SCANNING PROBE ALLOYING NANOLITHOGRAPHY (SPAN)

A Dissertation

by

HYUNGOO LEE

Submitted to the Office of Graduate Studies of
Texas A&M University
in partial fulfillment of the requirements for the degree of

DOCTOR OF PHILOSOPHY

May 2009

Major Subject: Mechanical Engineering

SCANNING PROBE ALLOYING NANOLITHOGRAPHY (SPAN)

A Dissertation

by

HYUNGOO LEE

Submitted to the Office of Graduate Studies of
Texas A&M University
in partial fulfillment of the requirements for the degree of

DOCTOR OF PHILOSOPHY

Approved by:

Chair of Committee,	Hong Liang
Committee Members,	Anastasia Muliana
	Miladin Radovic
	Philip Hemmer
Head of Department,	Dennis O'Neal

May 2009

Major Subject: Mechanical Engineering

ABSTRACT

Scanning Probe Alloying Nanolithography (SPAN). (May 2009)

Hyungoo Lee, B.S., University of Seoul

Chair of Advisory Committee: Dr. Hong Liang

In recent years, nanowires have become increasingly important due to their unique properties and applications. Thus, processes in the fabrication to nanostructures has come a focal point in research. In this research, a new method to fabricate nanowires has been developed. The new technique is called the Scanning Probe Alloying Nanolithography (SPAN). The SPAN was processed using an Atomic Force Microscope (AFM) in ambient environment. Firstly, an AFM probe was coated with gold (Au), and then slid on a silicon (Si) substrate. The contact-sliding motion generated a nanostructure on the substrate, instead of wear. Subsequently, careful examination was carried out at the scale relevant to an AFM probe, in terms of physical dimension and electrical conductivity. The measured conductivity value of the generated microstructures was found to be between the conductivity values of pure silicon and gold. Simple analysis indicated that the microstructures were formed due to frictional energy dispersed in the interface forming a bond to sustain mechanical wear. This research proves the feasibilities of tip-based nanomanufacturing. The SPAN process was developed to increase efficiency of the technique. This study also explored the possibility of the applications as a biosensor and a flexible device.

This dissertation contains nine sections. The first section introduces backgrounds necessary to understand the subject matter. It reviews current status of the nanofabrication technologies. The basic concepts of AFM are also provided. The second section discusses the motivation and goals in detail. The third section covers the new technology, scanning probe alloying nanolithography (SPAN) to fabricate nanostructures. The fourth talks about characterization of nanostructures. Subsequently, the characterized nanostructures and their mechanical, chemical, and electrical properties are discussed in the fifth section. In the sixth section, the new process to form a nanostructure is evaluated and its mechanism is discussed. The seventh section discusses the feasibility of the nanostructures to be used in biosensors and flexible devices. The conclusion of the research is summarized in the seventh section.

ACKNOWLEDGEMENTS

Specially, I would like to offer my sincere gratitude to my advisor, Dr. Hong Liang, for giving me opportunities to study and do research, and for guiding and advising me. I would also like to thank my committee members, Dr. Anastasia Muliana, Dr. Miladin Radovic, and Dr. Philip Hemmer, for their guidance and support throughout the course of this research. I thank Dr. Jun Zou, who supported me in research and participated in my defense. My group members gave me a lot of helpful advice and discussion while I was in Dr. Liang's group. I also want to extend my gratitude for financial support by the National Science Foundation (0506082 and 0515930). Finally, thanks to my family for their patience and love.

NOMENCLATURE

AFM	Atomic force microscope
CD	The critical dimension (the smallest pattern)
DRAM	Dynamic random access memory
MEMS	Micro-Electro-Mechanical System
MLS	Motorized Linear Stage
MPU	Microprocessor unit
NEMS	Nano-Electro-Mechanical System
NSOM	Near-Field Scanning Optical Microscope
PVDF	Polyvinylidene difluoride
SEM	Scanning electron microscope
SPAN	Scanning probe alloying nanolithography
STM	Scanning tunneling microscope
TEM	Transmission electron microscope

TABLE OF CONTENTS

Page

LIST OF FIGURES

Page

Page

LIST OF TABLES

Page

1. INTRODUCTION

This section provides background necessary to understand the motivation and objectives of the research. A review in lithography is provided. First of all, basic backgrounds and importance of lithography is discussed. The limitations of current lithography are explained and some alternative fabrication methods are discussed. Finally, the principles and fundamentals of Atomic force microscopy (AFM) which is a main instrument in this research are presented.

1.1. Lithography

1.1.1. Background

The word of lithography was from Greek. The 'litho' means stone, and 'graphy' writing; i.e., stone-writing. There are many lithography methods. The dominant patterning technique is the 'photolithography.' The 'photo' means light. This technique is the process to pattern the geometric shapes of mask onto silicon wafer. This technique has been used in semiconductor industry to make integrated circuits [1].

The entire process of the photolithography involves surface preparation (wafer cleaning), pre-baking, photoresist application (spin coating), soft baking, wafer loading, alignment, exposure, development, and hard baking. Figure 1.1 is a diagram to depict the process of the regular photolithography.

This dissertation follows the style of IEEE Transactions.

Ultraviolet (UV) light illuminates and passes through mask and lens, then exposes photoresist on a silicon wafer. The wafer is submersed into the developing solution [2]. The photolithography can be categorized into three parts with different space between the masks and substrates. The first is the mask contacted to photoresist samples. This is so called the contact printing. The advantage of the contact printing is that one can get higher resolution than other printing methods. The disadvantage of the contact printing is to damage the silicon wafer on the contact area [3-5]. Proximity printing method was invented for preventing the wafer damage due to the contact between the silicon wafer and the mask. This method is similar to the contact printing method. However, there is a small gap ($10 \sim 50\,\mu m$) between the mask and the wafer silicon. Although this gap of the proximity printing minimizes the damage on the wafer, the resolution is not high, about $2 \sim 4\,\mu m$ [6-8]. In order to increase the resolution and reduce the sample damage, the projection printing method was invented by Perkin-Elmer, 1973. This method removes the damage induced by direct contact completely and the resolution can be as small as $1\,\mu m$. The disadvantage is that only a small area on the silicon wafer can be scanned. The process should be repeated for other areas until the entire area of the wafer is scanned. This method is called step-and-repeat system [9-13].

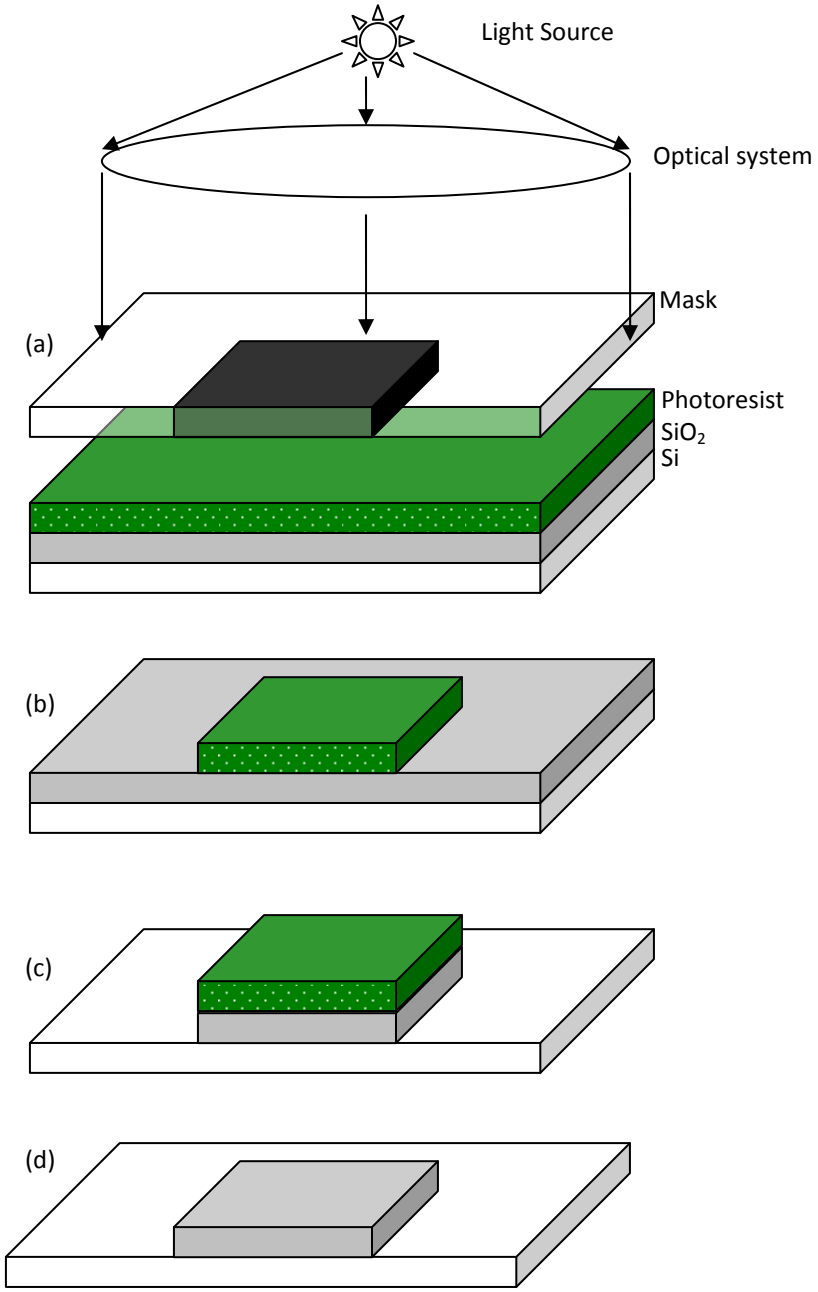

Figure 1.1 Steps of optical lithography process.

1.1.2. Importance of Lithography

Lithography plays a key role in semiconductor technology [14]. Lithography can enable or limit the growth speed of semiconductor industries. Table 1.1 lists the critical dimensions of a chip with years [14]. The lithography advanced IC manufacturing. As shown in Table 1.1, as the line dimensions are reduced, the number of transistors in a microprocessor unit increases, also the cost of one transistor decreases.

Table 1.1 The performance improvements of chips [14].

Year		1999	2002	2005	2008	2011
Dense Line CD (nm)		180	130	100	70	50
Isolated Line CD (nm)		140	100	70	50	35
MPU	Frequency(MHz)	600	800	1100	1400	1800
	Transistor/cm^2	6.2M	18M	39M	84M	180M
	Cost/Transistor (microcents)	1735	580	255	110	49
DRAM	Bits	1G	4G	16G	64G	256G
	Bits/cm^2	270M	770M	2.2B	6.1B	17B
	Cost/Bit (microcents)	40	15	5.3	1.9	0.66

CD: the critical dimension (the smallest pattern)
MPU: microprocessor unit
DRAM: dynamic random access memory

1.1.3. Limitations of Lithography

1.1.3.1. Resolution

There is a critical problem with the photolithography; resolution. The resolution is limited by optical diffraction. As shown in the following equations (Equ.1), the minimum printed-feature size (R, resolution) depends on the wavelength (λ) and the aperture (*NA*) of exposure system [15-23].

$$R = k_1 \frac{\lambda}{NA},\ DOF = k_2 \frac{\lambda}{NA^2},\ NA = n\sin(\theta) \quad \text{----------} \quad \text{(Equ.1)}$$

where R is resolution, k_1 and k_2 are constants (normally 0.5-0.8 for k_1 and 0.1-0.5 for k_2) depending on the resist technology, λ is the wavelength of the transmitted light, *NA* is the numerical aperture (the sine of the convergence angle of the lens,) and DOF is the depth of focus.

To obtain smaller feature size, the wavelength λ should be decreased and the numerical aperture should increase. Thus, the wavelength has been reduced from 435nm (g-line [24-29]) to 405nm (h-line [30]) to 365nm (i-line [31]) to 248nm (DUV, deep ultraviolet [32]). The critical resolutions (CD) are $0.5\mu m$, $0.4\mu m$, $0.35\mu m$, and $0.25\mu m$, respectively. However, the depth of focus also will be decreased as increasing the resolution. The decreased depth of focus will reduce the process latitude (capability) of the optical system [23].

1.1.3.2. Alignment

One of other problems involved with lithography is the alignment [33-41]. For fabricating an integrated circuit, a number of layers should be printed. Typically 15 to 25

layers are demanded. Those layers should be precisely aligned for fabricating a non-defected chip. It is difficult to make a precise alignment for each layer. This leads to a trade-off between alignment accuracy and alignment time. In addition, there is a trade-off between resolution and alignment. As the pattern size decreases, it gets more difficult to make a good alignment between layers. Thus, alternative nanolithography methods were invented to solve the problems of above-mentioned lithography. One of the promising technologies is the AFM lithography [42-67].

1.1.4. Alternatives

There are several alternative lithographic technologies overcoming the resolution limits of optical lithography [68-74]. Extreme ultraviolet (EUV [23]) or X-ray lithography (XRL [75-77]) use smaller wavelength which is 13.4nm or 7Å, respectively. The small wavelength can be easily absorbed by air. The process of this lithography should be done in vacuum. The lenses and masks should be devised specially for this wavelength due to its absorption. Those reasons increase the process cost. Electron Beam Lithography (EBL [78-80]) can scan a finely focused beam and directly write features on a sample. The features can be as small as 10nm by using EBL. However, the throughput of EBL is very low. This means that the process is slower and more expensive than others. EBL is normally used for making masks of other lithography.

1.1.5. Scanning probe alloying nanolithography (SPAN)

There are many AFM based lithography methods [81-88]. In general, the methods can be categorized into two groups; force-based lithography or bias-based one. In bias-

based lithography, the AFM tips are biased to create an electrical field between the tips and the substrate surfaces. For force-based lithography, larger forces are loaded on the substrate surface, which fabricate a structure on the surface. In the following, SPAN of bias-based lithography will be discussed. The SPAN is a new technology of among force-based lithography methods. The SPAN has significant advantages over the regular lithography. With AFM lithography, the patterns can be fabricated on various materials such as metals, semiconductors, and polymers. SPAN can be processed in air, liquid, or vacuum environments. The fabricated patterns by SPAN can be characterized by using AFM immediately.

1.2. Introduction of AFM

Atomic Force Microscope (AFM) is being used in wide range technologies, such as biological, chemical, and electrical industries. In addition, AFM is being applied to fabricate nano-materials or devices. AFM is a type of Scanning Probe Microscope (SPM). The SPM covers technologies to image and measure surfaces on a micro- or nano-scale. There are three most common types of SPM; Scanning Tunneling Microscope (STM), Atomic Force Microscope (AFM), and Near-Field Scanning Optical Microscope (NSOM). These three types share the concept that an extremely sharp tip (3-50 nm radius of curvature) scans a substrate surface. In scuh the system detects the surface properties, such as topography, phase, or conductivity.

While AFM measures the interaction force between the tip and surface, the STM measures a weak electrical current flowing between tip and sample, and NSOM detects light energy very close to the sample.

1.2.1. Comparison of AFMs

The STM is the origin of an AFM. Sometimes, STM resolution is better than AFM because tunneling current of STM dependent exponentially on distance between the tip and the substrate surface. But, the samples of STM should be conductive while AFM can be used for both of conductive and non-conductive samples. That is, the AFM is more versatile than STM. Scanning Electron Microscope (SEM) has good depth of field, and scans very fast. However, it needs samples coated with conductive materials such as Ag, Au, and Au-Pd. While SEM can get a 2D image, AFM shows 3D images. AFM doesn't need vacuum system which SEM needs. The images of AFM have good contrast even the samples are not coated with conductive materials. Compared with Transmission Electron Microscopes (TEM), the samples of AFM don't need special and expensive preparation. Also, AFM gives more complete information than the two dimensional profiles available from cross-sectioned samples.

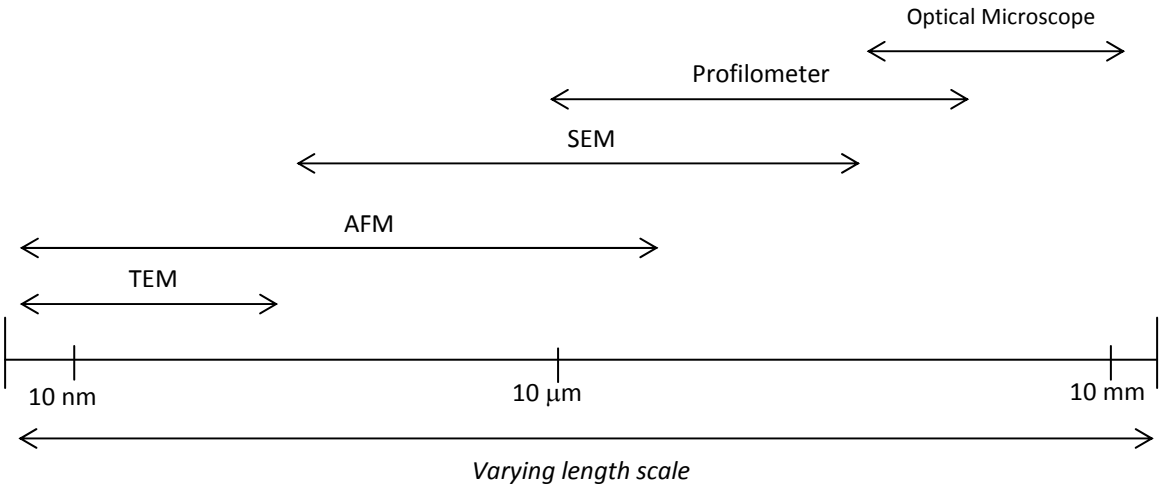

Figure 1.2. Comparison of AFM with other measurements (Courtesy of PNI).

As shown in Figure 1.2, the scanning range of AFM is broader than others. TEM can be used to get sample information at a few nanometer or micrometer ranges which AFM can cover. Profilometer cannot give 3D information, but only cross sectional information of samples.

1.2.2. History

Binnig, Rohrer, Gerber, and Weibel introduced STM in 1981 [42, 89, 90]. The STM opened the imaging technology of atom scale. Figure 1.3 shows the conception of the STM that a sample surface could be interpreted from its deformations. After one year (1982) of its introduction, the adatom layer of Si (111) was imaged with an STM by Binnig et al.[42, 89, 90] (See Figure 1.4).

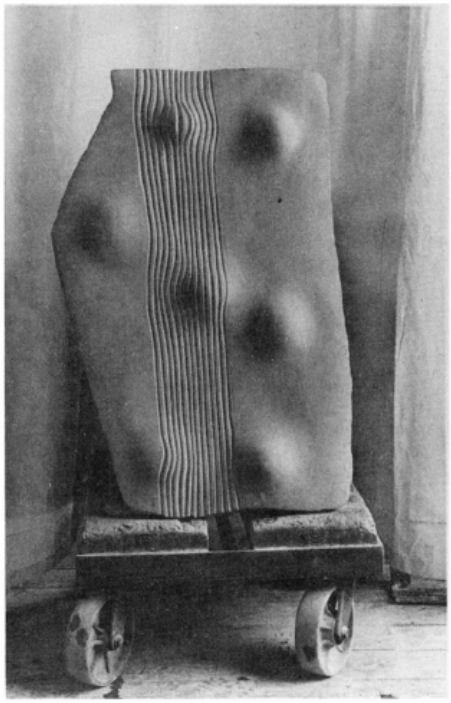

Figure 1.3. The conception of STM. (sculptor, Ruedi Rempfler)

G. Binnig and H. Rohrer were rewarded with the Nobel Prize in Physics in 1986. The STM is a milestone of the nanotechnologies, but it has a serious limitation. That is, STM use the tunneling current flowing between a tip and a sample so that the sample should be an electrical conductive material.

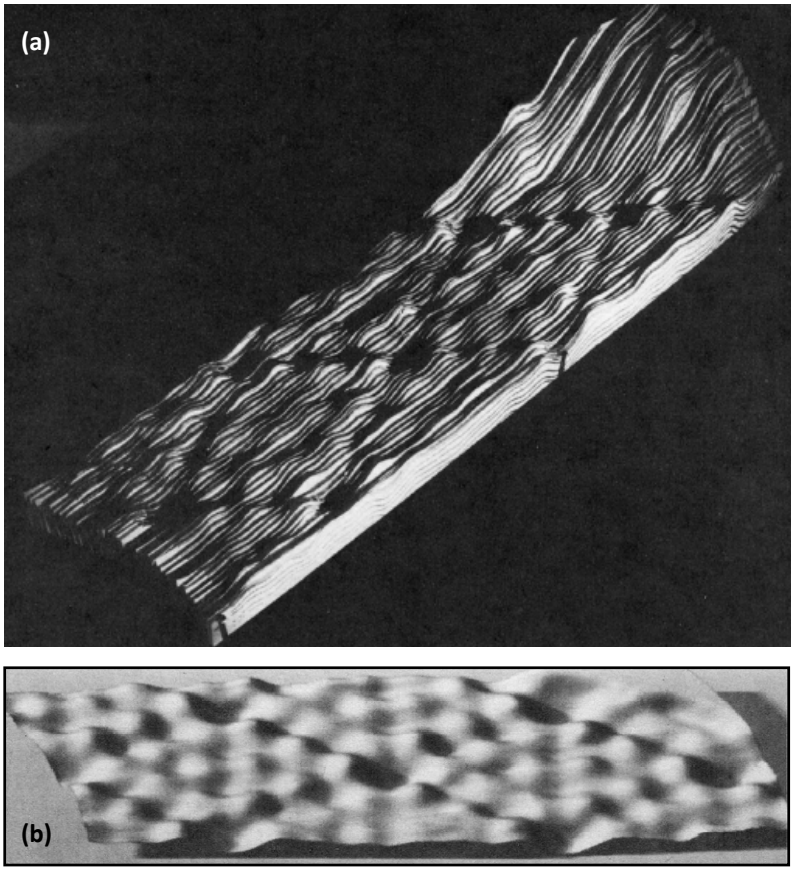

Figure 1.4. The first scan images of STM by Binnig et al. in 1983; (a) the original tracing image (b) the processed image of 7×7 reconstruction of Si (111).

From the experiments of STM, Binnig found that there were significant forces between the STM tip and the sample when the distance of the tip and sample was enough

close to flow the tunneling current [89]. By using the forces, Binnig et al. invented AFM [42, 89, 90]. In the result, the first commercial AFM was fabricated by the company, Park Scientific. Consequently, thousands of AFM's are in use in university, public and industrial research laboratories all over the world.

1.2.3. Laser and Detector

There are forces between an AFM probe and a sample when the probe contact to the sample surface; attraction and repulsion forces. AFM operate with the forces [89]. As the tip drags over the sample, the forces between the tip and the sample have the cantilever of the tip deflected or twisted. A laser beam of AFM is reflected and detected by a photo-detector of AFM. The reflection direction of the beam is changed due to the cantilever deflection. The detector measures the position of the reflected beam on the detector horizontally and vertically. The schematic of the laser beam, the photo-detector, and the cantilever is shown in Figure 1.5. The detected signals are processed by the AFM computer (controller). The vertical change of the reflected beam position on the detector indicates the sample height. The horizontal change is for the frictional force between the probe and the sample. The differential amplifier in Figure 1.5 enlarges the amplitude of the output signals of the photodetector.

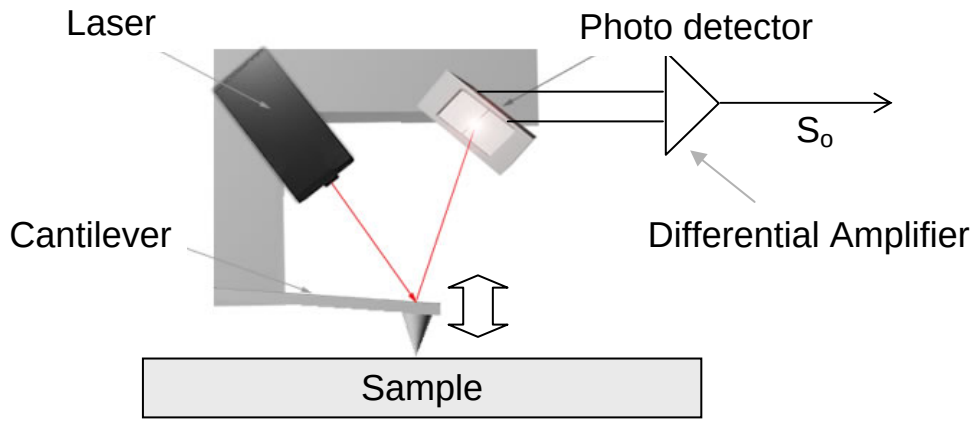

Figure 1.5. Schematic of the structure of AFM with Laser, photo detector, and cantilever. (Courtesy of PNI)

1.2.4. AFM system

Appling electrical energy to a piezoelectric ceramic material creates the mechanical movement, which called an electromechanical transducer [91-94]. The transducer is mostly used in AFM system. A typical piezoelectric disc will vertically expand by about 1nm per applied volt. It's possible to expand a piezoelectric disc up to 0.1mm by applying 100V. The larger motions can be made by adding more layers of piezoelectric materials on the piezoelectric disc. That is, the piezoelectric discs including 1000 disc layers expand 1000nm when exposed to only 1V energy potential. Figure 1.6 shows an example that the expansion of a piezoelectric disc is achieved when they are exposed to an electric potential. The motion size, speed, direction depends on the type of piezoelectric material, shape, the number of the added discs, and the applied electric energy strength.

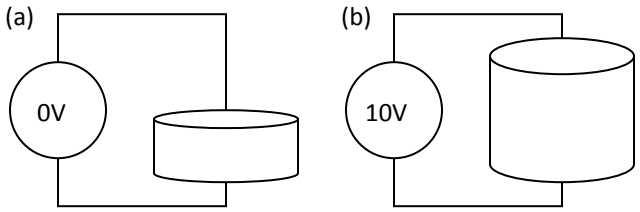

Figure 1.6. Piezoelectric Ceramic disc. (a) Applying no voltage will not make any change on the disc, but (b) applying some voltage will vertically expend the disc at the rate with 1nm per 1 volt.

Those piezoelectric ceramic discs are used for x, y, and z transducer controllers [95]. As shown in Figure 1.7, there are X, Y and Z motors. By using the motors, the AFM probe is roughly placed the location close to the sample where will be imaged. The z piezoelectric ceramic transducer places the probe to the surface very precisely. During scanning, x, y and z piezoelectric ceramic discs are used because their motions in nanometer amount can be controlled.

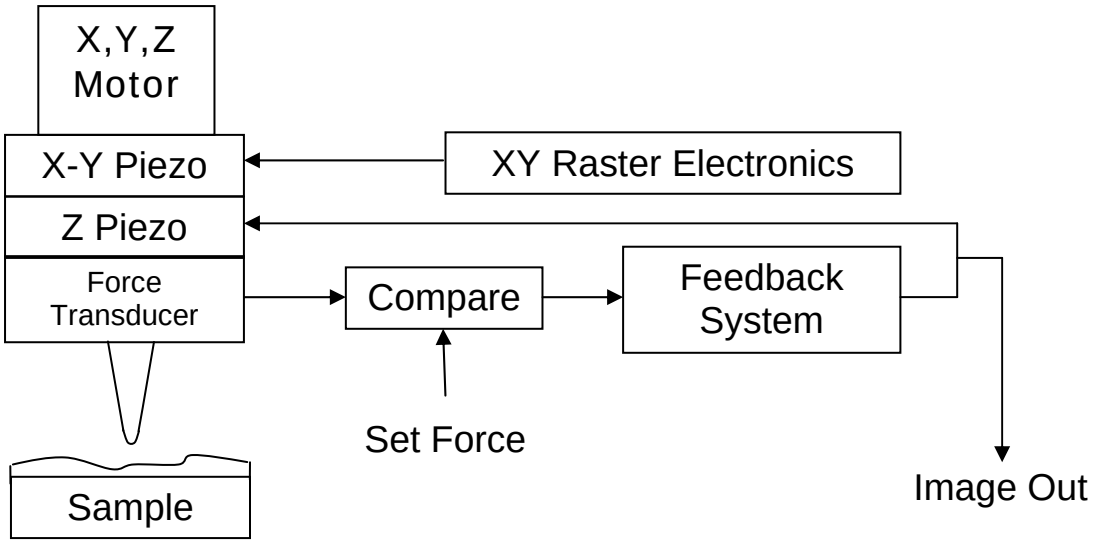

Figure 1.7. The system diagram of an Atomic Force Microscope. (Courtesy of PNI)

The piezoelectric discs for x and y are expanded while the probe is moved on the sample surface. The feedback system takes the signal from the force sensor. Then, the signal generator of the feedback system generates output voltages. The voltages control the Z-piezoelectric ceramic to change the Z-height of the probe. This voltage is necessary to keep the cantilever deflection constant while scanning.

1.2.5. Probe Approach

There are many mechanisms for the probe approaching to a sample surface [89, 96-99]. To bring the probe from 1mm above the surface to within 0.1nm in 60 seconds is same to fly to the moon in 60 seconds and stop within 38 meters of the surface. This would require traveling at 23 million kilometers per hour. A typically used approach method is 'Wood Pecker' tip approach. The Z motor goes down $1\mu m$, and then the z piezoelectric ceramic disc have the probe cantilever down to $5\mu m$. While the z ceramic disc make the cantilever go down, the force sensor system monitors if the probe is close to the sample surface. If the probe is still far from the surface, the Z motor goes down more $1\mu m$. Then, the z ceramic disc scans again. The system repeat these step until the probe gets close to the surface. This mechanism is called as 'Wood Pecker' tip approach because it's very similar to the behavior of the bird, wood pecker.

1.2.6. Cantilever and Probe

There are many kinds of cantilevers and probes [56, 100] as shown in Figure 1.8. Those are categorized by their shapes, materials, and usages. Typically, cantilevers are either triangular or rectangular shaped. The cantilever shape and materials affect on its

spring constant value. That is, the triangle shaped cantilever has higher spring constant value than that of rectangle shaped one. Also, it can stand higher torsion or higher vertical-bending force. The rectangle cantilever can be used to scan softer samples. The probe materials can be diamond, silicon or silicon nitride. Probes shapes can be pyramidal or conical and may be sharpened.

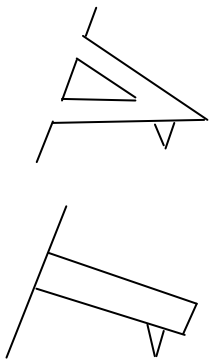

Figure 1.8. Two kinds of cantilevers; triangle and rectangle shapes. (Courtesy of PNI)

1.2.7. Mode

The AFM become much more versatile and capable than before various modes were developed. Two modes can be broadly categorized; DC and AC modes. Those two modes are separated with oscillation of AFM cantilevers. That is, AC modes oscillate the AFM cantilevers, but DC modes don't. The contact mode of AFM doesn't use the oscillation. The contact mode is a common mode used in AFM to scan a sample surface with the AFM probes. Although the term 'contact' is used for the mode, actually the tip doesn't touch the sample because of the repulsive force between the probe and the sample. (See Figure 1.9) The cantilever is pushed against the repulsive force from the surface to the

probe. The deflection of the probe cantilever is detected by the force sensor elements. If the contact mode probe scans on a sample surface, the electrostatic charge will be trapped.

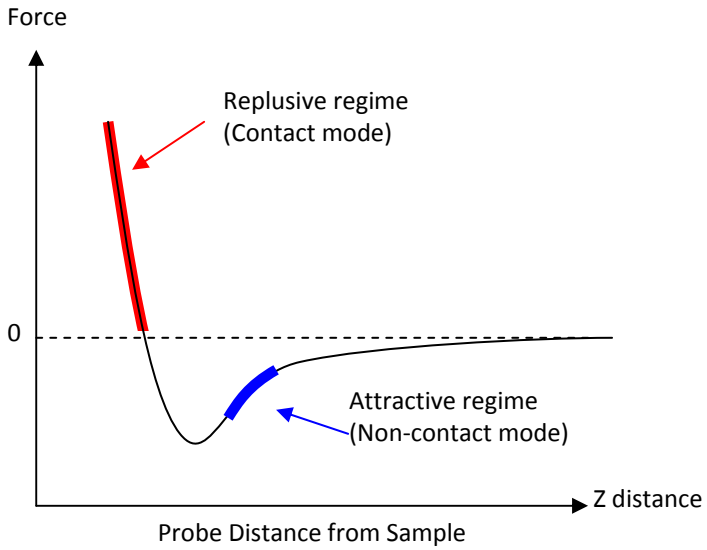

Figure 1.9. Potential energy (force) diagram of the interaction between a probe from a sample. The red line is for repulsive force, and the blue one is attractive regime. (http://www.mobot.org/jwcross/spm/)

This charge substantially causes additional attractive forces between the probe and the surface. Those additional attractive forces effect on the cantilever or sample. The cantilever will be twisted. Sometimes, this twisted cantilever is monitored, and used for imaging the frictional image of the sample surface. However, the forces which are enough to twist the cantilever will damage on soft samples such as biological or chemical samples. Also, the forces can dull the cantilever probe or distort the scanned images. Thus, there is a solution of those forces causing damages on samples. The solution is the

non-contact mode. While the contact mode AFM is in the repulsive regime of the potential energy diagram of the probe-sample interaction, the non-contact mode is in the attractive regime as shown in Figure 1.8. In non-contact mode, the probe doesn't touch the sample at all. The probe is always scanned 50~150Å̀ above the surface. Van der Waals forces between the probe and the sample surface are detected to image the surface [101]. However, the Van der Waals forces are much weaker than the forces of the contact mode. The probe should have an oscillation. This method is called AC detection. The oscillation is used to detect the forces between the probe and the sample surface. The cantilever will be also affected by the force gradients from the sample. Finally, the AFM measures the changes of amplitude, phase, or frequency of the cantilever oscillation. Another solution for the friction forces between the probe and the sample is the tapping (intermittent contact) mode of AFM. This mode overcomes the problems related to friction, adhesion, and electrostatic forces. It also doesn't damage the soft samples while scanning [102]. The tip in the tapping mode provides higher resolution than other modes, but in practical it's more difficult to get images by using the tapping mode tip [103]. While scanning the surface, the tip drags over the sample and oscillates simultaneously [53]. The z piezoelectric disc drives the cantilever oscillation with high amplitude of more than 20nm. The frequency of the tapping tip oscillation is about 100 kHz and 400 kHz with vibration amplitude of a few nanometers. While non-contact mode imaging generally provides low resolution, tapping mode achieve high resolution without destructive frictional force. That is, the tapping mode tip can be used for the very soft and fragile samples successfully.

1.2.8. Resolution

AFM has two resolutions; the plane (x, y) resolution and vertical (z) resolution [104]. The x and y piezoelectric discs are used to scan the probe on a sample. The plane resolution means how precise the sample surface can be imaged. The resolution mostly depends on the sharpness of the probes [105-108]. Thus, many methods to fabricate the probes are investigated [52, 56, 100, 109-114]. The recent AFM technology established a resolution of 10pm.

The vertical resolution is for the perpendicular direction to the sample surface. The height changes of the probe are monitored. Those changes give information to the imaging processor to get an image for the surface height. However, some noises decrease the vertical resolution. The noises are from vibrations of the cantilever. The vibrations should be minimized to obtain the maximum vertical resolution. The source of the vibrations typically is from acoustic noise, floor vibrations, or thermal vibrations.

1.2.9. Measuring Properties

AFM is very powerful to measure most of all properties of a sample, such as mechanical, thermal, electrical, and magnetic properties. For the mechanical properties of a sample, AFM can measure the force-distant curve, friction (lateral) force between the tip and the sample, and phase changes. Phase imaging is an extension of tapping mode of AFM. The phase image provides nanometer-scale information of a sample surface. The oscillation the tapping mode tip changes when the tip meets other materials as the tip scans the sample surface. The changes of the oscillation consist of the phase as well as the amplitude of the oscillation. The different materials on the sample cause phase lags of the cantilever oscillation. The phase lag is sensitive to adhesion, viscoelasticity, or friction. The phase images can be used to identify sample contaminants and different components. It also can differentiate the surface area having high or low adhesion forces or hardness. Another mechanical property of a sample measured by AFM is force-distant curve.

1.3. Nanowires

In recent years, nanowires have attracted tremendous interests due to their unique properties. The diameter of a nanowire is about 50 nanometers or less. It can be categorized into two types: sub-microstructures (1μm–100nm) and nano-structures (1–100nm). At the nano-meter length scale, there is the confinement of charged carriers in their own structures such as nano-films, nano-wires, or nano-dots, as shown in Figure 1.10.

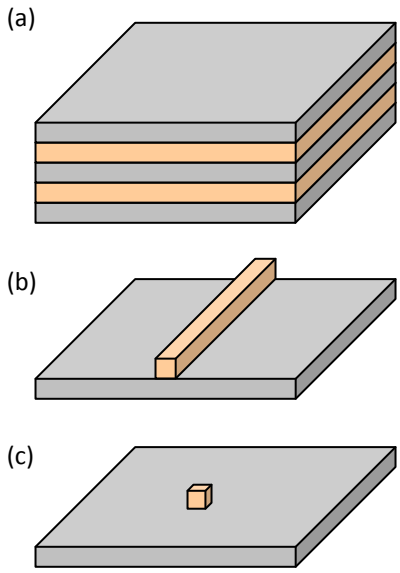

Figure 1.10. Three nanostructures. (a) quantum well, (b) quantum wire, and (c) quantum dot.

The confinement drives important quantum mechanical phenomena of nanowires. The conductance is quantized, the band-gap is modified, and coulomb is blockaded [115]. Those phenomena will be utilized for its applications such as a single-electron

transistor which operates at a low power. The transistor works as the base for nanowire devices. There are many different types of nanowires. They can be broadly separated into three types; metals, semiconductor, and insulators. Metallic nanowires include Ni, Pt, or Au. Semiconducting wires are Si, InP, or GaN. The nanowires composed of SiO_2 or TiO_2 are insulating. These nanowires are inorganic. Organic materials, such as DNA, are building the nanowires by repeating molecular units.

1.3.1. Properties

Due to their nanometer-length-scale size, nanowires have peculiar electrical, mechanical, and optical properties. Electrical properties are a key for being used in semiconductor. The properties can be applied to semiconductors or sensors. Current flowing throughout the nanowires is changing with small change of applied electrical potential due to the edge effects [116]. There are many electrons on a nanowire surface that are not bonded. Those free electrons on the surface play a source of conductivity of nanowires. This effect is called an edge effect [117]. As decreasing the size of nanowires, the edge effect becomes more significant to the nanowires' properties.

1.3.2. Applications

Nanostructures can be used in electronic or optical devices and sensors. In the nano-sized electronic device areas, most researchers are interested in nanometer-sized transistors to extend Moore's law beyond 100 nm resolution [118]. It has been known that nanowire transistors are at least four times faster than conventional semi-

conductive devices [119]. The devices are inexpensive, but save space so that they can be used in displays or cell phones. In optical applications, there are optical sources and detectors made with nanowires. The nanowires in the applications improve their own characteristics which cannot be achieved by large scale devices. The nano devices have lower threshold current so that they can save energy and perform faster and more dynamically than bulk-wire optical devices. In addition, they can improve the emission line-width in quantum dot lasers. In the sensor application area, the nanowires behave sensitively and selectively more than conventional optical lithography does. Cui et al.[120] devised a sensitive electrical sensor. The sensors perform in real-time as a chemical or a biological sensor. The researchers fabricated doped-silicon nanowires for the sensors. As changing the pH values in a solution, the conductance of the nanowire sensors will be changed nonlinearly. Thus the sensors detect pH values with high sensitivity [121].

1.3.3. Fabrication of Nanowires

Researchers have attempted to fabricate the nanowires in several ways [122]. Nanofabrication focuses on technologies to fabricate sub-micron or nano-scale structures. To achieve nanofabrication, the optical lithograph has been developed continuously. However, there is a limitation of the lithography method; trading-off between resolution and accuracy. The resolution is for minimum resolvable feature, and the accuracy is from Depth of focus (DOF) [123]. Rayleigh's equations have been used to optimize the typical optical lithography to obtain a high resolution with accuracy [123]. According to Equ.1, the resolution R trades off with the depth of

focus (DOF). However, the depth of focus becomes small so that the exposure process becomes sensitive to the distance between the substrates and lenses, and the position of the resist layer [124]**.** To improve the resolution, various methods have been invented. Methods can be broadly divide into top-down and bottom-up categories. The top-down approach starts with bulk materials and removes the materials in a specific area to fabricate nanostructures. The top-down approach is an extension of the typical optical lithography or micromachining. This approach is close to the mechanical or optical engineering. On the other hand, the bottom-up method builds or grows a structure on a substrate. Over the past few years, the bottom-up approach is mainly focused on the synthesis of low-dimensional semiconductor materials. Hence, the bottom-up approach is closer to chemical engineering or material science than the top-down approach. For the top-down techniques, there is Electron-beam lithography (EBL) to pattern nanowires [125, 126]. EBL has a disadvantage of which throughput is very low. To overcome the low throughput of EBL, the nanoimprint technology is invented [127], but it makes the fabrication complicated. There are three main methods in bottom-up fabrication; epitaxy engineering [128-133], self-assembly manufacturing [134], and template-assisted synthesis [135-137]. However, for those methods, it's difficult and complicate to locate a nanowire on a specific area.

1.4. Needs

As predicted by the Moore's Law, the device dimensions of production transistors have been decreased exponentially since 1965 [138]. In 1998 the device

dimensions faced a wall of 250nm that it was difficult for the typical conventional lithography techniques to break through [138]. In 1997, the Semiconductor Industry Association predicted that critical dimensions would decrease to 150nm by 2001, to 100nm by 2006, and to 50nm by 2012 [139]. The current size is about 50nm To date, the conventional optical lithography used to fabricate the integrated circuits is facing the limitations of resolution-accuracy trading-off, as discussed in the introduction section. An alternative lithography may be devised within the next five years to achieve and extend Moore's Law. In such the scanning probe alloying lithography will be investigated to pattern 100nm feature sizes and below.

Both of bottom-up and top-down methods to fabricate the nanowires have limitations. The top-down techniques to fabricate the nanowires have been the fundamental method of semiconductor devices [118]. Nevertheless, as explained in the section, 1.4, the methods cannot obtain high accuracy and small enough features to be used in nano-devices. Among the top-down methods, EBL is well established for high resolution with high accuracy. This process is also very slow and expensive. On the other hand, the bottom-up methods can manufacture nano-sized features. The down side is that they are expensive and systems are complex to operate. It's mostly impossible to locate the nanowires in a specific region during the process [140].

2. OBJECTIVES

The long term objective of this research is to develop new nanomanufacturing processes in order to fabricate nanostructures with unique properties. There are four objectives in this thesis research:

A. Develop a nanomanufacturing process, Scanning probe alloying nanolithography (SPAN).

B. Process optimization.

C. Develop a methodology to characterize nanostructures.

D. Obtain basic understanding of the interfacial phenomena.

A. Develop a nanomanufacturing process, SPAN.

We will develop the SPAN technology using an AFM for its high resolution and ease in control. In the present research, a new method to fabricate nanowires will be developed. The method is called the scanning probe alloying nanolithography (SPAN). The SPAN is similar to write with a pencil on a piece of paper. The alloying is simply referring to the nature of mixer of the Au-Si that dominates the property of nanowires. This process is different from any other AFM based methods. Comparing with the dip-pen lithography, this process is simple and doesn't use metallic ink. This process can use electrical potentials however being different from AFM Oxidation lithography. The latter applies only electrical potentials without a mechanical force in order to form a

nanostructure. The major difficulties of SPAN are to increase productivity and efficiency of the process. We will overcome them by controlling the temperature of substrate surfaces. Another difficulty of the SPAN is to obtain uniform nanostructures. For this issue, the contact-sliding direction is discussed. It is expected that this process would enable nanostructures to be located in a desired area and be capable to fabricate nanostructures at 100nm sizes or smaller. The efficiency and precision of the SPAN process was expected to be higher and better than existing techniques. In addition, the materials used in SPAN would be wider than other techniques. Furthermore, the SPAN is able to overcome the limitations of the conventional nanofabrication methods as mentioned above. With the capability of SPAN, nanostructures were fabricated.

B. Process Optimization.

The process of SPAN will be optimized to increase productivity, efficiency, and uniformity of the nanostructures by evaluating the process parameters. There are four main parameters; probe sliding speed, down-force of the probe, sample surface temperature, and the number of strokes. It's critical to understand the complete process of SPAN for developing and optimizing the process to fabricate a nanostructure efficiently.

C. Characterization.

In this objective, nanostructures generated by SPAN will be characterized. To understand the surface properties, behaviors, and structures of the nanostructures, the nanowires will be characterized for physical, chemical, electrical, and mechanical

properties. We will use different high resolution techniques, such as AFM, TEM, SEM, EDS, and nanoindentation, among others.

D. Interfacial phenomena.

Under this objective, the interfacial phenomena in SPAN occurred during the process will be studied. Understanding the phenomena is needed to develop and optimize the SPAN process. Study the mechanism of SPAN; how the nanostructures are formed by contact-sliding, materials transfer, and the interface between nanostructures and the substrate will be investigated.

3. PROCESS DEVELOPMENT OF SCANNING PROBE ALLOYING NANOLITHOGRAPHY

In this research, Scanning Probe Alloying Nanolithography (SPAN) is developed. The experimental setup is sketched in Figure 3.1. The AFM probe approaches on a substrate and writes a nanostructure. It's similar to pencil writing on a paper. The 'writing' process experiences friction between the sharp probe and the substrate, resulting in occurring alloy of the materials at nano-scale. The process involves thermal, physical, and chemical principles, such as friction and wear.

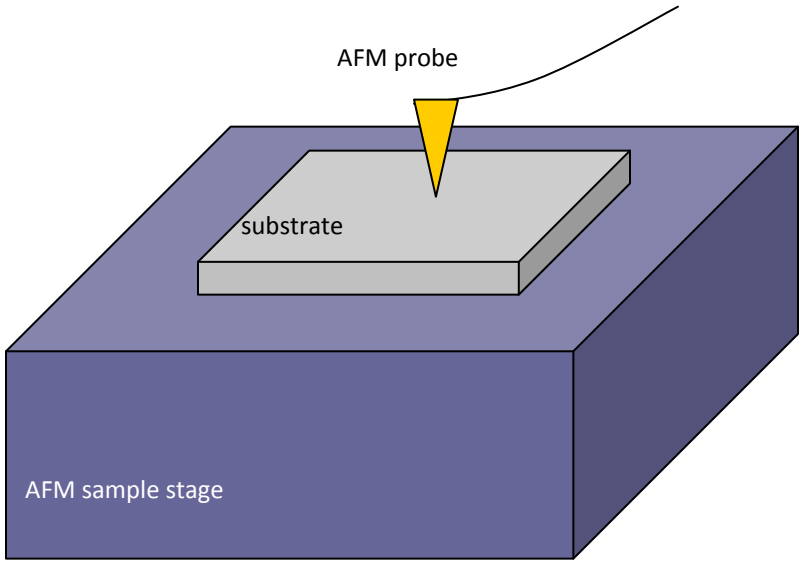

Figure 3.1 Simple diagram of experimental setup with AFM probe and a substrate. The AMF probe is slid on the substrate to 'write' a nanostructure.

3.1. Contact-sliding Experiments

Contact-sliding experiments were conducted by using an AFM (Nano-R^{-}, Pacific Nanotechnology Inc.) in a contact mode. With the down force of 503nN of Au-coated AFM probe, the Au tip slides against Si at the given speed (480μm/s). The applied load and contact-sliding speed were kept constant during tests. The gold was coated using a thermal evaporator (Edwards, Model: Auto 3063). Chromium (Cr) was deposited on a Si_3N_4 AFM tip to serve as an adhesion layer. Gold with 99.999% purity was deposited subsequently. The thickness of Cr and Au coatings were 15nm and 250nm, respectively. The surface characterization after contact-sliding experiments was conducted by using the same AFM with a standard Si_3N_4 tip. Close-contact-mode, also called as tapping-mode, was applied for this purpose with the scan rate at 1Hz for a 5μm in length.

The gold-coated probe was slid against the Si substrate in the contact mode. Figure 3.2 shows the schematic diagram of the experimental setup. The location, down-force, and sliding length of the probe were precisely controlled through the control panel of the AFM. Nanopatterns could be formed on the substrates by repetitive sliding of the probe. The shapes and dimensions of the patterns could be controlled by adjusting the down-force, sliding speed, temperature, and the number of strokes. Effects of electrical potential on the nanostructure were also investigated by applying a potential directly to the probe and substrate.

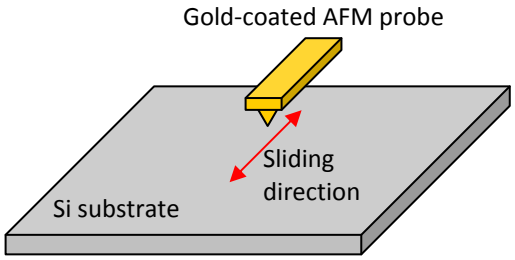

Figure 3.2. . The gold-coated AFM probe was slid on Si substrate along the red-colored direction.

3.2. Materials

For this study, the AFM is used as the major research instrument. Gold (Au) is coated on an AFM probe which works as a pencil. The substrate for this research will be Silicon (Si).

3.2.1. AFM

There are several advantages using an AFM. It is operated in normal ambient environment without a vacuum system which is needed in STM-based techniques. It has good reproducibility. The SPAN technique is expected to work with a wide range of materials. The operation and concept of an AFM is not complicated, but the control is very precise and simple. Figure 3.3 shows the AFM probe stage and the optical microscope. Using the optical microscope makes its operation easier and precise. Photodetector is sensitive enough to read nano-scale size features.

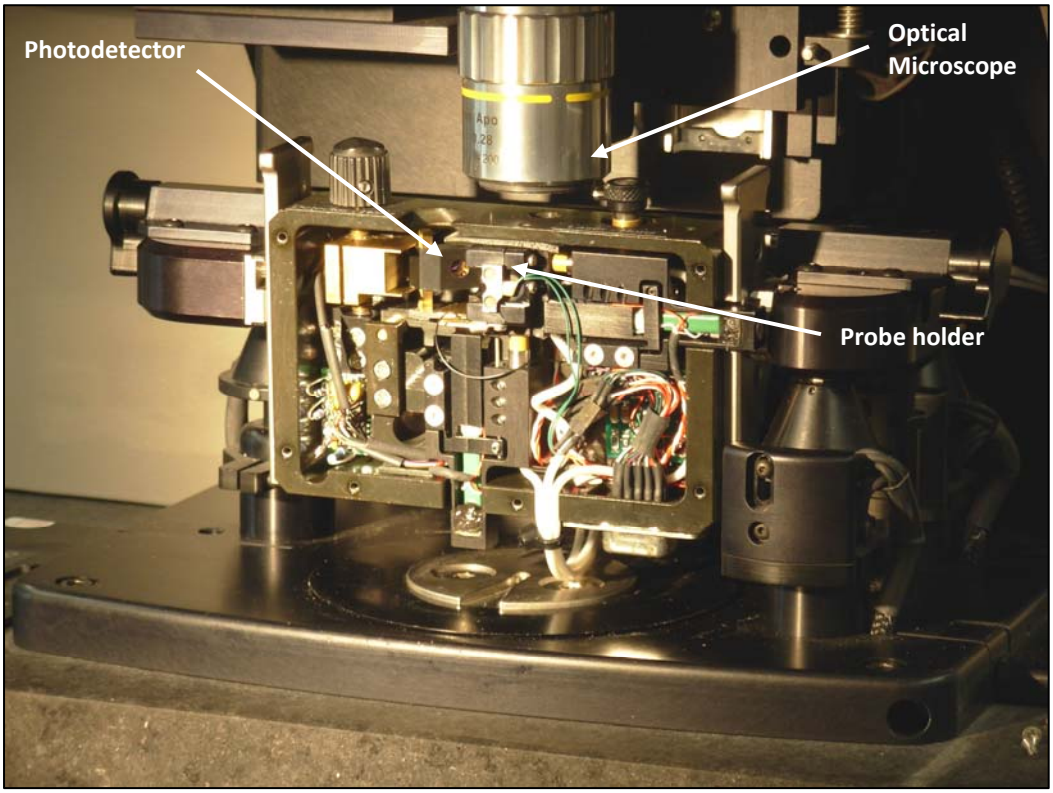

Figure 3.3 AFM probe stage and its circuits. AFM laser beam and the photo detector are embedded. It includes an optical microscope to operate easier.

3.2.2. Au & Si

For further applications of the nanowire into semiconductor devices, silicon (Si, 100) has been chosen as the substrate for this research. To fabricate a conductive nanowire, a highly-conductive material such as silver or gold should be chosen. Silver (Ag) has the lowest electrical resistivity (15.87nΩm) which is lower than gold (Au, 22.14nΩ·m). The melting point (962°C) of Ag is lower than that of gold (1064°C), shown in Figure 3.4. Despite of the advantages of Ag, gold has been chosen for this study.

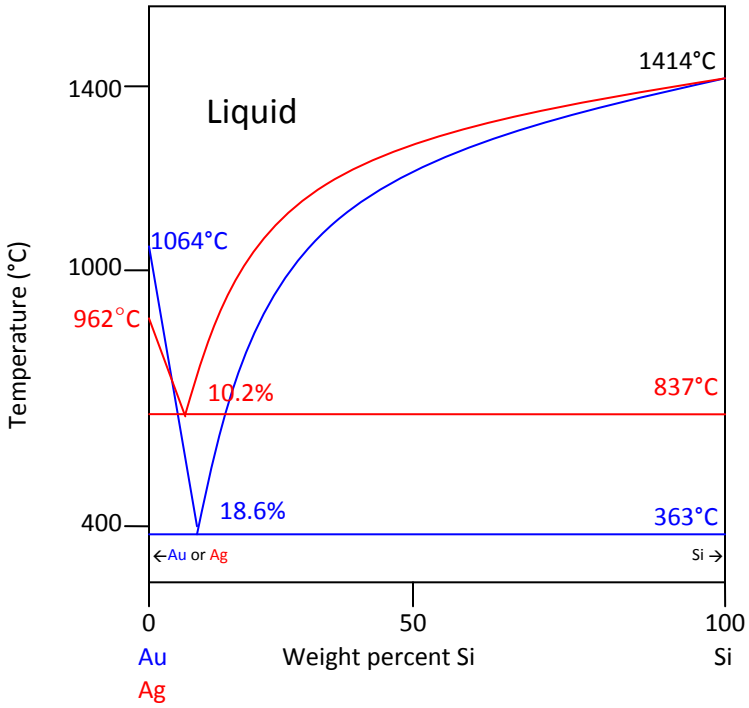

Figure 3.4 Phase diagram of Au and Si. The x-axis is for the weight percent of Si. The y-axis is the temperature. The blue-colored is for Au with Si, and the red is for Ag with Si.

The conductive nanowires will be fabricated with Si which drives the nanowires to an alloyed material. In the alloy materials, the eutectic points of them are more important than the melting points of each material involved in the process. The eutectic point of gold with silicon is lower than Ag with Si. The temperature of eutectic point of Au with Si is 363°C which is almost three times less than Ag with Si (867°C).

The gold material was chosen due to its stable properties, high conductivity ($45.2\times10^{6}S\cdot m^{-1}$), low resistivity ($2.44\times10^{-8}\Omega\cdot m$), and low eutectic temperature (360°C) with silicon. Au has an elastic modulus of 78GPa, hardness of 20Hv, and its crystal structure is cubic face centered (FCC). For further applications of the nanostructures

formed by SPAN as a biosensor, gold is suitable due to its strong adhesion with a thiol group [141, 142]. Single crystal silicon (Si, 100) was used as a substrate. Silicon is one of the most common materials in the semiconductor industry. This material has also been used in MEMS and other electronic devices [143-146]. The melting point of silicon is 1420°C. Its crystal structure is a diamond cubic and the Young's modulus is 150GPa. For each experiment, the Si substrates were cleaned successively with ethanol, isopropyl alcohol, acetone, and DI water. A standard AFM probe (Si_3N_4) was prepared by depositing a gold layer using a sputtering machine. The thickness of the Au layer was approximately 300nm. In Figure 3.5, the cantilever and the tip of the Au-coated probe are shown. The curvature of the tip is about 10nm (±5nm). The length and thickness of the cantilever is 100 and 1μm respectively.

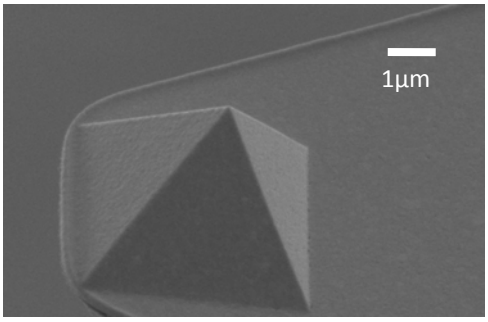

Figure 3.5. SEM image of a gold-coated AFM probe. Gold was deposited on the probe by a sputtering machine with 300nm thickness.

3.2.3. Parameters

There are four major parameters affecting the nanostructures formed by the SPAN process;

A. The number of strokes (N)

B. Sliding speed (v)

C. Surface temperature (T)

D. Down-force (F).

A. The number of strokes (N)

We have conducted a series of trails to fabricate nanostructures. It was found that the number of strokes affecting the final results. The contact-sliding of the probe induced the Au material transferred to the substrate to form a nanostructure on the Si surface. Figure 3.6 shows the structures after sliding. As increasing the number of the strokes, the height of the nanostructures increases.

As seen in the figure, the number of strokes (N) was the only variable while other conditions fixed. Here the sliding speed (v) was 480μm/s and the temperature was at the room temperature (T=25°C). AThe number of strokes was determined at N=20, 40, 50, 80, and 100, as shown as the plots in Figure 3.7. In the figure, the red line is for the square-shaped structures and the blue line for the line-shaped ones. As increasing the number of strokes, the height of the nanostructures was also increased. The fact that the height of a line is higher than that of the square is due to the amount of material transfer. For line-shape, the material is built up faster than otherwise. The difference started to

show after 40 strokes. It indicates that the buildup took place only after sometime due to activation of surface molecules.

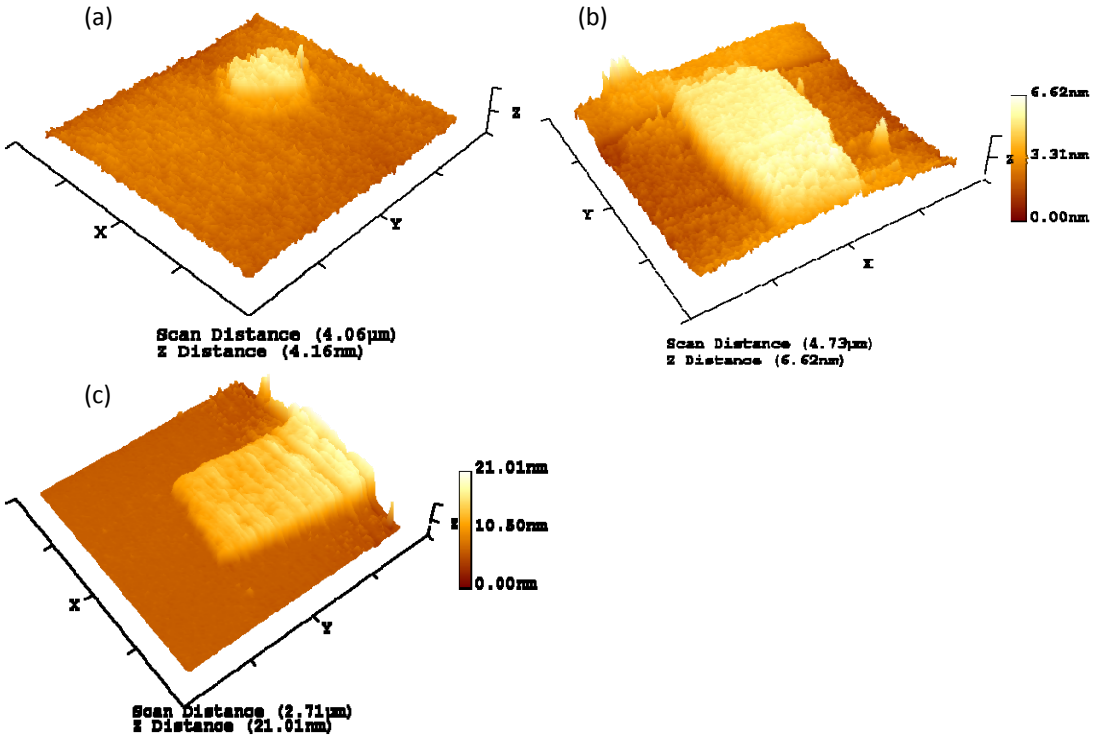

Figure 3.6. The AFM images are for nanostructures fabricated by SPAN process with different strokes (N). (a) N=50 (b) N=80, and (c)N=100.

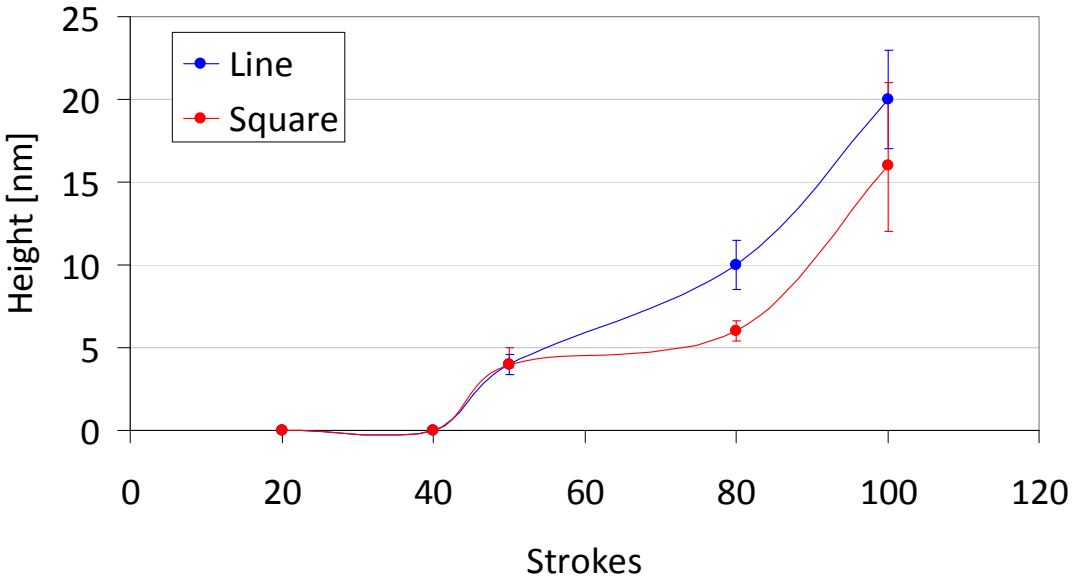

Figure 3.7. The effect of the number of strokes on nanostructure height. The red line is for the square-shaped structures, and the blue line for the line-shaped ones. Those results were obtained with fixing the other conditions at v= 480μm/s and T=25°C.

B. Sliding speed (v)

AFM can control precisely the sliding speed and distance of its probe. Equ.2 shows the relationship between friction and normal force.

$$f_f = \mu F \qquad \text{----------} \qquad \text{(Equ.2)}$$

where f_f and F are friction and normal force respectively. μ is the friction coefficient. According to Equ.2, the friction is not dependent on sliding speed. However, our results showed that the contact-sliding speed affects on fabricating the nanostructures. Figure 3.8. shows the effect of the sliding speed on nanostructures. The contact-sliding speed (v) was 250, 340, and 480μm/s. The sliding strokes and temperature were fixed at N=40 and T = 50°C, respectively. The higher the speed, the thicker the nanostructures. The sliding

speed is not directly affecting the friction. Instead, it enhances the material (Au) transfer to the Si substrate.

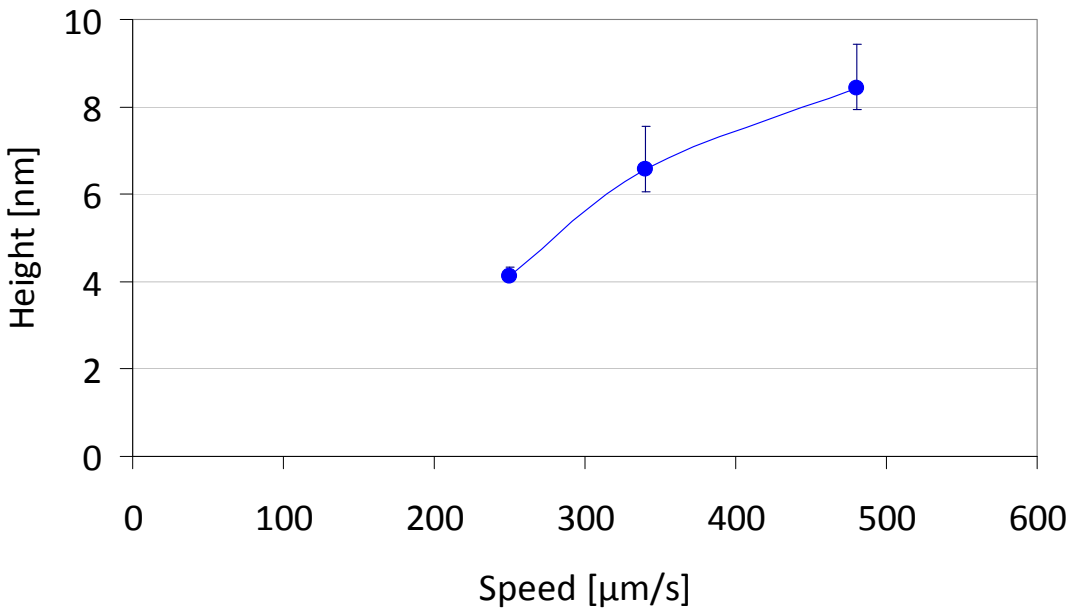

Figure 3.8. The effect of the contact-sliding speed (v) on forming the nanostructures. The sliding strokes and temperature were fixed at N=40 and T = 50°C, respectively.

C. Surface temperature (T)

The sample surface temperature is controlled using a heating element. To increase the efficiency of the process, the sample stage is heated up to 100°C. As shown in Figure 3.9, the temperature of the sample surface affects the height of nanostructures. It's expected that the thermal energy enhances the interfacial interactions between Au and Si through eutectic reactions. Details will be discussed later.

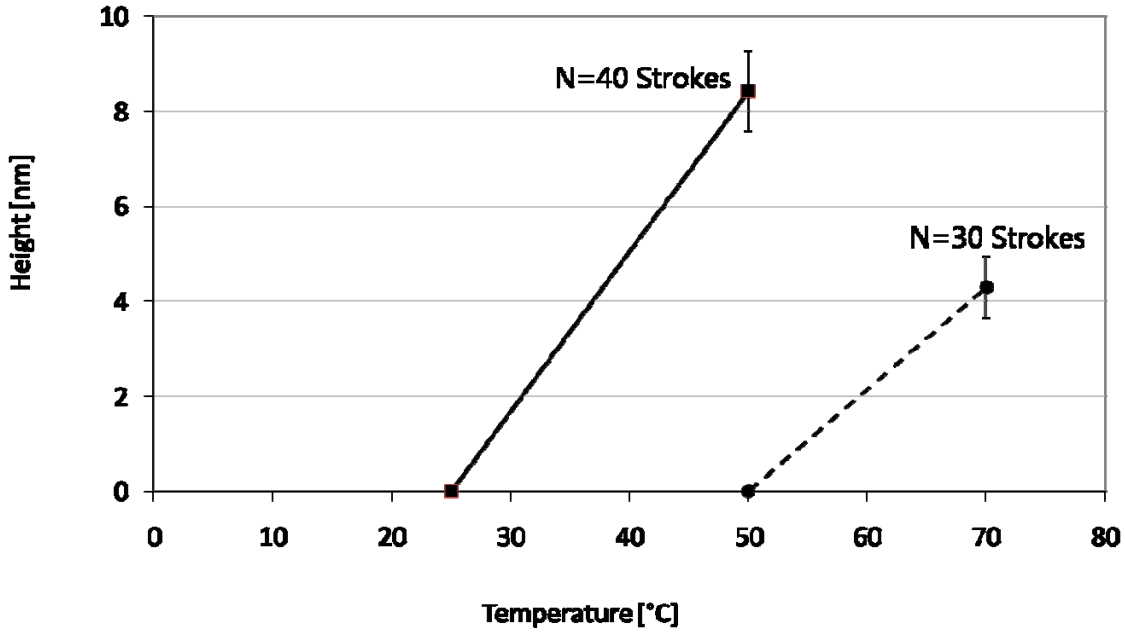

Figure 3.9. Temperature effects on SPAN fabrication of the nanostructures. The speed (v) was fixed at 480μm/s, but the number of strokes (N) and temperature (T) were changed. For the solid-line, temperatures were 25 and 50°C at N=40. The dashed-line on the plot was obtained with the conditions; N=30 and T=50 and 70°C.

D. Down-force (F)

As mentioned in the above (Equ.2), the normal force of the probe against the substrate is affecting on friction critically. The down-forces are calculated and discussed with the cantilever deflection and the probe properties. According to Equ.2, the down-force of the probe is affecting on friction directly.

Two different forces are investigated. The line and dot structures in Figure 3.10 were obtained with F=503.1 and 166.7nN, respectively at v=480μm/s, N=100, and T=25°C.

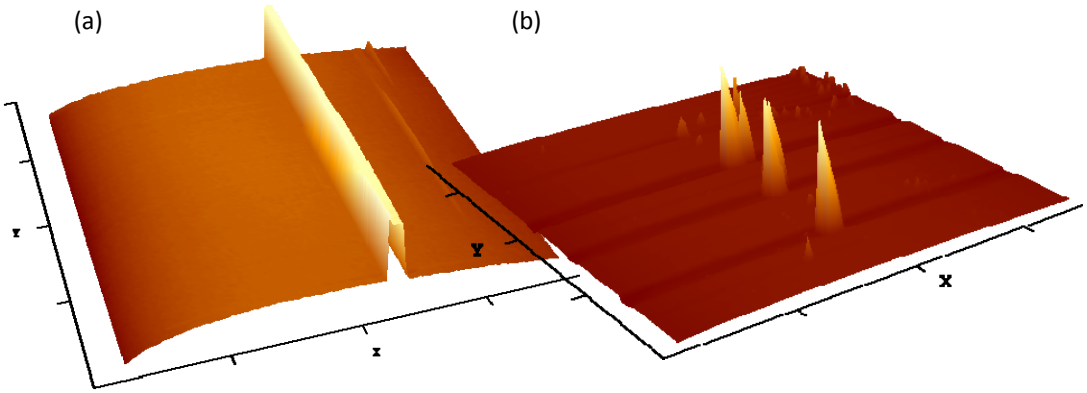

Figure 3.10. Two different down-forces (F) are applied; (a) 503.1 and (b) 166.7nN.

The Au-coated probe was first brought into physical contact with a single-crystalline Si (100) surface. At this stage, there is no stress on the cantilever and the probe stage is considered to be at a neutral height. The probe stage is then brought down 15.48μm closer to the substrate causing a deflection of the probe cantilever.

The deflection δ of the cantilever is expressed as

$$\delta = Fl^3/C_1EI \quad \text{----------} \quad \text{(Equ.3)}$$

where F the bending force, l the length of cantilever, C_1 the geometry constant (=2), *E* the Young's modulus and I the moment of the cantilever.

The bending force can be can be solved from (Equ.4),

$$F = \delta C_1 EI/l^3 \quad \text{----------} \quad \text{(Equ.4)}$$

The length of the cantilever is 320μm. Young's modulus of the Si_3N_4 probe is assumed to be 224.6GPa. The moment I is calculated by equation (Equ.5)

$$I = bh^3/12 \quad \text{----------} \quad \text{(Equ.5)}$$

where the width of cantilever *b* is 87.5μm, the thickness of the cantilever *h* is 0.69μm resulting in a moment of of $2.37 \times 10^{-24} m^4$. Hence the down force *F* applied for the nanobelts is 503.1nN and 167.7nN for dots.

SPAN is a new method to fabricate nanostructures using AFM which has advantages to overcome the problems of STM. Although a STM has advantages of high resolution and precise control, it still has disadvantages. It needs to operate in a vacuum system, and the substrates for this process have to be conductive materials. Another critical limitation is the efficiency of the processing. The processing speed is lower than other bottom-up methods. The nanowires fabricated by STM are neither uniform nor repeatable. To overcome those disadvantages of STM, AFM is suitable to fabricate nanowires with high-throughput and reproductivity. The SPAN process is based on a STM and can write a nanostructure on a substrate using AFM. Fabricating a nanostructure on a desired area is easy due to an easy control system of AFM without any vacuum system. The nanowire length is not limited with SPAN. The processing speed is improved by controlling parameters (N, T, v, F). The uniformity and reproductivity of the nanostructures were also increased. This will be discussed more detail in Section 5, Mechanisms of SPAN.

4. NANOSTRUCTURE-PROPERTY RELATIONSHIPS

This section discusses the properties of nanostructures generated using the SPAN. The characterization techniques are discussed following the experimental results. The effects of nanostructures on properties of the same are discussed at the end of the section.

4.1. Characterization

A field emission scanning electron microscope (FE-SEM, LEO 1530 VP) and a scanning electron microscope (SEM, JEOL T330) were used to characterize the gold-coated probe before and after contact-sliding experiments, as shown in Figure 3.5. The total height of the tip, including the coating, was 8μm, and the base of the tip was a square shape with side of $8\times8\mu m^2$. The images were obtained at a magnification of ×7,500 with the accelerating voltage 30kV. The wear scar diameter was measured from the SEM images.

The properties of the fabricated structures include the physical size, roughness, hardness, electrical conductivity, and adhesion. The hardness was characterized by using a nanoindenter (Hysitron TriboIndenter). The nanoindenter could provide the submicron scale measurement for the hardness with real-time data. Mechanical properties such as roughness, adhesion, and size of the microstructures were measured using the AFM. Adhesion forces were characterized by using the AFM standard (Si_3N_4) tips for both tip and substrate materials. Roughness and physical dimension of the microstructures were estimated using the close-contact mode AFM tips. The properties of the processed probes and substrates were characterized by using the nanoindentation, the energy dispersive X-

ray spectroscopy (EDS), the transmission electron microscopy (TEM), and the scanning electron microscopy (SEM) techniques. The same AFM, with a different problem was used to characterize the topography and phases of the substrate surface. To prevent any damage on the sample surface, a non-contact mode probe was used for the analysis. Electrical properties of nanostructures were obtained by using an AFM conductive probe in the same setup. The configuration is shown in Figure 4.1. The conductive probe was operated in a contact mode to drive electrical current flow through. A picoameter was employed to record the electrical current in real time.

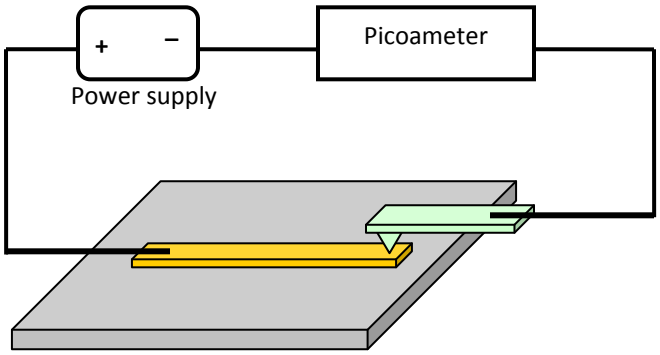

Figure 4.1. Experimental setup to characterize the electrical properties of the patterns.

4.1.1. Atomic Force Microscope (AFM)

AFM can obtain the surface properties, such as topography, phase, or conductivity. The AFM probe size is fitted to characterize nano-scale properties so that the nanoscale features can be imaged. Additionally, the AFM has a function to measure the adhesion force between a sample and the AFM probe. The adhesion force is calculated from a force-distance curve of the probes. That's how to get AFM images and mechanical

properties of the nanowire. Moreover, the AFM provides a way to characterize the electrical property of the nanowires. The AFM conductive probes can be utilized to measure the conductivity of the nanowires, because the curvature radius of the probes is less than 15nm. The I-V curve of the nanowires can be plotted by AFM conductive probes.

4.1.2. Scanning Electron Microscope (SEM)

The AFM probes are expected to be changed before and after the process of SPAN. SEM will be usable to investigate the probes. Figure 4.2 shows two SEM images of AFM probes. The first SEM image is an AFM original probe which is not coated with gold. The material of the original one is Silicon Nitride (Si_3N_4). The right side SEM image is an Au coated AFM probe.

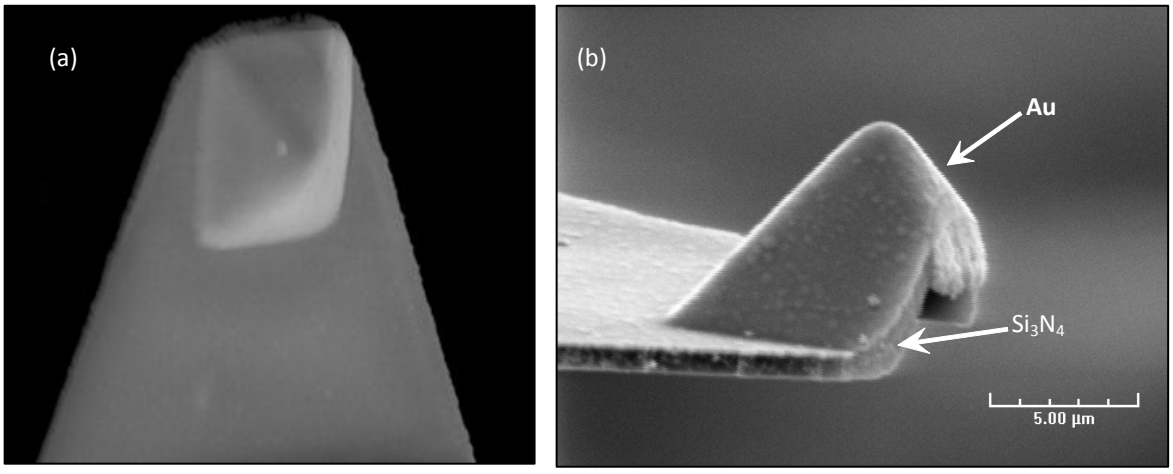

Figure 4.2 SEM images of AFM probes before and after coating gold on it, (a) and (b) respectively.

The Au-coated probes will slid on silicon substrates during the SPAN process. After sliding, the probes should be changed. It will be investigated in details by using an SEM.

4.1.3. Nanoindentation

Mechanical properties will be obtained. A Hysitron Nanoindenter will be used to measure the hardness of the nanowires. The machine is a low load nanomechanical test system. The diamond tip of the machine is indented on the nanowires gradually. It will display the load of the diamond versus displacement of the nanowires which is called a load-displacement curve. The machine calculates hardness and elastic modulus of the nanowires from the curves.

4.1.4. Transmission Electron Microscope (TEM)

The atomic resolution of the nanowires will be achieved by TEM (JEOL JEM-2010). The imaging resolution of the machine is 0.23nm. Diffraction patterns of the nanowires will be obtained to investigate the atomic structures of the nanowires. Also, the interfacial areas between the nanowires and silicon substrates will be resolved. The machine has the Energy-dispersive X-ray spectroscope (EDS). EDS is usually used for the elemental analysis or chemical characterization. The compositions of the nanowires will be investigated by EDS.

4.1.5. TEM Sample Preparation

TEM samples were prepared for interface analysis of the substrates and nanostructures. The procedure of preparing the TEM samples is shown in Figure 4.3 (a-f). First two substrates (gray-colored) with the formed nanostructures (yellow color) were prepared as described in the previous section, shown in Figure 4.3(a). The two substrates were glued together (Figure 4.3(b)) with the nanostructures facing each other. The glue (red color) filled the voids between the two substrates. The sample was ground until it reached a length of 60μm, as shown in Figure 4.3(c). Dimpling was processed until the thickness reached 20μm, as shown in Figure 4.3(d). An ion miller (Precision Ion Polisher System 691, Gatan) oriented as shown in Figure 4.3(e) was used to make a hole at the center of the sample. The hole was used to verify that the appropriate thickness of 20nm was obtained for TEM analysis. One of the TEM samples was shown in Figure 4.3 (f). The outer ring was a sample holder protecting the two substrates.

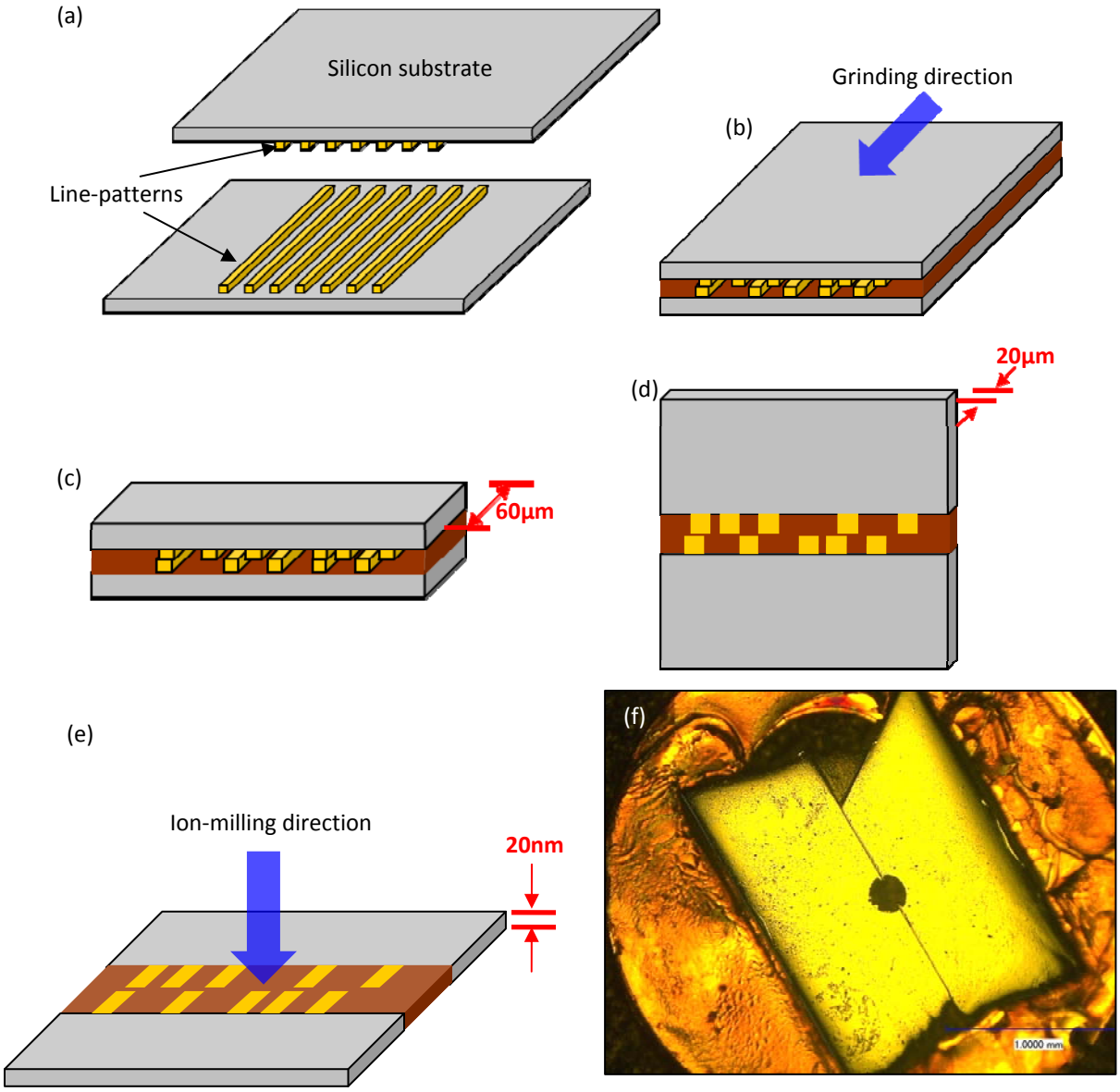

Figure 4.3.The procedure of preparing the TEM samples is shown in (a)-(f). (a) Two substrates (gray-colored) having the patterns (yellow) were prepared. The substrates were glued together. (b) The length of the sample got smaller by grinding along the direction (arrow). (c) When the sample got 60μm in length, dimpling was started. (d) Dimpling stopped at the length of 20μm. (e) An ion miller was used to make a small hole at the center of the sample by emitting ions on the side of the substrate as the arrow. The final thickness of the sample around the hole was 20nm. (f) The real TEM sample was taken by a microscope. An outer ring round the sample was a sample holder protecting the two silicon substrates separated.

4.2. Nanostructures

After a number of contact-sliding strokes, the Au-coated probe was observed and it showed a visible wear scar (Figure 4.4). Under the SEM, the scar is smooth with neither fracture nor a large area of Au material pullout.

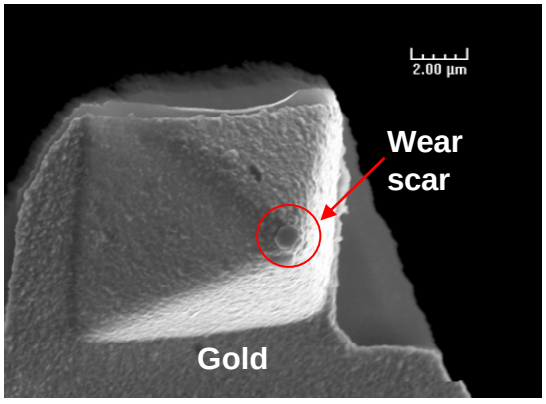

Figure 4.4. SEM image of an Au-coated AFM tip after sliding-contact experiments.

On the Si surface, there are some microstructures formed. Figure 4.5a shows a square grown due to sliding of Au probe on Si in the area of $1.5\times1.5\mu m^2$. A standard Si_3Ni_4 probe was also used to slide on the Si sample in a designated area. Comparing the grown-square fabricated by Au probe, the square area on Si scanned by the standard Si_3Ni_4 was not grown as shown in Figure 4.5b. After the first few strokes for line sliding tests with the Au-coated probe, discontinued dots were found on the Si surface (Figure 4.6a). A line started to form connecting the aligned dots with different height. The peaks outside the line are thought to be debris on the original Si surface. After 80times contact-sliding, a continuous line formation is observed on the Si surface (Figure 4.6 b-d). The morphology image (Figure 4.6b), phase image (Figure 4.6c), and the 3D image (Figure

4.6d) show a clean and straight line. Another line-structure was fabricated with the same conditions shown in Figure 4.7. The structure was also observed by AFM. The top-view, phase, and 3D images are shown in Figure 4.7 (a), (b), and (c) respectively. The top portion of the line (Figure 4.7c) is slightly narrower than that at the bottom. The width of the line-structure is about 600nm and the height is 12nm.

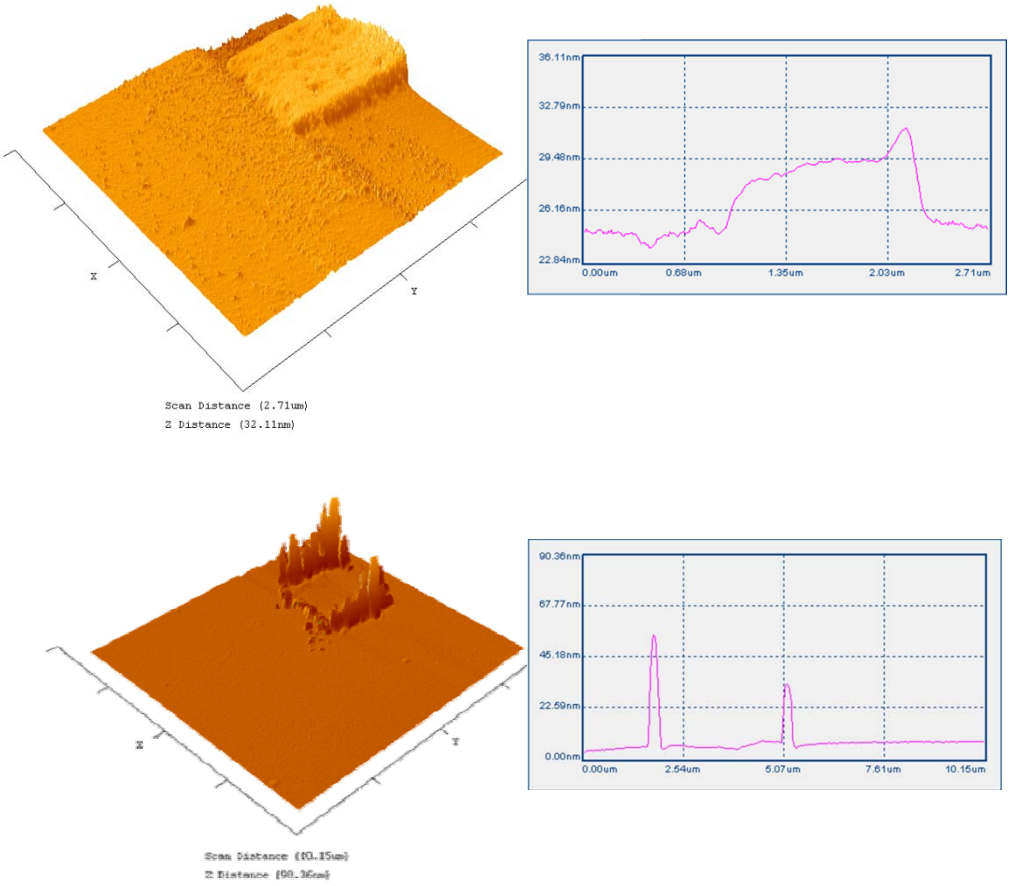

Figure 4.5. 3D AFM image and profile (left to right) (a) A square pattern was grown by sliding of Au-coated probe at room temperature. (b) The square contact-sliding area of Si was not affected by sliding of Si_3Ni_4 (normal) probe.

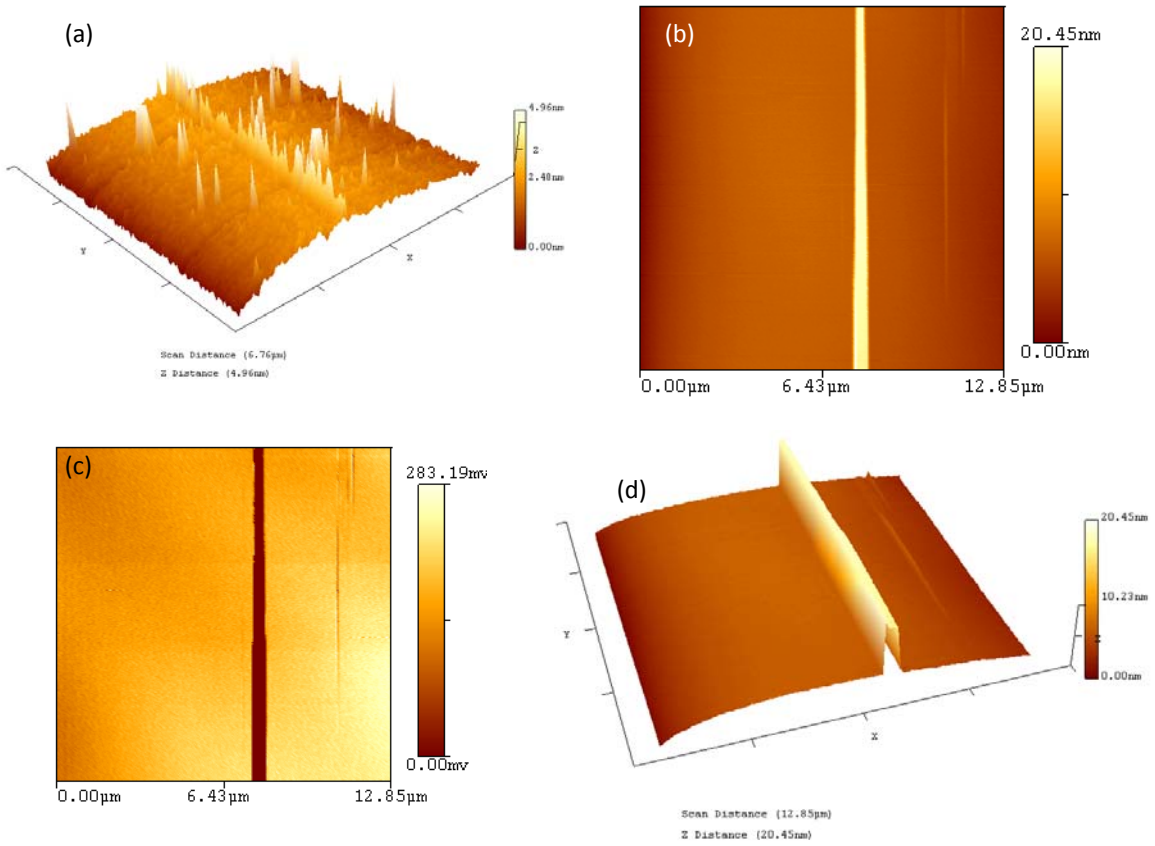

Figure 4.6. AFM images of line-structures formed on the silicon substrate. (a) Initial stage of line-forming. (b) Top view of the line structure. (c) Phase image showing the width variation. (d) A 3D view.

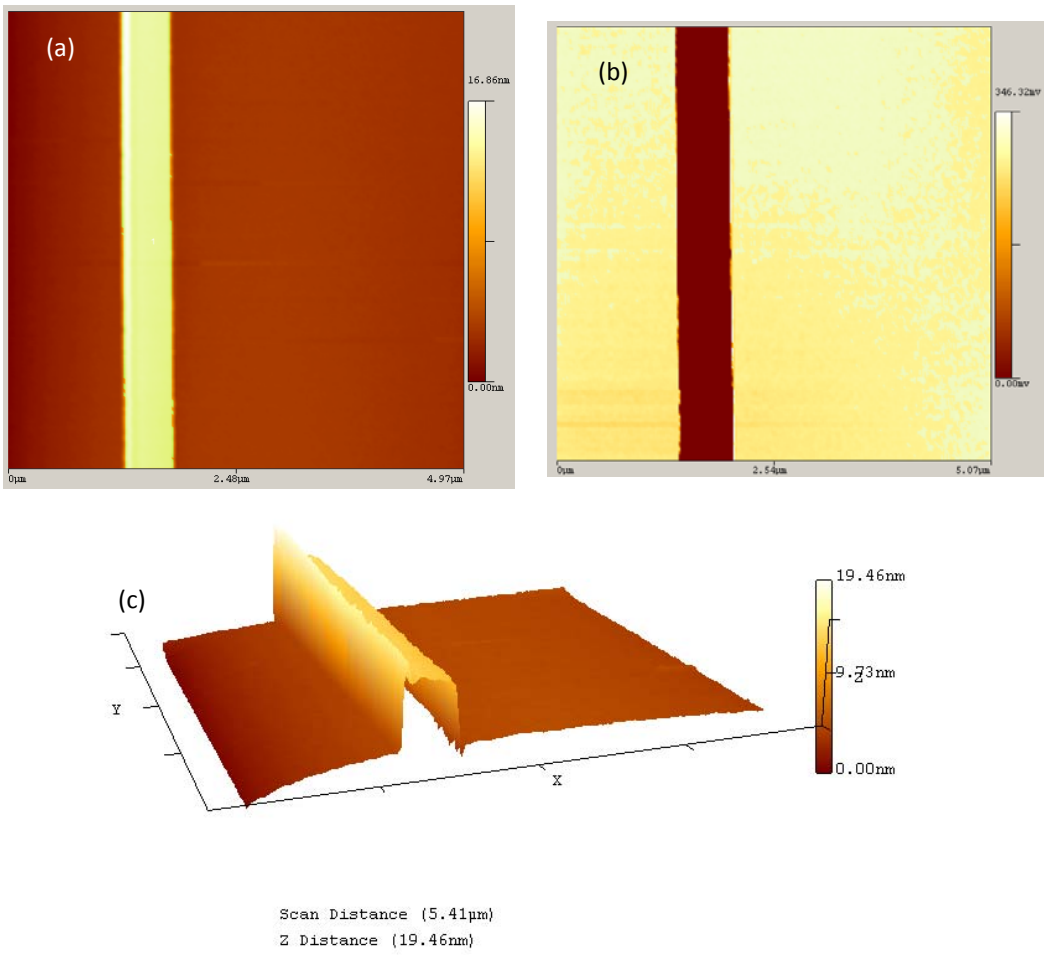

Figure 4.7. The line-structure was observed using an AFM. (a) Morphology image. (b) Phase image. (c) The 3D image.

A non-contact mode AFM probe was used to characterize the morphology of the nanostructures created. Figure 4.8 shows a SEM image and a line-shaped structure formed by the SPAN process. The SEM image in Figure 4.8 (a) is the AFM gold-coated probe after the sliding test. The gold on the probe was transferred to the substrate to form the structures. The gold-coated probe revealed wear as demonstrated by the blunt tip shown in Figure 4.8(a). The transferred gold can be identified on the nanostructures by EDS. It will be discussed in the next section. The AFM images in Figure 4.8 (b, c, and d) show the height, profile, and 3-dimensional images of a nanobelt formed by the process. The nanostructure was created by sliding the probe with an initial 503nN down-force and 480μm/s for 80 strokes. The structure has 10nm height and 600nm width which coincides with the width of the worn surface of the probe in Figure 4.8(a).

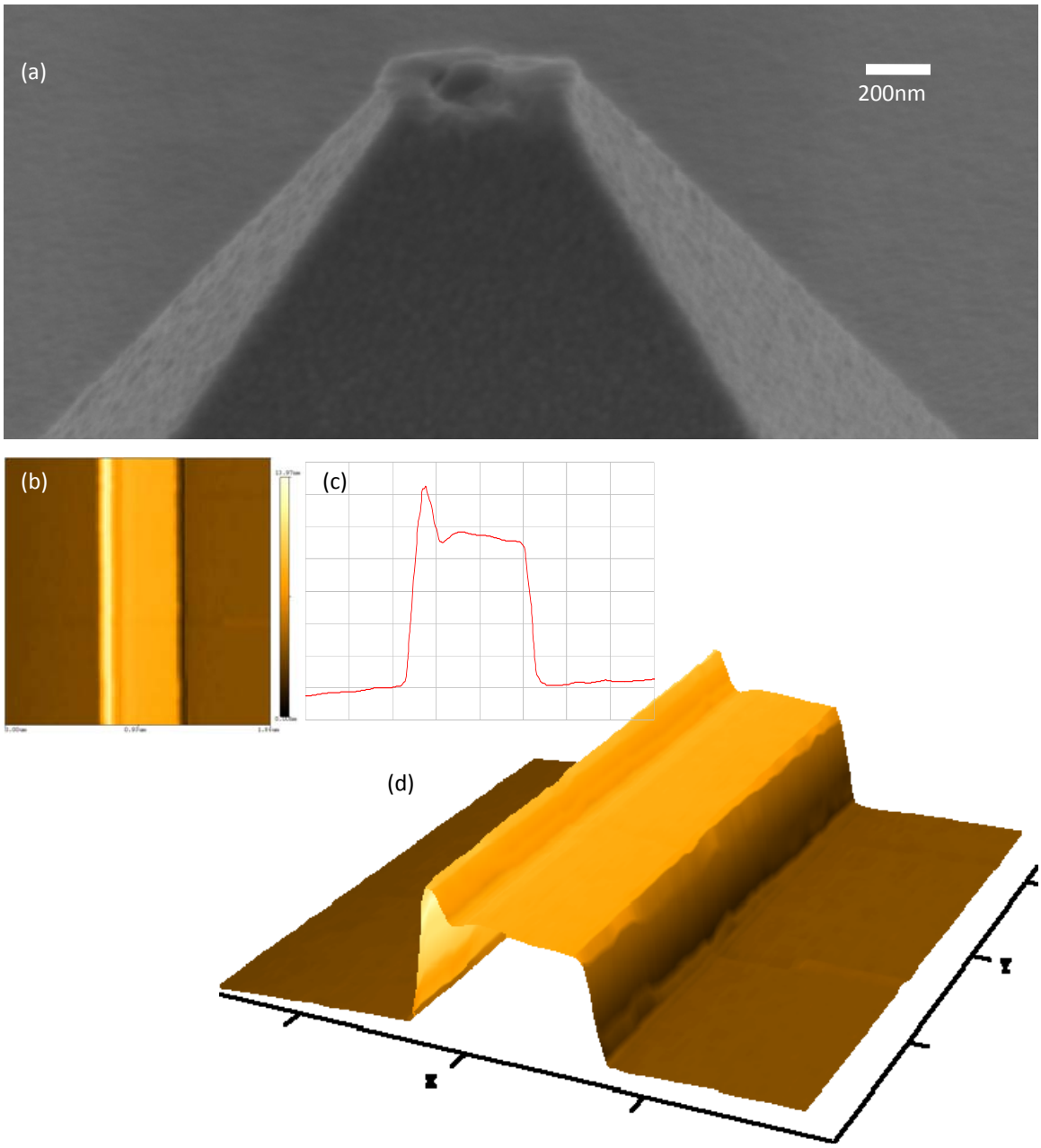

Figure 4.8. SEM and AFM images after test. (a) SEM image of the gold-coated probe after a contact-sliding test. AFM images of the nano-sized line on the Si substrate; (b) topology, (c) profile, and (d) 3D AFM image. The dimension of the line is 10nm high and 600nm wide.

The down force of the probe could not be measured during the test due to the limitation of the equipment. The down force was calculated by the tip deflection and will be discussed later. Another test was conducted with the same conditions as the previous test, except the down-force of the probe was reduced to one-third. The sliding with these conditions formed dots instead of a nanobelt.

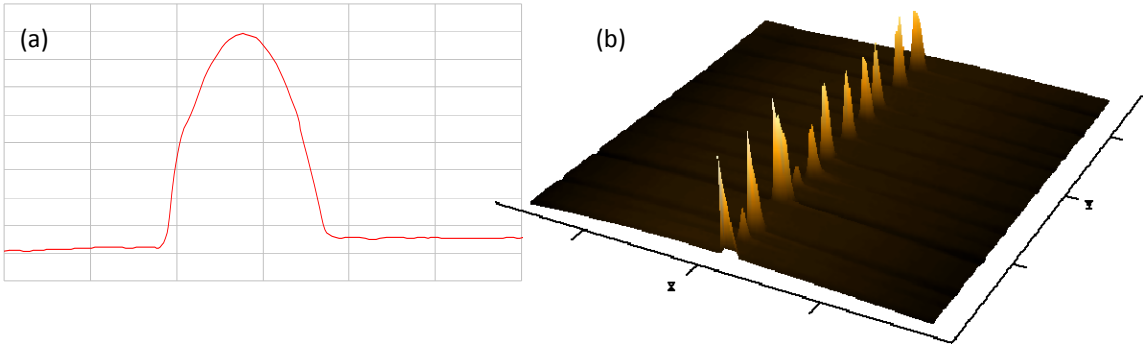

Figure 4.9. A series of dots fabricated by an intermittent-contact test. (a) a profile shows the height and width of one of the dots; 153nm high and 400nm wide. (b) a 3D image of the dots along the sliding direction of the probe.

Figure 4.9 (a) shows the profile of a dot. The height and width of the dot were 153nm and 400nm, respectively. The dots were laid along the sliding direction of the probe as shown in Figure 4.9 (b).

4.3. Effects of Applied Potential on Nanostructures

The SPAN technique was verified to fabricate various shaped patterns. The sliding tests were conducted to fabricate the Texas A&M University logo "$_{A}T_{M}$" on the substrate,

shown in Figure 4.10. For the tests, electrical potential of 12V was applied between the substrate and the probe. Figure 4.10 is the results of the tests. The pattern, ${}_{A}T_{M}$, is shown in Figure 4.10 (a) and the 'A' letter of the pattern was enlarged in Figure 4.10 (b).

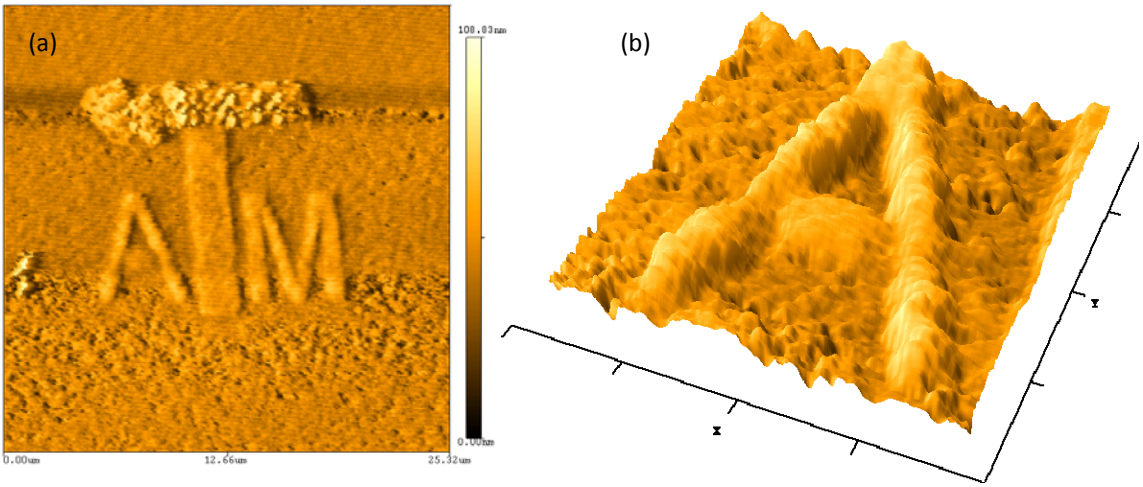

Figure 4.10. ${}_{A}T_{M}$ formed by the contact-sliding test with electrical potential (12V). (a) AFM height image of the pattern. (b) Enlarged image for 'A' letter of ${}_{A}T_{M}$ pattern.

The ${}_{A}T_{M}$ pattern in Figure 4.10 was fabricated with the same conditions as the nanobelt but with one addition. An electrical potential of 12V were applied between the probe and the substrate during the sliding tests. In both Figure 4.8(d) and 4.9(b), the width of the structures is approximately 600nm. The smallest width of the pattern (Figure 4.10) formed with the electrical potential is 800nm. The applied electrical potential leaded the structure wider. Electrical adhesion, defined by McLean [147], was originated at the contact point due to highly concentrated electrons. Here, the applied electric field is highly localized at the contact area of the probe on the substrate. The large electrical

adhesion was induced due to the highly intensified electrical strength between the two materials. According to the theoretical equation,

$$\sigma = (\varepsilon_0\varepsilon_a/8\pi)^{1/3}[VEd/\pi D^2(1 - v^2)]^{2/3} \quad \text{----------} \quad \text{(Equ.6)}$$

the electrical adhesion stress σ could be increased with the electrical potentials [148] where ε_0 is the permittivity of free space, ε_a the average permittivity, V the applied electrical potential, E the young's modulus of the probe material, d the contact diameter, D the contact length on substrate, and v the Poisson ratio of the probe. The adhesion force was increased on the highly localized contact area by electrical adhesion. This further enhanced the gold material transfer resulting wider patterns.

4.4. Volume

Our results showed that the Au material on AFM tips was transferred by sliding. The amount of transferred material was compared with the loss of the coated material (Au) on AFM tip. The sliding experiments were conducted in extended sliding lengths (80, 120, and 160μm) for accurate estimation. As shown in Figure 4.11, the volume of the wear scar of Au-coated tip (gold loss volume) was 5.65, 9.48, and 12.01μm^3 at the contact-sliding distance of 80, 120, and 160μm respectively. However, those of grown lines on Si substrate were 6.85, 10.28, and 13.7μm^3 at their respective distance. These results showed that line-structure volumes on the Si surface are larger than the gold loss of the tip. This might mean the existence of a different type of material in the generated line-structures. Further evidence was sought in continued characterization.

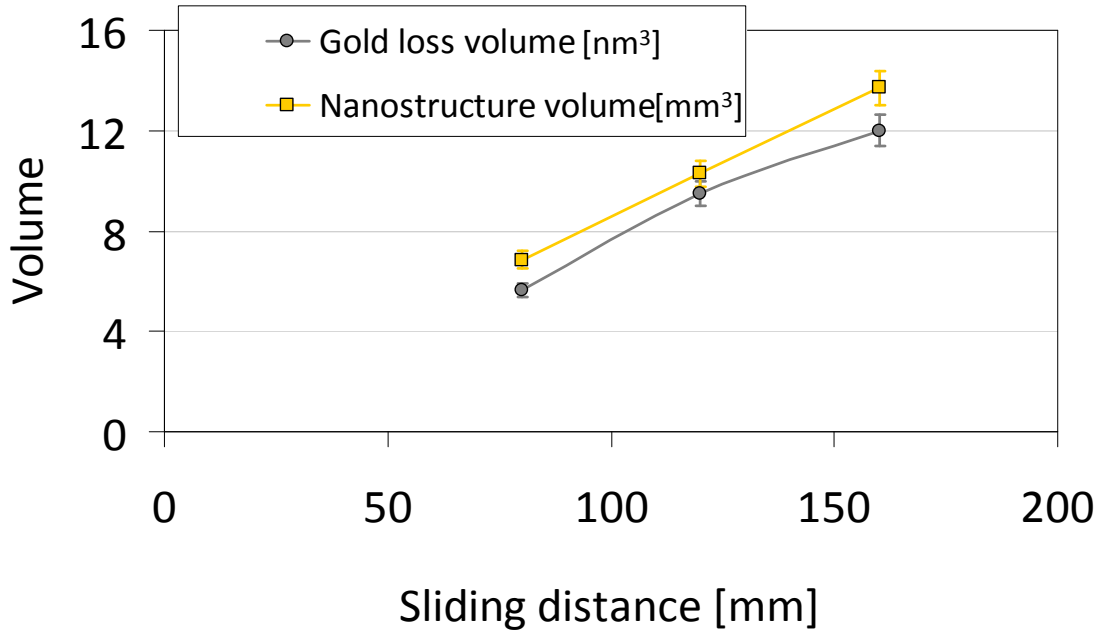

Figure 4.11. The extended experimental data comparing the wear scar (gold volume) on the Au-coated AFM tip with line-structure volume verses the sliding distance.

4.5. Surface Properties

Hardness, Roughness, and Adhesion are discussed here. To compare the line-structures with Si substrate, mechanical properties were characterized. Roughness was characterized by the AFM which was used for sliding tests. Roughness of Si and the line-structure were 2.22 and 0.7nm. The surface was smoothened by sliding the AFM tip on it. Hardness was measured by a nanoindenter. Hardness of Si was 150GPa while the line-structures were 78GPa. Although the roughness of the line-structures was smoother than that of Si, the structures have the lower hardness value than Si. Adhesion force was calculated with the force-distance curve for the AFM tip and the sample surface. The line-structures and Si have their adhesion value, 217.74 and 213.68nN respectively.

4.6. Electrical Conductivity

To understand the nature of microstructures, we conducted electrical conductivity measurement using the AFM. Electrical potentials were applied and the current flew through a conductive AFM tip to the small lines. One end of the line was applied to the negative electrical potential while the probe was with a positive (+12V). Figure 4.12(a) shows the experiment setup to measure the conductivity. The conductive AFM tip was scanned by reciprocating between the silicon and the line regions on the surface as shown Figure 4.12(a). The current was generated during scanning. The amplitude of the generated current was different with the conductivity of the surface. The flown current throughout the line and the AMF tip was displayed by a picoameter, recorded and plotted by LabView program on a computer. Figure 4.12(b) is its result. The y-axis is the amplitude of the current and x-axis is the scanning time up to 1 second. The peaks were occurred when the probe was on the line-microstructure during scanning. There was no peak for the probe on the Si substrate. The average currents flowing on gold line and silicon surface are 11.22μA and 0.41nA respectively.

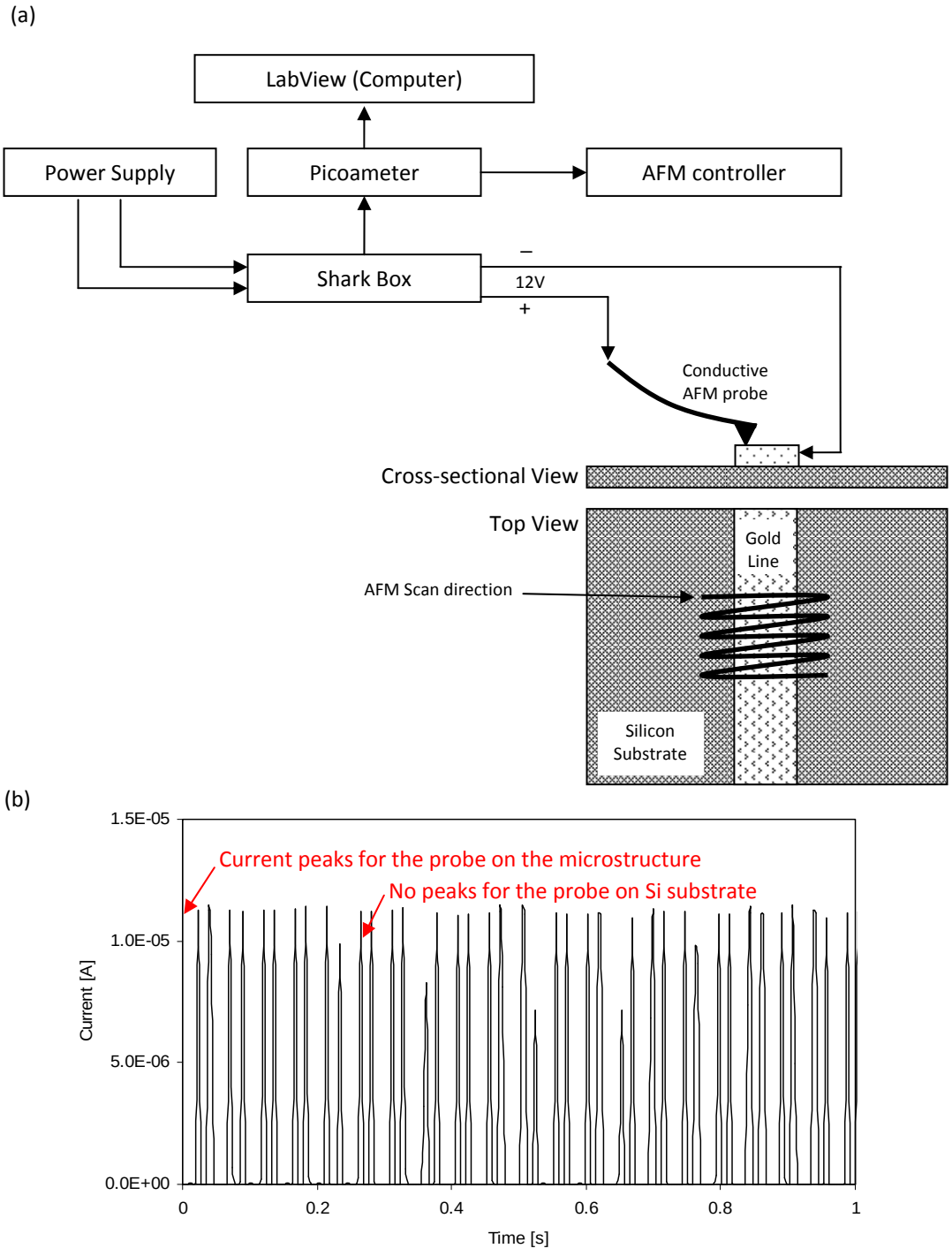

Figure 4.12. Electrical conductivity measurement. (a) The simple diagram of the experimental setup to measure the conductivity. (b) Current flowing throughout the line-structure. During scanning, the current peaks were occurred when the AFM conductive probe was on the microstructure; no peak for the probe on Si substrate.

Electrical properties of the nanostructure in Figure 4.8 were characterized using an AFM conductive probe. As shown in Figure 4.1, an electrical potential was applied between the nanopattern and the probe to observe the conductivity of the structure. The output current was measured and recorded by a picoameter.

Figure 4.13 shows the measured current as the probe scanned across the width of the structure. The x-axis is for the position [μm] of the scanning probe across the sample and the y-axis for the output current [A]. The insert in Figure 4.13 is the height profile of the nanostructure used for electrical property measurements. The average current value of the nanostructure is 1.07×10^{-3}A. On the other hand, when the probe was in contact with Si, the current was about 0A. I-V curves of the nanopattern, Si substrate, and pure gold were also obtained using the same setup, varying the potential from -2 to 2V with 0.01V increments. The current flow of the Si substrate (blue line in Figure 4.14) was about 0A. The conductivity of a pure gold layer deposited by sputtering methods on a Si substrate (green line) shows a linear and high response to changes in voltage. However, the output current for the nanostructure (red line) exhibited a nonlinear response due to a semi-conductive property caused by the alloying during the SPAN process.

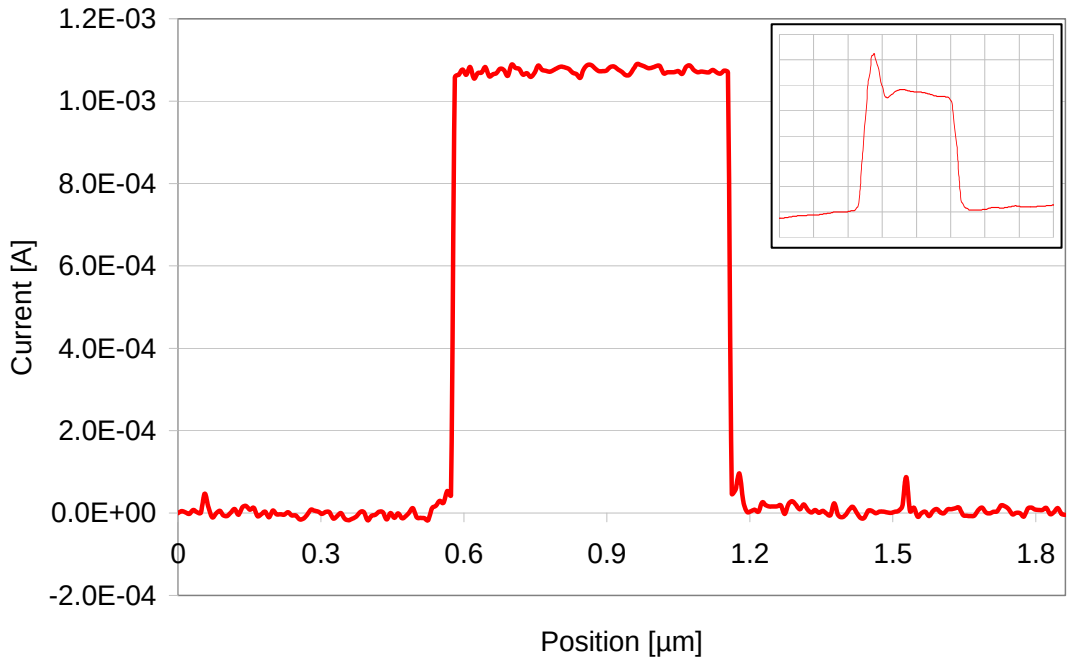

Figure 4.13. The profile of output current [mA]. When an electrical potential (12V) was applied to the nanostructure, the electrical current flowing through was recorded. The average current is 1.07×10^{-3}A. The inset of the figure is for the profile of the nanostructure (cross-sectional view of the structure).

As shown in Figure 4.14, the conductivity of the nanostructures formed by the SPAN process was compared with the substrate and a pure gold layer. The pure gold layer has the resistance of 2.88Ω. The current of the pure gold layer increased proportionally with the input voltage. On the other hand, the output current (red-line) for the nanostructure was increased nonlinearly while the input voltage was increased linearly.

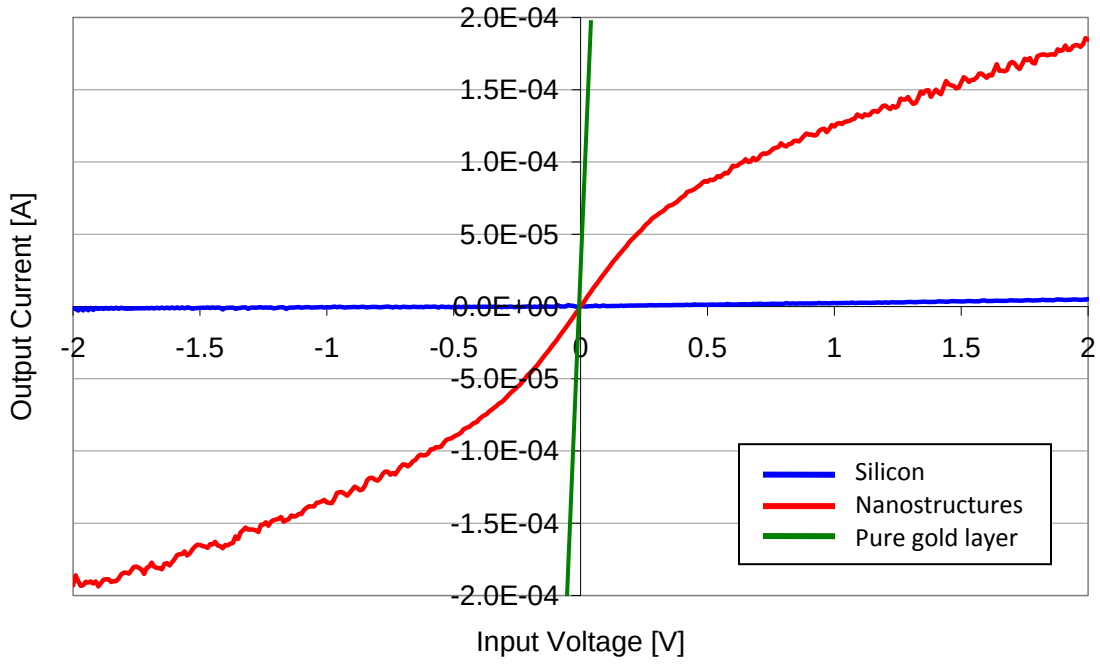

Figure 4.14. I-V curves of the nanopattern and a Si substrate. For each material, the applied electrical potential was increased from -2 to 2V with 0.01V step. The current (blue-line) flowing throughout Si substrate was about 0A, but the slope of I-V curve of the pure gold layer is very high. Meanwhile, the output current (red-line) for the nanostructure was increased nonlinearly even though the input voltage was linearly increased. The resistances of the nanostructure are R_{low}=5kΩ and R_{high}=14.3kΩ, respectively.

5. MECHANISMS OF SPAN

5.1. An Alternative Nanolithography Process

In the present study, a new method to fabricate nanostructures, so called SPAN, has been developed. The SPAN method is similar to writing on a paper with a pencil. The coated-AFM probe acted as a pencil. This process is different from any other AFM based methods in that the nanostructure is created from an alloying effect of two materials. The SPAN can be seen as a combination of the AFM Oxidation lithography and the dip-pen lithography without the metallic ink. AFM Oxidation lithography applies electrical potentials without a mechanical force to form a nanostructure.

A probe of 10nm (±5nm) diameter is used for the SPAN method. The Hertzien contact pressure is about 6.4nN/nm^2, consistent with previously reported data [149, 150]. The surface tension (γ) of silicon is 700mN/m, and the force F is followed the previously reported equation; $F = 4\pi r\gamma \cos(\theta)$ where r is the probe diameter and θ is the contact angle of probe to the surface which is approximately 0. The sliding leads to friction and shear of the tip [151, 152]. The frictional energy introduced through sliding is transferred to the thermal energy increasing the temperature at the tip, referred as the flash temperature [153, 154]. At a certain temperature, the tip material is transferred to the substrate and the two materials form an alloy together at the nanoscale [155, 156]. The down-force of the probe leading to friction and shear is an important factor for the process.

There are other factors affecting the dimension of the nanostructures: the shape of the probe and the surface roughness of the substrate. With observation of worn AFM probes (results not shown), the tip of the AFM probe was a sharp pyramidal shape as shown in Figure 5.1.

Figure 5.1 is the simple diagrams for the probe before gold coating, after coating before the sliding test, and after the sliding test. The curvature of the tip was 100nm after gold coating. After sliding, the wear of the tip caused the end to become blunt. The nanostructures had the corresponding shape of the probe as shown in Figure 5.1(c). The Au coating on probe was worn out due to contact-sliding. However, it did not expose the original AFM probe (Si_3N_4) as demonstrated by EDS analysis of the probe (Figure 5.1(d)) and nanostructure (Figure 5.2). Nitride (N), one of the materials of the original AFM probe, was not found on either probe or nanostructures. Figure 5.2 shows that the nanostructure is not purely gold, rather it was composed of 72.7%wt. Si and 27.3%wt. Au.

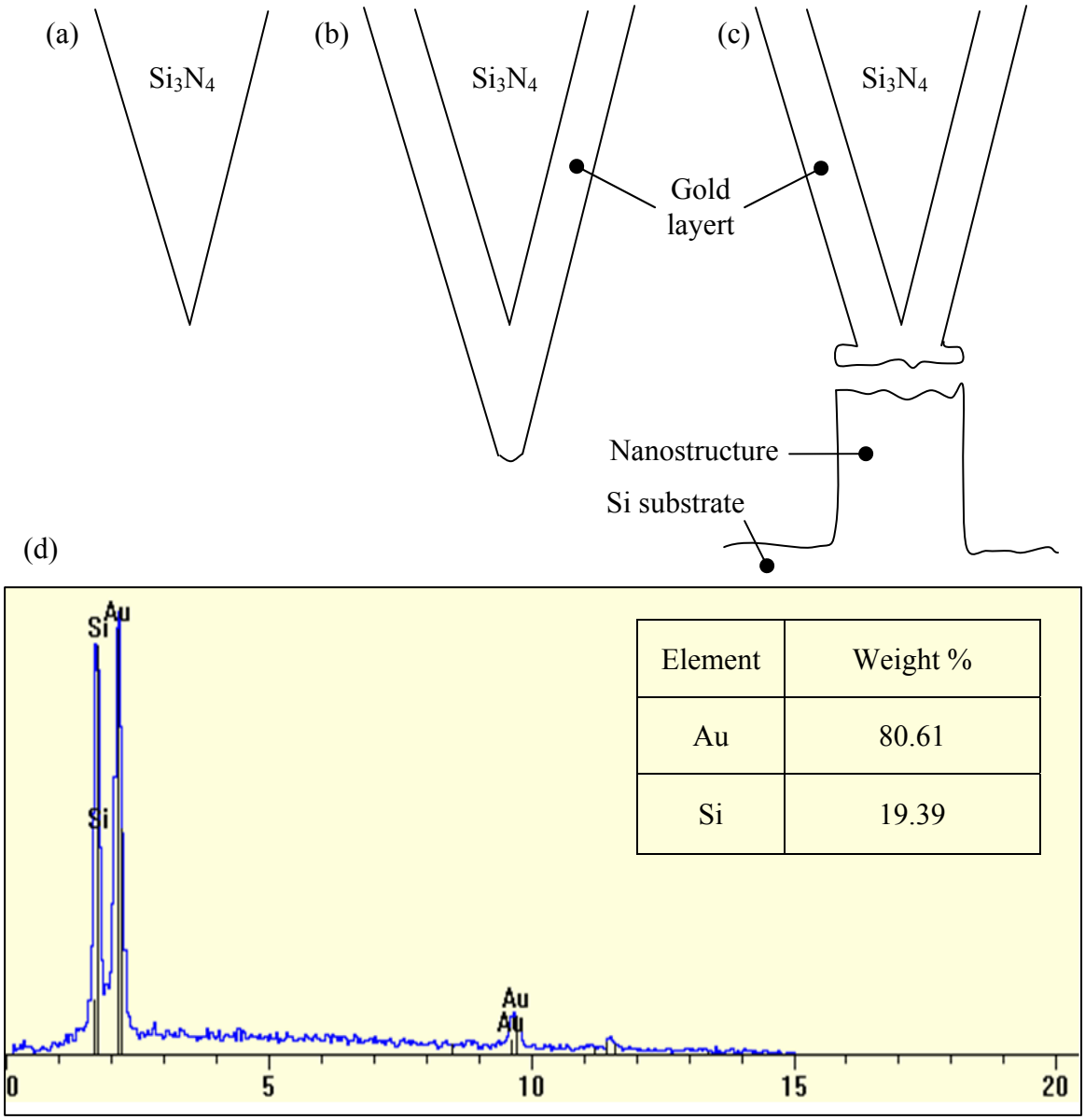

Figure 5.1. Schematic diagrams for the AFM probe (a) before gold coating, (b) before the sliding test with coating, and (c) after the test. The nanopatterns on the substrate were built by sliding the coated probe. As shown in (c), the nanostructures had the corresponding shape of the probe. (d) is the energy dispersive x-ray spectroscopy (EDS) analysis for the probe after sliding test.

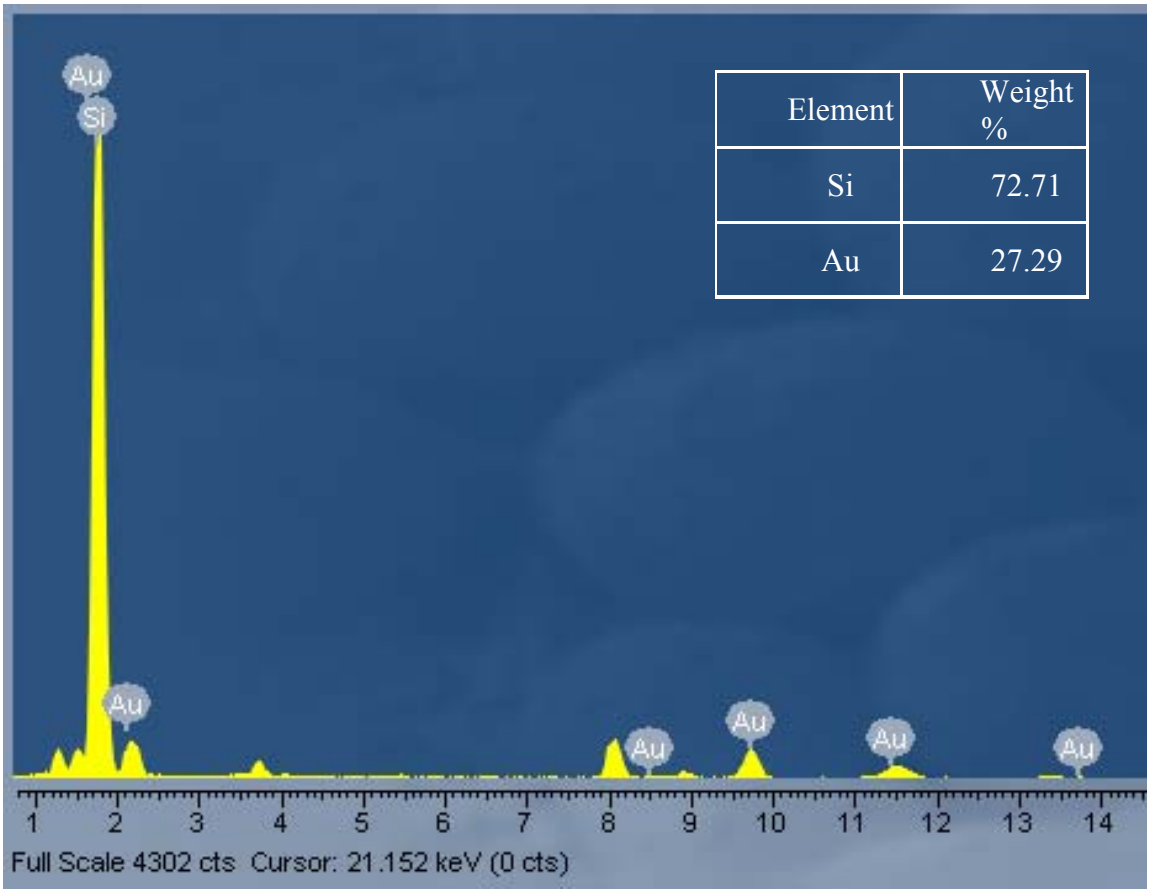

Element	Weight %
Si	72.71
Au	27.29

Figure 5.2. EDS data showing the composition of the nanostructure. It has 72.71%wt. of Si and 27.29%wt. of Au.

A TEM image of the cross-section of the nanostructure is shown in Figure 5.3. The boundary between the nanostructure and the Si substrate is not distinctly clear. The highly localized down-force and frictional energy activates gold atoms to diffuse into the Si substrate forming an alloy. The mixed layer of Au-Si under the substrate is only a few atomic layers thick. With further sliding of the probe on the substrate, the nanostructure was grown on the substrate. The left-inset is one of the cross-sectional images, and the right is the diffraction pattern of the structure.

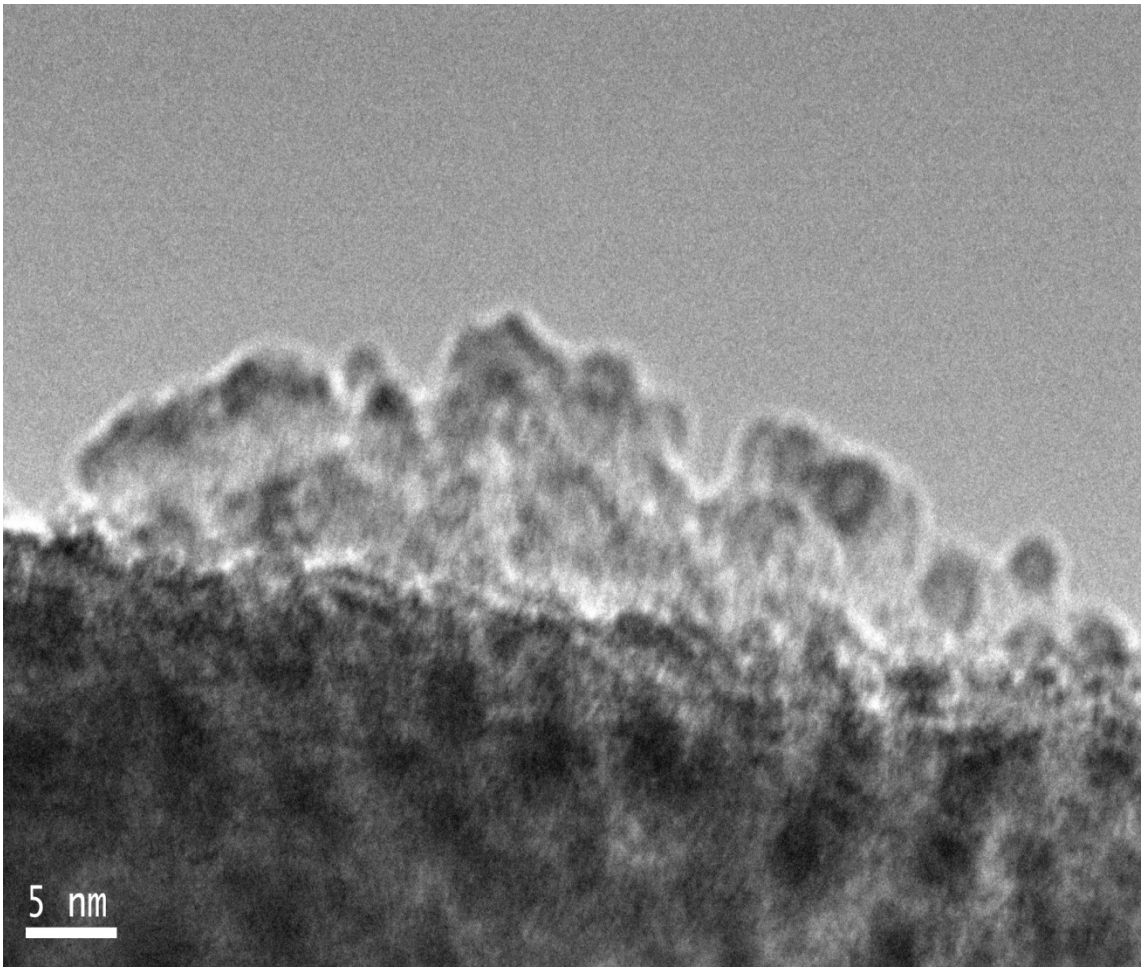

Figure 5.3. TEM images of the interface of the nanostructure and the silicon substrate.

5.2. Electrical Conductivity of Small Structures

The nanostructure in Figure 4.8 was characterized for its conductivity. Results are shown in Figures 4.13 and 4.14. As mentioned earlier, the electrical current through the nanostructure did not respond linearly with the input voltage. That means that at low electrical potentials (from -0.3 to 0.3V), the nanostructure has a low resistance (R_{low}, high current), and a high resistance (R_{high}) at high potentials. The resistance is 5 and 14.3kΩ for low and high potentials, respectively.

Much like strain gages and thermocouples vary resistance in response to a mechanical deformation and thermal variations [34, 35, 36], the nanopatterns on Si respond to an applied electrical potential. The resistance (R) of the material depends on the length (L), cross-sectional area (A), and the resistivity (ρ) as shown in the following equation.

$$R=\rho L/A \quad \text{----------} \qquad \text{(Equ.7)}$$

Here the length (L) and the cross-sectional area (A) of the nanostructures were maintained to be constant. The resistivity (ρ) could thus dominate the resistance. According to Ohm's Law, it has been known that the current should increase with the voltage. The charge passing through the nanostructure is hence increased with the increased electrical potential. It means that more electrons past through the nanostructure. Meanwhile, the traveling electrons generate heat. The generated heat is proportional to the square of the current (Joule's Law). Heat induces resistance and resistivity of the nanostructures increased with the following relationship.

$$\rho=\rho_0[1+\alpha(T-T_0)] \quad \text{----------} \qquad \text{(Equ.8)}$$

where ρ_0 is the initial resistivity, α is temperature coefficient of resistance, T and T_0 are the changed and initial temperature. Finally, as the electrical potential increases, the resistance is increased.

5.3. Interface

Our experiments have shown that the contact-sliding with an AFM can generate well defined microstructures. The friction force did not damage the line during sweeping. Instead, we observed that friction firstly continued the dots of debris/asperities (Figure

4.6a), then the line (Figure 4.6d), and finally completed it (Figure 4.7). The interface of Au and Si is strong enough to sustain sliding impact in later steps. Our results have shown that the thickness and width of the line range from a few atomic layers to a few microns. There are two potential explanations in the formation of the Au-Si interface: abrupt interface [157, 158], and an intermixed layer [159, 160]. Our results indicated that diffusion is likely to be a major factor since the line is found stable after forming. The frictional heating promoted the formation of the line. The formation of a stoichiometric compound is likely to bond the line onto the Si substrate. If a stoichiometric compound is formed, then the interface layer should be at least a few (tens of) atomic layers. If there is no such compound formed, the Au and Si will be bonded through Van der Waals forces. As shown in a TEM cross sectional image of a nanostructure (Figure 5.3), there are several layers. Each layer is randomly composed of the both materials of Au and Si. Those layers stacked up to at least 10nm in height. It is believed that the interface of the Au-Si system follows the intermixed-layer theory rather than the abrupt interface theory. This means that the gold atoms diffuse into the Si substrate so that they are mixed together under 2 atomic layers from the Si surface. When the mixed layers form at least 2 monolayers, the nanostructures start to grow on the surface by diffusion of Au and Si atoms, so called inter-diffusing. The atomic structure is the randomly mixed formation.

Thermal dynamically, the Au-Si follows the equilibrium phase diagram (Figure 3.4). Our results showed that the concentration of Au and Si are 27.29% and 72.71% as shown in the EDX results in Figure 5.2. at room temperature. Within a small length scale, a certain amount of Au is needed to relax the interfacial energy through surface interactions. The intermixed interfacial region between Au and Si materials reduces the interfacial free

energy to be stable. This is further proven by our nanoscale characterization in electrical conductivity. The microstructure apparently has much higher conductivity than that of silicon.

Our results demonstrated that the nucleation of the Au-Si interface as well as further crystallization forming the line were thermodynamically possible. Figure 5.3 shows particle-like features at the interfacial regions. This might be the nuclei. The diameter of such nuclei is around 2nm. The inside center is a graynish colored, but the outer is darker. It means that Au is a hypothetical nucleus for nucleation. If the gold nucleus is too small as a nucleus, the interfacial free energy would not be enough to induce nucleation. It's known that the critical nucleus radius (r^*) is following Equ.9.

$$r^* = -2\sigma/\Delta G_v \quad \text{----------} \quad \text{(Equ.9)}$$

where σ is surface tension and ΔG_v is the change per unit volume of the interfacial free energy. According to the equation, a nucleus bigger than a certain critical radius is needed to initiate nucleation. The critical radius depends on the surface tension and interfacial energy to be released. However, in the case of the contact-sliding, the frictional energy and the heated surface provide the interfacial energy, even though the gold nucleus is small (r=0.5nm). Hence, the equation (Equ.9) could be modified with the friction energy (G_F) and heating energy (G_T) as shown in Equs.10 and 11

$$r^* = -2\sigma/(\Delta G'_v) \quad \text{----------} \quad \text{(Equ.10)}$$

$$\Delta G'_v = \Delta G_v + \Delta G_F + \Delta G_T \quad \text{----------} \quad \text{(Equ.11)}$$

Based on our results, we come to the conclusion that the nucleation and growth were most likely associated with the interfacial free energy through sliding friction stimulation. The interfacial free energy is released by forming stable nuclei, and eventually thermal

activation provides enough energy for intermixed-layers to be grown on Si surface. During the process, the both materials of Si and Au are inter-diffusing. Finally, the nanostructures are a randomly intermixed, a low-packing, and a non-equilibrium system.

6. APPLICATIONS*

In the research, the SPAN process was successfully demonstrated to fabricate nanostructures. The nanostructures fabricated by the process are applicable to be used in a biosensor and a flexible device. In this section, the feasibility of the nanostructures to be used in those applications is demonstrated. Sections 6.1 and 6.2 discuss about the applications as a biosensor and a flexible device, respectively.

6.1. Biosensor

The nanowires can be used as biosensors. One of the advantages of nanowire biosensors is that single-molecule can be detected due to their sensitivity and selectivity [120]. The applications of nanowires in biological areas are sought after in the present research. If the nanowires are fabricated on a piezoelectric material, the nanowires could be operated with the electrical power supply of the piezoelectric material. The piezoelectric material could be used as a sensor. Piezoelectric materials have been used as smart sensors [161]. To show the possibility of the SPAN application on a biosensor, the nanowires will be fabricated on a piezoelectric material, and then the piezoelectric material will be attached to cockroaches to detect their movement and generate an electrical potential. Piezoelectric materials have been used as smart sensors [162, 163].

---

*Reprinted with permissions from "Polymer Sensors to Monitor Cockroach Locomotion" by Hyungoo Lee, 2007, IEEE-Sensors, vol. 7, pp.1698-1702, Copyright 2009 by IEEE Intellectual Property Rights Office, and from "Nano-scale characterization of a piezoelectric polymer (polyvinylidene difluoride, PVDF)" by Hyungoo Lee, 2008, Sensors, vol. 8, pp. 7359-7368, Copyright 2009 by Creative Commons Attribution License.

Polyvinylidene fluoride [PVDF, $(CH_2 - CF_2)_n$] has been widely used for research and in industrial applications [164-167]. PVDF is known for its durability, biocompatibility, and flexibility [167]. It is sensitive and can generate measurable voltages when subjected to a small mechanical force [168-173]. For this reason, PVDF has been used in various sensors, such as transducers, pressure sensors, acoustic components, and airborne sensors [164] .In this work, we developed a PVDF-based sensor and attached it to the limbs of cockroaches in order to monitor the movement of roaches. We work with a Discoid or False Dead-head roach, *Blaberus discoidalis,* a large-sized neotropical cockroach. The species are commonly distributed from Mexico to South America and is easily reared under laboratory conditions. Typically, roaches are found almost everywhere there is food and moisture [174, 175]. Using our approach, we found that the output voltage was a function of the degree of sensor bending caused by the movement of leg sclerites.

A PVDF thin sheet (from Measurement Specialties Inc.) was used to fabricate the sensors for our experiments. The PVDF sheet has a thickness of 52μm. A gold layer was deposited on both sides of the PVDF sheet using a hummer sputtering system (Anatech Corp.). The sputtering rate was set at 3mA for 10 minutes. The final thickness of the gold layer was 100nm (Figure 6.1a) for each side. After coating, the gold-coated PVDF was cut into the size as shown in Figure 6.1b. The sensor had a base of 2×3mm. Thin wires (ANACONDA WIRE) of 0.3mm diameter were attached to both sides of the sensor using epoxy. Under the influence of bending, an electrical voltage is generated due to the piezoelectricity associated with PVDF. To measure and record the output voltage, the wires were connected to a real-time oscilloscope (Tektronix THS720P).

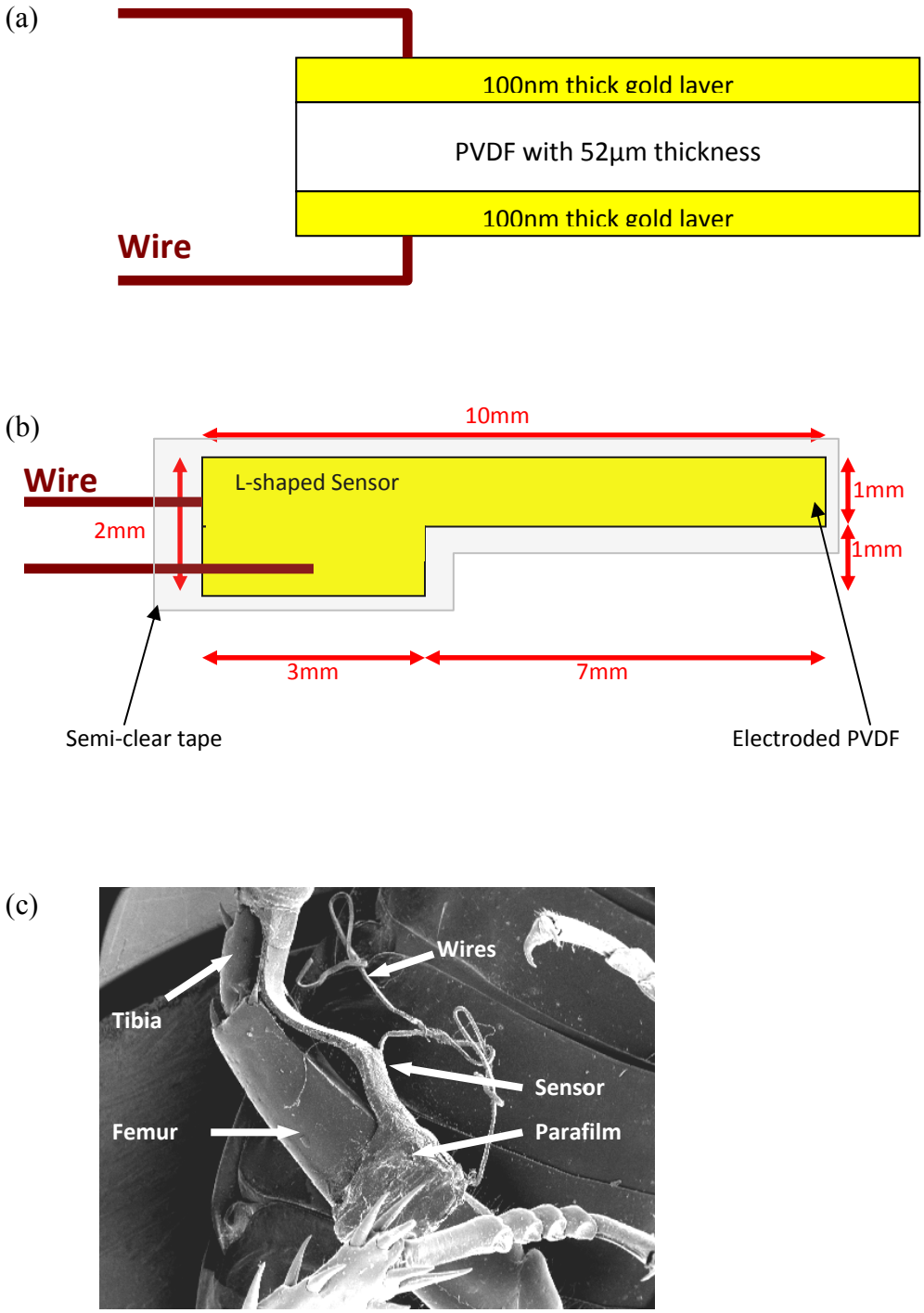

Figure 6.1. (a) Cross-sectional view for the gold-coated PVDF (b) L-shaped sensor used in the tests (c) Attachment location at the 'femur- tibia' joint is shown. The sensor was always placed on the inside area of the joint causing bending.

Sensors were attached to either male or female *Blaberus discoidalis* roaches that were about 50mm in length. The insects were firstly narcotized with CO_2. To attach the sensor, a commercial parafilm (PECHINEY 'M' Laboratory Film) was cut into 30 × 1 mm^2 strips. The strips were wrapped around the insect leg with the sensor placed on the inner surface of the leg (Figure 6.1c). Sensors were attached to the leg segment at the joint between the coxa and femur (CF), or femur and tibiae (FT). The sensors were placed on the inner surface of the joint as shown in Figure 6.1c. The metathoracic legs were studied instead of the prothoracic or mesothoracic legs, due to the greater degree of bending of the joints of these legs.

A live roach is hung from a cork that is fixed to a stand. The roach's legs can move freely in this configuration. The roach grabs a foam ball (6.16g in weight) with its hanging legs (Figure 6.2). This setup is less complex than treadmills that have been reportedly used to study roach walking [176, 177]. The roach can move freely in any direction it may choose. Discoid roaches can drag 7.6 times (28.12g) their weight (3.7g) [178, 179] and can efficiently lift up to two times (7.4g) their body weight [178]. Two types of tests were performed. One was a "pulling test" where the foam ball was pulled away from the roach causing full leg extension. The second test was to make the roaches walk and run.

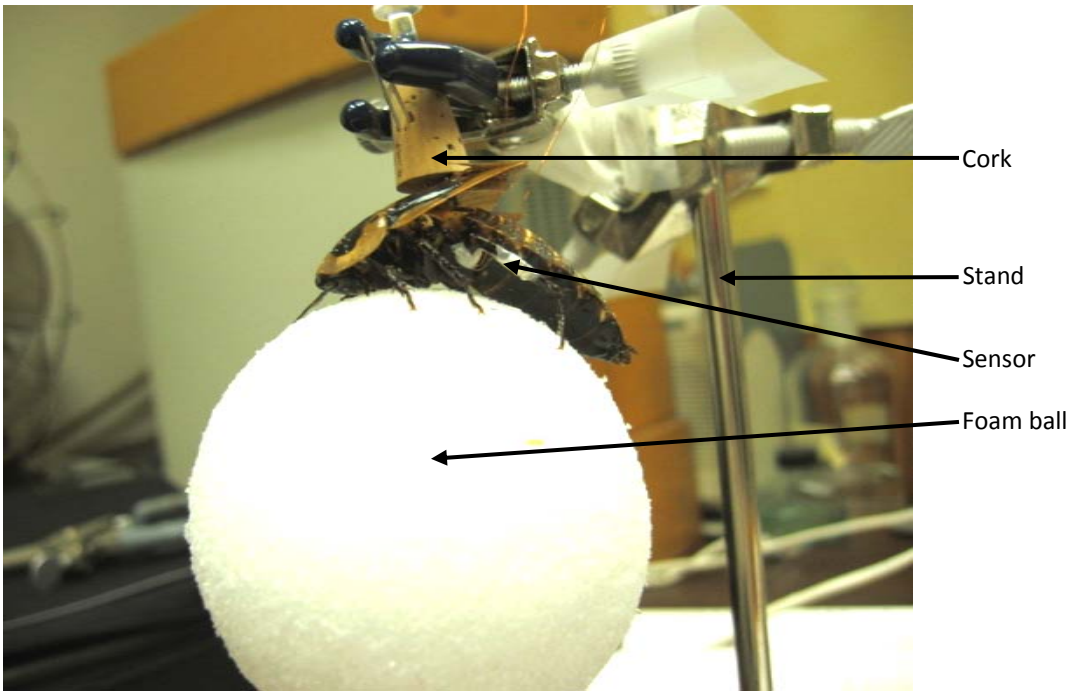

Figure 6.2. Experimental setup for roach (*Blaberus discoidalis*) tests. The roaches are suspended as they grasp and hold a foam ball. Sensor is already attached to the leg of the roach.

In pulling tests, the ball was pulled away from the roach making their legs stretch, along with the sensor. The legs flexed back when the ball was pulled beyond reach. In the walking/running tests, the ball rotated as the roach moved, and the sensor bent along with the leg. The degree of flexing in this case was less than in the pulling test. In addition, during walking/running, the sensor bent multi-directionally. The charge of the sensor was believed to be due the dipole alignment [180-183], and was sensed by the oscilloscope, which read out the resulting voltage.

Figure 6.3 shows a sample output signal recorded by the oscilloscope in real time during one of the pulling tests. The y-axis and the x-axis represent voltage of the output signal and time, respectively. Each segment along the y-axis represents 100mV, while

each horizontal segment corresponds to 1 second. In the Figure 6.3, the output signal is about 400mV. There were 26 sensors tested. Each test was repeated 20~50 times. The output signals varied from 20mV to 1000mV. During the pulling tests, the stretched legs straightened the sensor and then released it to the nominal position again.

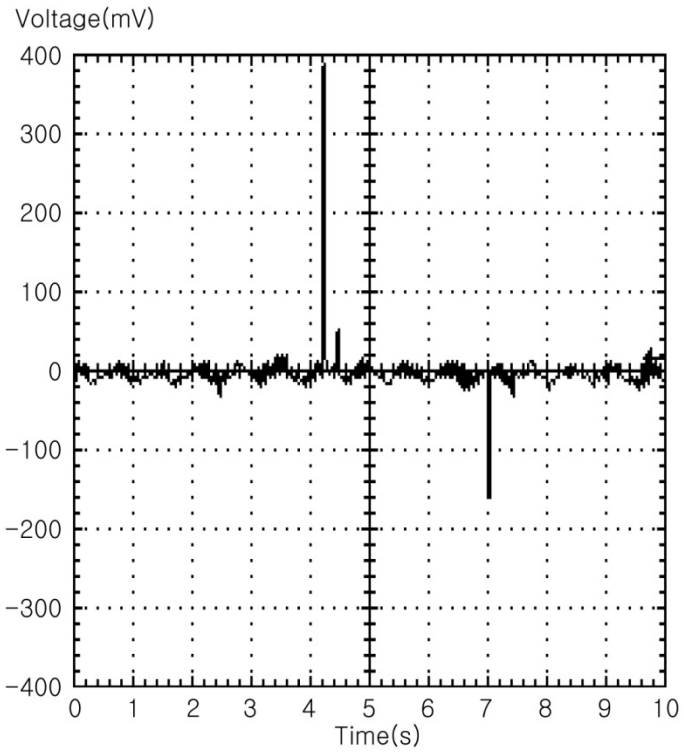

Figure 6.3. Pulling data image; the output signal is 400mV. Each vertical segment represents a voltage of 100mV, and each horizontal segment represents 1 second.

Our setup enabled the tethered roach to walk on the foam ball. Figure 6.4 shows the output signal from one of the walking tests, as recorded by the oscilloscope. In the figure, the x and y-axes correspond to time and voltage, respectively. The scales for x and y-axes of the figure were the same as for Figure 6.3. The output signal in Figure 6.4 is 200mV.

The same sensor was used for both pulling and walking tests. Even though pulling data is considered artificial, the walking data is considered natural since no additional external forces were applied to the foam ball. The walking results indicate that roaches could force the sensor to bend and to produce measurable voltage signals.

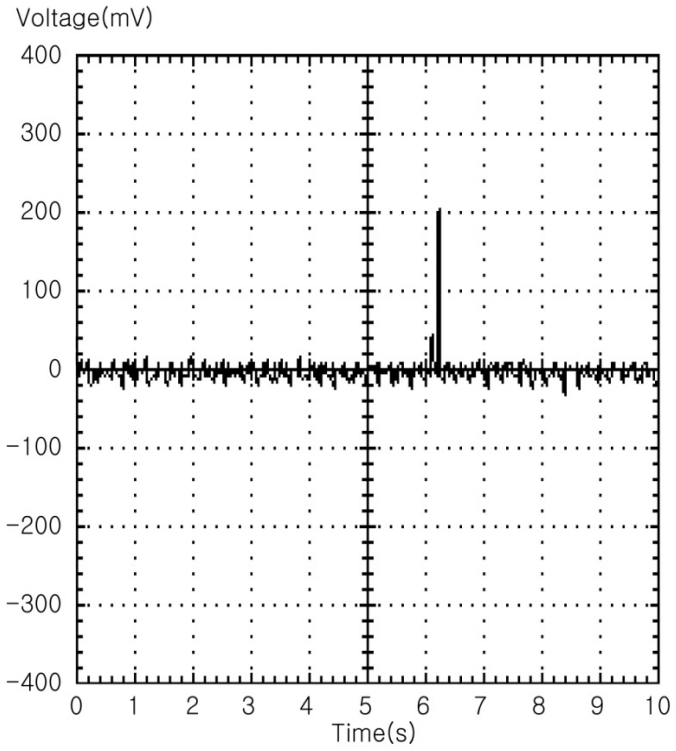

Figure 6.4. Walking data image; the output voltage is 200mV. Each vertical segment represents a voltage of 100mV, and each horizontal segment represents 1 second.

As noted in the experiments section, each sensor was placed across one of two locations: coxa - femur (CF) and femur - tibia' (FT). We are interested in determining if the attachment locations would affect the output signal. Indeed, the sensors attached on the CF generated a larger output signal than the FT attachment. One of the reasons was

due to the different bending angle of the CF and FT configurations. More details will be discussed in the following sections.

The generated signals from the sensors was conjectured to depend on the bending speed, angle, pressure, and force applied to the sensors [184, 185]. In the present work, the roaches bent and stretched their legs usually twice per second. As a result, there were two peaks per second on average (2Hz). When the roaches moved at a frequency faster than 2Hz, the output signal frequency was increased as a function of the roach's rate of flexing its legs, as shown in Figure 6.5(a). At a low rate of leg flexion, i.e. less than 2Hz, as shown in Figure 6.5(b), the number of the peaks are found to decrease. It was observed that the amplitude of the peaks was not related to the frequency.

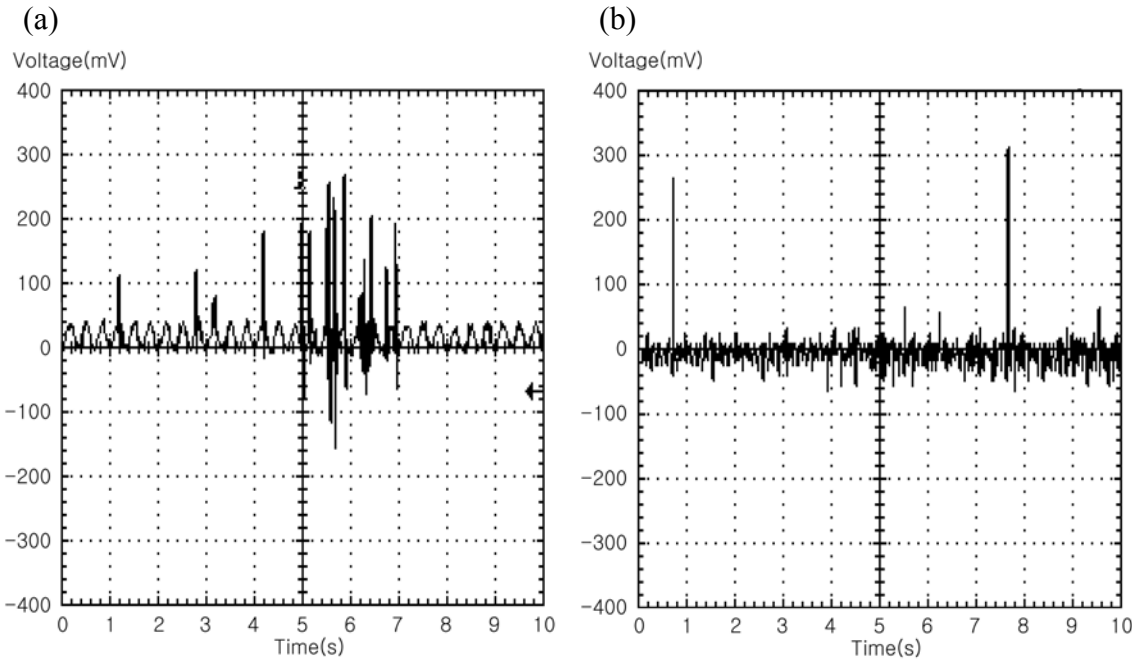

Figure 6.5. Voltage output generated by sensors attached to a roach's leg (FT joint) (a) running (b) walking.

The number of peaks is proportional to the bending frequency, but the voltage magnitude is largely independent of bending frequency. This proves that the Au-coated PVDF sensors can detect the speed of the roach movement; the higher the speed of the roach movement, the more frequent the generated voltage pulses.

The sensors attached to the CF joint generate higher amplitude signals than the ones attached to the FT joint. There are two possible explanations for this. One is due to the fact that the angle of CF movement was greater than that of FT; the other is due to the induced mechanical force of the CF joint. It was found that the CF joint angle ranges from 0º to 180º, and the angle of the FT ranges from 90º to 180º, when roaches move. Thus, the output signals from the CF configuration were higher than that from the FT configuration.

These results are believed to be due to the higher angle of the CF movement. In other words, the large magnitude of the voltage obtained in the CF configuration is due to the flexing of the joint over a large angle, but with the same speed, compared to the FT configuration. This shows that the sensors voltage amplitude is proportional to the angle of the joint flexion. The results were further supported by an experimental setup using a motorized linear stage. The motorized linear stage was designed to mimic the bending motion of the sensors attached on the roaches' legs with better repeatability. This system allowed us to control the angle (Figure 6.6a) and frequency (Figure 6.6b) of the bending sensors. As shown in Figure 6.6a, the amplitude of the output voltage was proportional to the bending angle (for a constant bending frequency). However, the amplitude of output voltage was largely independent of the bending frequency (for a constant bending angle).

(a)

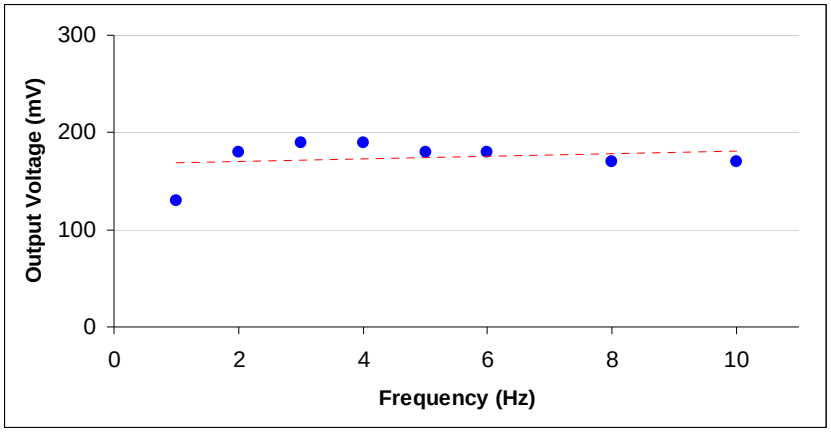

(b)

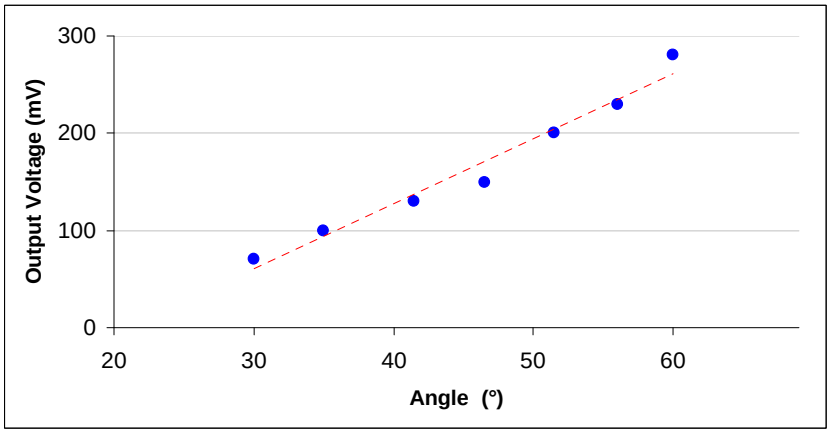

Figure 6.6. The linear motorized system mimics the bending motion of the roaches' legs. The amplitude of the output voltage was affected by bending angle (b), not by frequency (a). For bending tests (b), the frequency was fixed at 1Hz. The frequency tests (a) were conducted with a maximum bending angle of 97°.

In the present study, the sensors tested for CF attachment were also used for the FT attachment. The environmental temperature for all tests was kept at room temperature (25±2 °C). The reason for keeping the temperature constant is that PVDF has pyroelectric

properties, which results in a change in the induced-output voltage with changing temperature [171, 186]. Under these conditions, the CF results could be directly compared to FT results. Figure 6.7 shows that the output voltages induced by the pulling tests are higher than for the walking tests (for both the CF and FT configurations). The voltages induced during pulling or walking are both significantly higher than when there is no movement at all. During the pulling tests, the roach legs were highly stretched, and after releasing the foam ball, the leg joints were folded at high speed. Under such high angles of bending, the output voltages from the pulling tests are seen to be higher than those for the walking test (Figure 6.7).

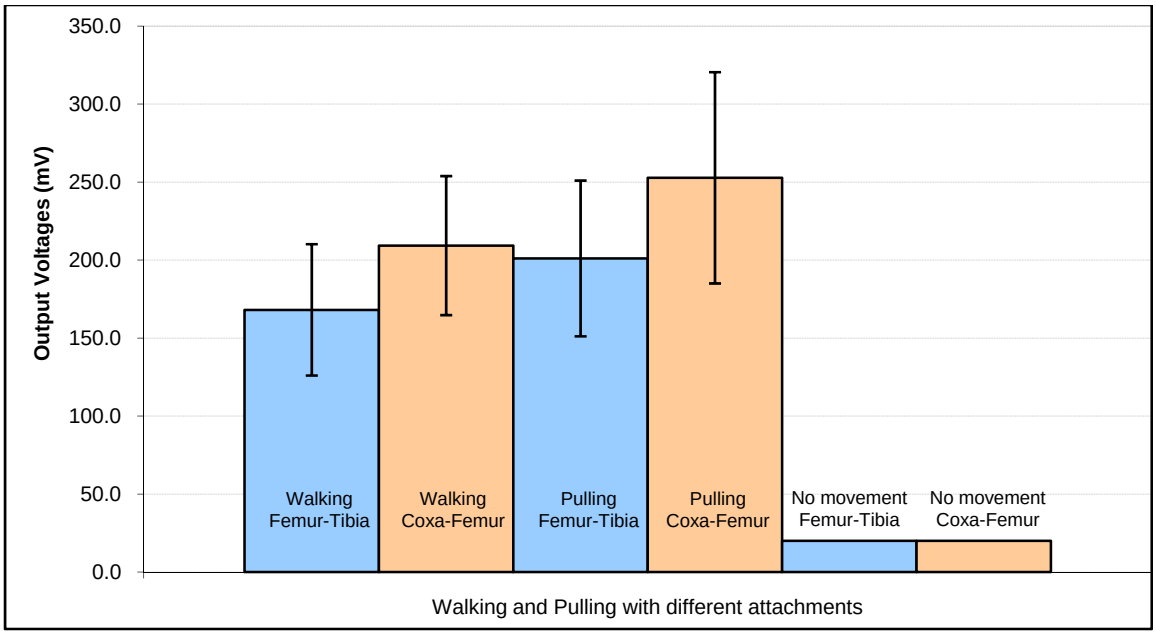

Figure 6.7. The output voltages of the experimental sensors under six conditions: Walking, Pulling and No movements, for two roach leg joints FT and CF using Discoid Roaches (*Blaberus discoidalis*).

The higher the bending angle, the higher the output voltage. Moreover, the voltages induced during the CF test are higher values than those induced during the FT tests. Since the coxa is the stronger leg segment, it is responsible for the initial "pushing" which leads to locomotion [187]. The CF joint folded with higher angle than the FT joint, in the same time interval, hence yielding larger output voltages.

The development of a technique to use polymeric sensors to monitor a roach's leg motion is presented here. With appropriate attachment locations, sensors were proven to be able to produce a measurable output voltage in tandem with the cockroach's movement. Results from pulling experiments indicated that the gold-coated PVDF works as a functional sensor that monitors the roach's leg movement. The signal data taken from roach walking on a foam ball proved that the legs of the roaches could bend the electrode coated PVDF sensors and repeatedly produce measurable output voltages. Comparing the two joints studied, it was found that the amplitude of the generated voltages from the sensors placed on the CF joint was higher than those placed on the FT joint due to the larger bending angle of the CF joint. In addition, the higher the speed of the roach, the more the frequency of the generated voltage pulses. This result was consistent with tests done with a motorized linear system. Our results further show that the amplitude of output signal was dominated by the bending angle. The output frequency depends on the bending frequency. Therefore, it can be concluded that PVDF based sensors can be used to measure the speed of roach movement, by means of the induced-voltage pulses from the PVDF sensor. Monitoring a roach's movement could bring insights into the behavior of insects and environments. In the long run, such a study could lead to mimicking the physiological behavior of natural biological systems.

6.2. Flexible Device

As mentioned above, piezoelectric materials have been wildly used for research and in industrial applications [188, 189]. Once the materials are physically stressed, they generate electrical potentials. Among those, there are flexible materials such as polyvinylidene fluoride [PVDF, $(CH_2 - CF_2)_n$]. If the nanowires are fabricated on these flexible piezoelectric materials, it will show the possibility that the flexible devices can be fabricated.

For Micro-electro-mechanical systems (MEMS) and Nano-electro-mechanical systems (NEMS), the piezoelectric materials play an important role [190, 191]. Polyvinylidene difluoride (PVDF) has been widely used in engineering applications due to its favorable chemical and mechanical properties [164-166, 192, 193]. The properties such as high piezoelectric coefficient, good flexibility, biocompatibility [194-196], low acoustic and mechanical impedance, and light, are especially unique for MEMS applications. The PVDF is one of the most widely used piezoelectric materials in the fluoropolymer family. Its piezoelectricity was discovered in 1969 [170]. However, the mechanism of piezoelectricity has not been clearly explained [197-199]. Its uncertainty obstructs the development of MEMS or NEMS. Many researchers have attempted to explain the origin of the piezoelectricity of the polymer [173, 200-203] and to investigate the structure change of PVDF due to electric field [203] and temperature [204].

Recently, development in new characterization techniques, particularly nanoscale analysis, has made it possible to bring new insights from the piezoelectricity measurements. One of the techniques is the Atomic Force Microscopy (AFM). It enables to characterize surface morphology at nano-scale. Using an AFM, we investigate the

relationship between the piezoelectric properties and structures of PVDF. An electrical field was applied to the PVDF samples. The effects of the external electrical voltage on the sample surface was observed using AFM. The responding time of the PVDF samples to mechanical stress was studied.

This study was performed using three different samples of polyvinylidene difluoride (PVDF). The original PVDF film samples were stretched to obtain the polar β-phase. The samples were examined for polarity (β-phase, TTT type) and piezoelectric coefficient (23pC/N). Using a metal evaporator, the metal coatings were deposited on the films as electrodes. Two samples of 110μm and one of 52μm of film thickness were coated with 28μm of Ag, 600 Å of NiCu, and 150nm of Au, respectively. The size of all samples was 3cm in length and 1cm width.

A home-built splitter, i.e., a Shark box, was attached to an atomic force microscope (AFM). The splitter distributes electrical potentials and passes a current from samples to a picoameter. The splitter was powered through the AFM's built-in power supply as shown in Figure 6.8. The sample surface is scanned with a standard Si_3N_4 probe. The surface profile is measured against the electrical potential. When bent, a PVDF sample generates a micro-ampere current flowing to a computer through a picoameter. The computer records the output current with LabView program. In this case, conductive AFM probes were used.

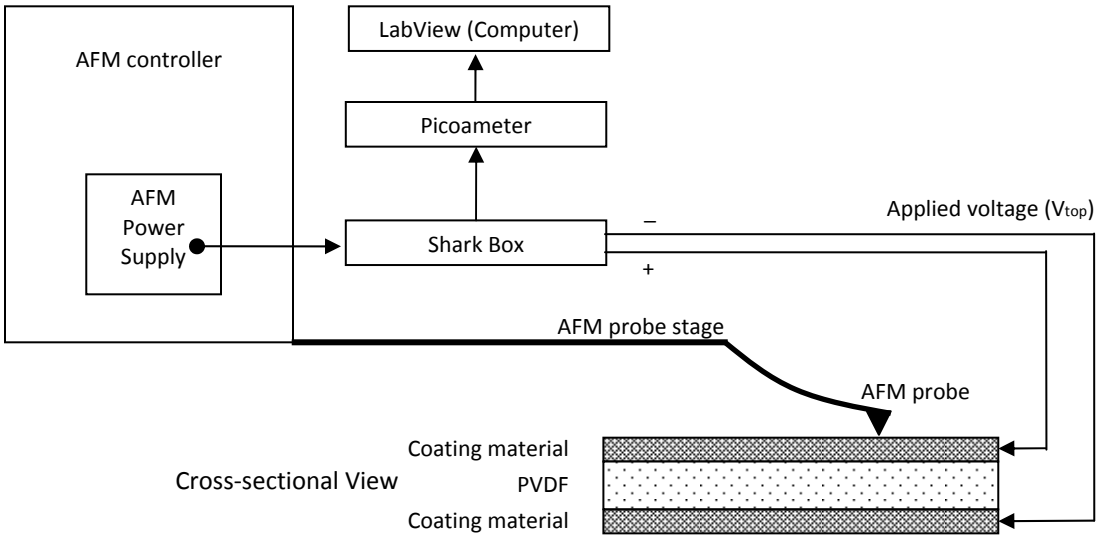

Figure 6.8. Diagram for the experimental setup and characterization. This work was done with an AFM Si3N4 probes. The external electrical potentials were supplied to the PVDF samples throughout the shark box which is a splitter for electrical potentials and current.

A motorized linear stage (MLS) was used to characterize the responding time of the dipoles in PVDF. The coated PVDF samples were placed on the MLS from end to end as shown in Figure 6.9a and b. With one of the sample holders fixed in a stationary position, the other holder moved reciprocally at a frequency of 4Hz in a stroke length of 3cm. This reciprocal motion buckled the PVDF samples. The buckling induces internal mechanical stresses. Figure 6.9c shows the AFM setup applying a force on one end. As a result, the PVDF sample produced an electrical potential due to the piezoelectric property. The voltage generated was recorded using the LabView throughout a picoameter.

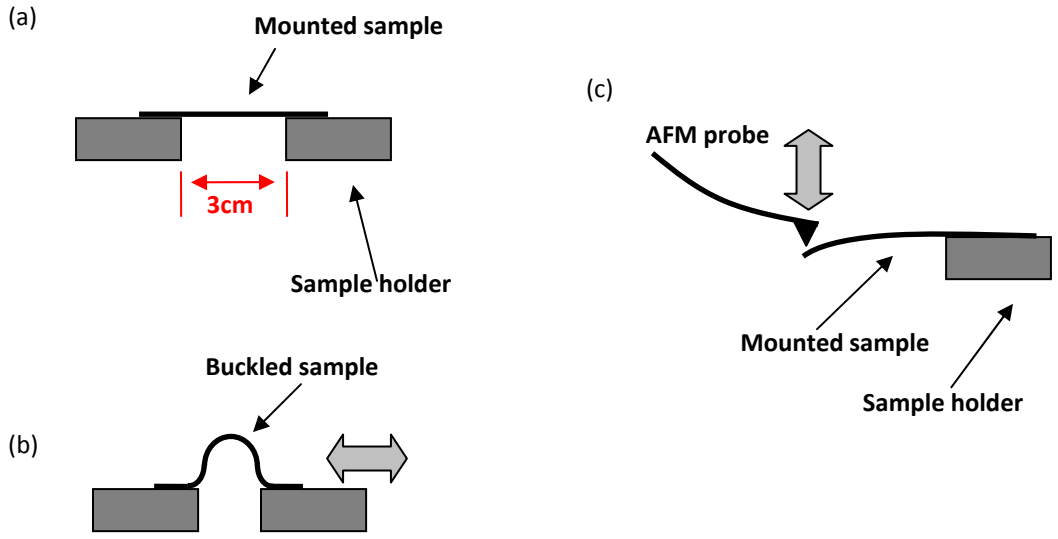

Figure 6.9. Simple diagrams of Motorized Linear Stage (MLS) (a, and b) and AFM setup (c) to apply mechanical stresses on a sample.

Scans of a PVDF sample, with the thickness of 110μm and an Ag-coating of 28μm, were conducted using the AFM with a standard Si_3N_4 probe. Figure 6.10(a) shows a scanned image of the sample prior to connecting the Shark box. The same region of the sample was scanned with the leads of the shark box connected to the PVDF as shown in Figure 6.8 while an applied electrical potential was at 0V.

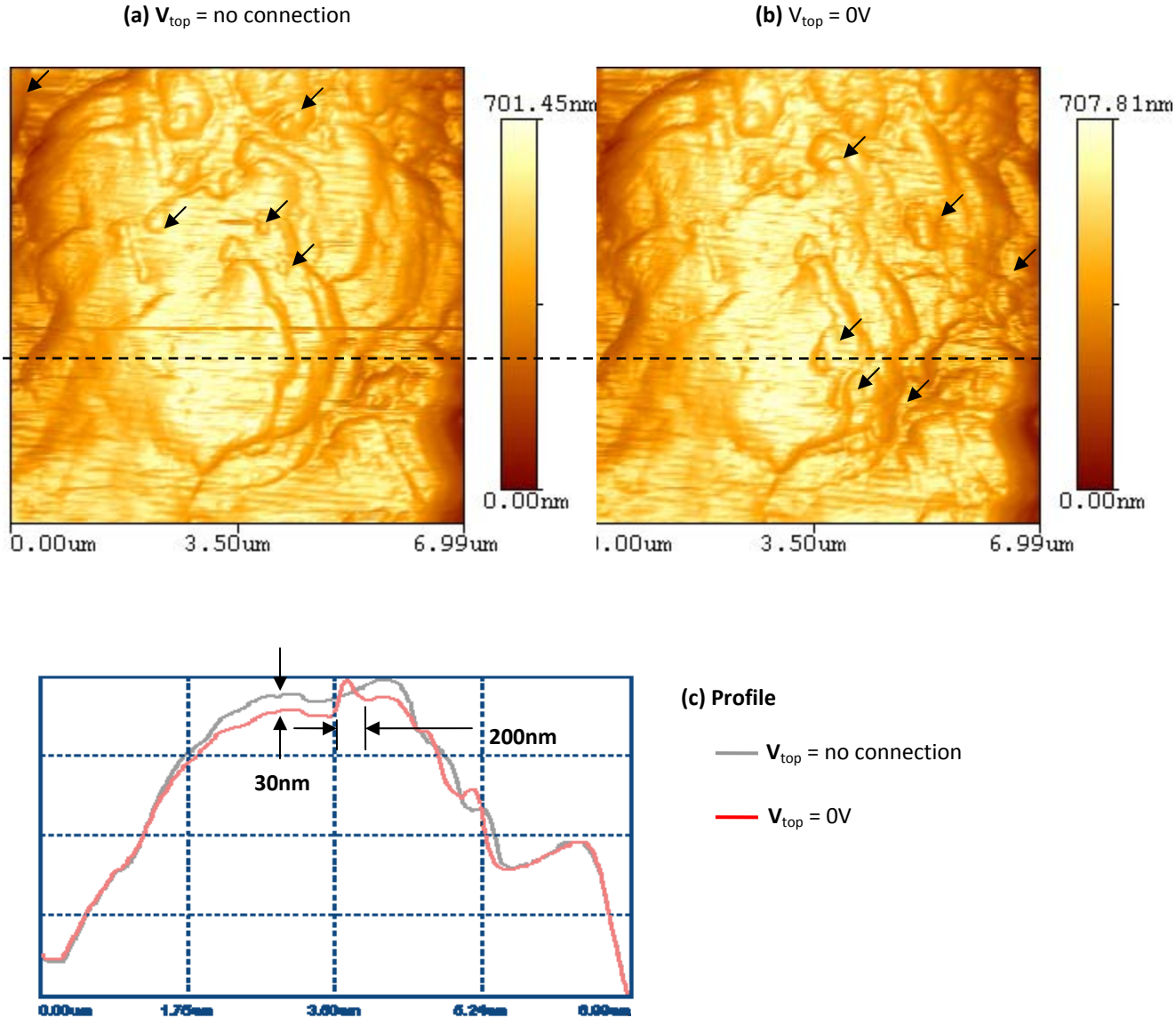

Figure 6.10. AFM images for the PVDF sample surface which was 110µm thick with 28µm Ag coated without (a) or with (b) connection of electric field. (c) The profiles of the two scans along the dashed line.

The profiles of the two scans along the dashed line are shown in Figure 6.10(c). It is seen that at the zero potential, the surface profile underwent a morphology change resulting in an increase in roughness.

As the electric potential on the PVDF is increased in discrete steps of 0, 4, 7, and 15V, the roughness (R_a) is seen to increase in a nearly linear manner as shown in Figure 6.11. A similar process was conducted for a PVDF sample of 110μm thickness and 600Å NiCu coat to characterize its surface morphology with external electrical potentials of 0 and 5V. As shown in Figure 6.12, the surface texture was squeezed with the application of 5V. This is believed to be due to the dipole realignment resulting in an increased surface height. A PVDF sample with the 52μm thickness and a 150nm-Au-coating, was used to determine the amount of deformation caused by the applied voltage. This sample showed an original wavy surface when no voltage was applied.

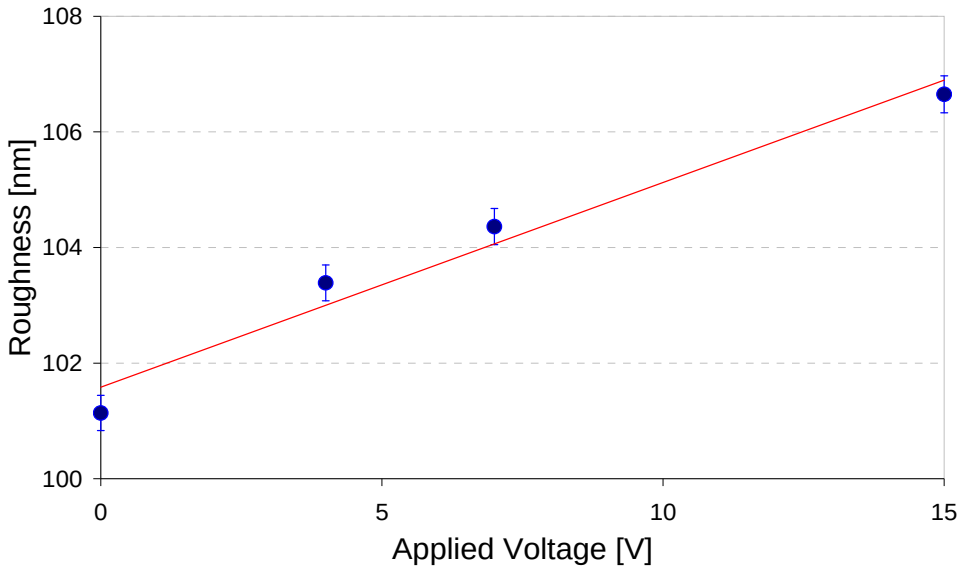

Figure 6.11. Roughness change with the applied voltage.

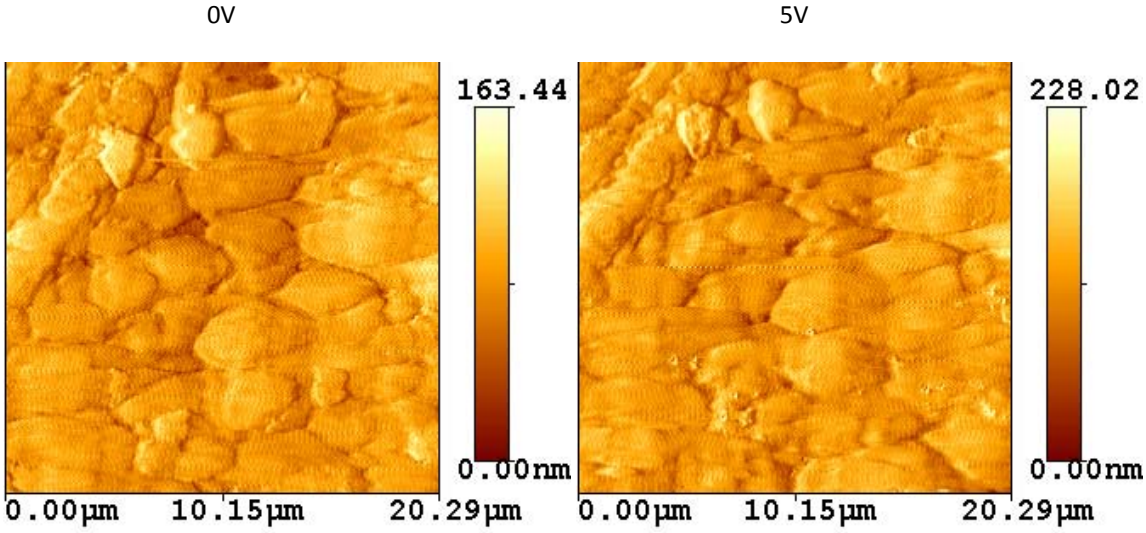

Figure 6.12. The texture change of a PVDF surface. The PVDF sample of 110µm thickness with 600Å NiCu coated was characterized for its surface with external electrical potentials, 0V (a) and 5V (b).

As a voltage was increased, the amount of squeezing deformation was observed and calculated through measuring the peak-to-peak distance (D_{pp}) of the wave surface. Figure 6.13(a) shows AFM images of the sample under different voltages. Figure 6.13(b) displays the change of the D_{pp} due to external electrical potentials. As the applied electrical potential increased, the D_{pp} was decreased with the rate of 28.7nm/V. The slope of the gray line in the figure is equal to the effective piezoelectric coefficient. From the results of MSL test, the response time, t_r, is calculated as the difference between the initial moment when stress is applied, ti, and the time when a voltage signal is produced by the sample, to, such that $tr=t_o-t_i$. It is seen that there is a delay between the blue and dotted line of 0.155s which is equal to the response time (t_r).

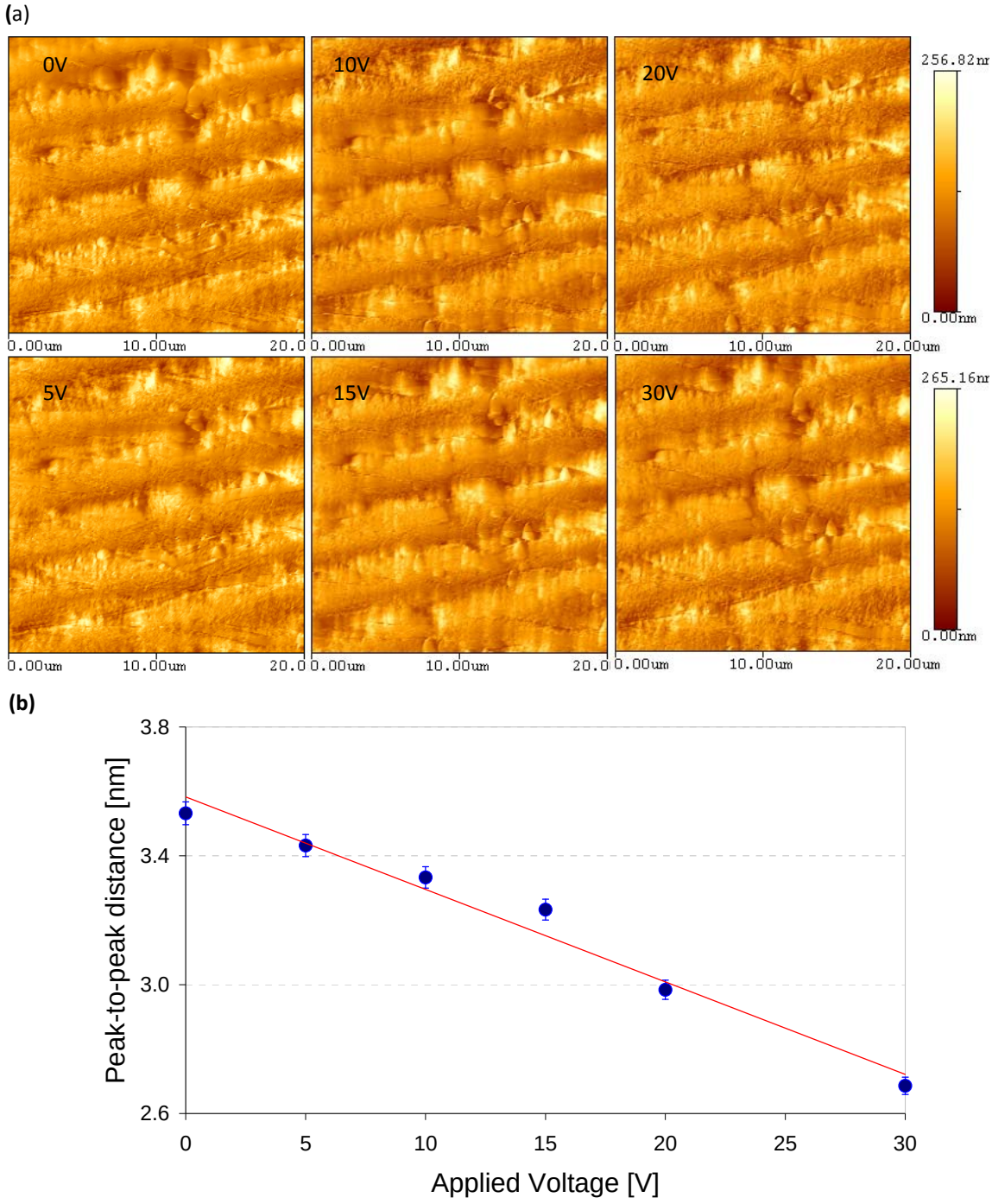

Figure 6.13. Investigation of the surface change rate with the applied voltage. (a) AFM images for a PVDF sample which was 52µm thickness with 150nm Au coated. (b) The change of the peak-to-peak distance (D_{pp}) with the external electrical potentials.

Some polymers have showed transformation on its surface due to external stimuli [205-207]. The surface of an electro-sensitive polymer changed polymer chains and alignment with an applied electrical field [208]. Figures 6.10, 6.12, and 6.13 demonstrate the effect of inverse piezoelectricity due to the alignment of the dipoles in response to an applied electric potential. As a result, the potential caused the change of a surface morphology. Furthermore, the alignment of the dipoles was a temporary response to a voltage and returned to their original state after the voltage was removed. This effect is caused by lamellae (usually 20nm thick) of crystalline embedded within amorphous regions (chain-folded model) of the samples. It was reported that one a 3D polymer was fixed at its ends, the local intra- and inter-chain associated orientational-deformational interactions could induce spontaneous ordering [209]. The lamellae were randomly oriented with no electric potentials present in the sample. As an electric potential was applied, the lamellae realigned to orient their dipole angle and moment to correspondingly. The higher the applied potential, the greater the realignment, and in such, the greater the peak-to-valley distance. The rate of the D_{pp} change was about 1nm per 2V.

In order to understand the piezoelectric behavior at different length scales, we compared the charge output under stresses at nanometer and millimeter scales. The first measurement was conducted by applying external mechanical stress on the samples with the MLS shown in Figure 6.9. As the distance between the sample holders decreases, a mechanical stress is induced into the sample resulting in the alignment of the lamellae which produces a voltage due to the alignment of the dipoles. Figure 6.14a shows the response of such a piezo sensor.

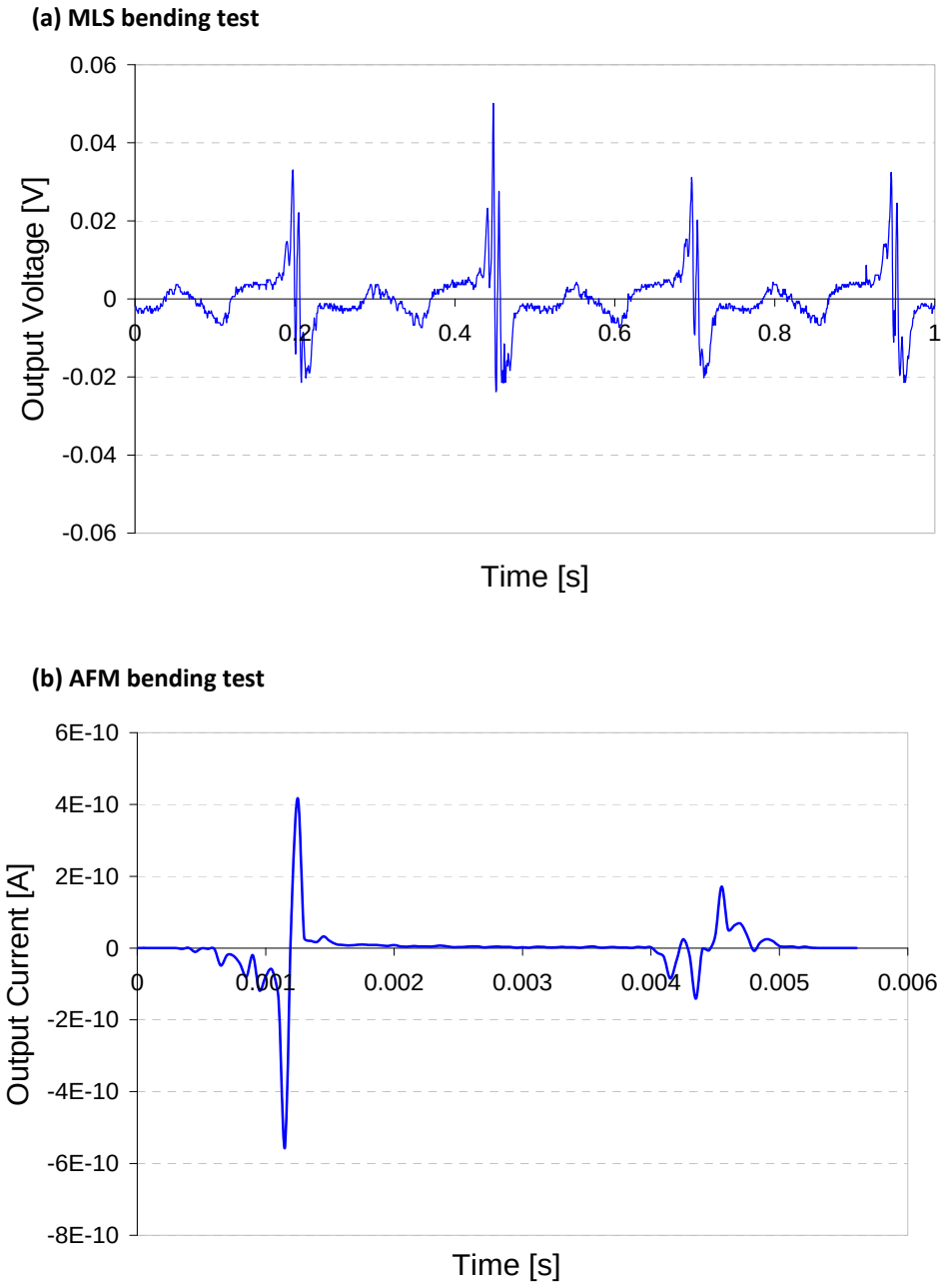

Figure 6.14. The results of (a) Motorized Linear Stage (MLS) and (b) AFM tests showing the output have similar behavior at different scales. The MLS test was to fix two ends of the sensor while the AFM was on a sensor that was fixed at one end only with manual bending.

The voltage produced by the PVDF is proportional to the amount of stress applied to the sample which is proportional to the distance traveled by the MLS holders. Since the sample holder is moving in a reciprocating motion, there should be no movement at its maximum and minimum deflection and not cause any further alignment of the dipoles resulting in a voltage output of 0V. The AFM was used to test the output of a piezo sensor when a down force was applied at one end of the polymer. Although the units of the MLS and AFM were different, the trend of their outputs was the same. This means that the localized dipole alignment is correlated with the global behavior. When an external force was applied, local or global, the PVDF produces a charge and subsequently a morphological change. The effects of electrical potential on microstructures and phase transformation of PVDF have been discussed elsewhere [210]. Since our focus of this research is on the surface morphology study of a piezo sensor, we will not discuss this aspect in details.

Metalized PVDF samples were characterized using an AFM and an external MLS in order to study the mechanisms of piezoelectric effects. Results showed that under an external potential, the surface roughness was increased. Under stress, an output was generated that is scale independent. Such variations are important for design consideration of MEMS devices and their sensitivity.

7. CONCLUSIONS

7.1. Summary

This research demonstrated that by using an atomic force microscope, we were able to generate well-defined micro- and nano- structures that have unique properties. We developed a new method to fabricate nanostructures. The process is called the scanning probe alloying nanolithography (SPAN), using an Au-coated AFM probe to slide against a Si substrate. The increased volume of those structures from the tip wear and their conductivity from the substrate indicate the nucleation and growth of potentially controllable nanostructures. The friction-stimulated structures are different from their original state (Au and Si). As a result, nanostructures (wires, dots, and logos) were fabricated. The properties of the nanopatterns were characterized using high resolution techniques. The line structures had about 10nm in height and 600nm in width. A dot formed by the process was 153nm high and 400nm wide. The electrical properties were also measured using AFM. When the electrical potential 12V was applied, current of 1.07×10^{-3}A was recorded. At low electrical potentials (-0.3~0.3V), the measured resistance R_{low} was 5kΩ. However, the resistance was increased at high potentials (R_{high}=14.3kΩ) due to electrons traveling and heating the material. The conductivity measurement reveals possible interactions between the AFM probe and the substrate material. The mechanisms of SPAN were discussed. The contact-sliding induced friction and thermal energy resulting in the temperature increase. The Au material was transferred from the probe to the Si substrate. Finally, the nanostructures were grown on the substrate.

Assisted by an external potential, the electrical adhesion was involved in the process. The dimension of the nanopatterns could be controlled with the power system. The SPAN technique is expected to be independent from materials and highly controllable. It would generate nanostructures precisely and effectively. Our experiments indicate that minimizing nanostructures is possible using a sharp AFM probe. With a sharpened tip and lower down-forces of a tip on a substrate, the lines can be further downsized.

7.2. Research Impacts

The SPAN will open a new avenue to fabricate nanowires and help to extend the Moore's prediction which cannot be achieved by the conventional photolithography. To improve the efficiency of SPAN, this research optimizes the process by understanding the scientific phenomena of material transformation, phase change, and nanostructure formation. This will also explain the fundamental principles involved in this process, such as nano-friction and nano-wear behaviors between the AFM probes and the substrates. In addition, this study will show the possibility of using the nanowires in biosensors and flexible devices.

7.3. Future Recommendations

There are some future recommendations to improve the research. During experiments, the down-forces of the probes against the sample surfaces couldn't be measured in real-time. Up to now, the forces were only calculated. To obtain more accurate data and precise control the probe, the real-time measurement for the probe down-forces is recommended.

Probes with different spring constant and sharpness are recommended to be used for the SPAN process. This will bring further understanding of the interfacial mechanisms and further optimization of the SPAN. It will also provide more opportunities for new applications.

REFERENCES

[1] Y. Watanabe, A. Seko, H. Kondo, A. Sakai, S. Zaima, and Y. Yasuda, "Conductive atomic force microscopy analysis for local electrical characteristics in stressed SiO_2 gate films," Japanese Journal of Applied Physics, Part 1, vol. 43, pp. 1843-1847, 2004.

[2] D. Banks, "General introduction to micromachining," IEE Seminar Digests, vol. 1, pp. 1-6, 1997.

[3] O. J. F. Martin, N. B. Piller, H. Schmid, H. Biebuyck, and B. Michel, "Energy flow in light-coupling masks for lensless optical lithography," Optics Express, vol. 3, pp. 280-285, 1998.

[4] H. Schmid, H. Biebuyck, B. Michel, and O. J. F. Martin, "Light-coupling masks for lensless, sub-wavelength optical lithography," Applied Physics Letters, vol. 72, pp. 2379-2381, 1998.

[5] H. Schmid, H. Biebuyck, B. Michel, O. J. F. Martin, and N. P. Piller, "Light-coupling masks: An alternative, lensless approach to high-resolution optical contact lithography," The Journal of Vacuum Science and Technology B, vol. 16, pp. 3422-3425, 1998.

[6] K. I. Arshak, N. N. Kundu, and S. N. Gupta, "Simulation of proximity printing," Microelectronic Engineering, vol. 10, pp. 241-246, 1988.

[7] W. Henke, M. Weiss, R. Schwalm, and J. Pelka, "Simulation of proximity printing," Microelectronic Engineering, vol. 10, pp. 127-152, 1990.

[8] B. J. Lin, "A comparison of projection and proximity printings-from UV to X-ray," Microelectronic Engineering, vol. 11, pp. 137-145, 1990.

[9] N. Shiotake and S. Yoshida, "Recent advances of optical step and repeat system," Systems", Proceedings of SPIE, vol. 537, pp. 168-174, 1985.

[10] R. B. McIntosh, Jr., G. P. Hughes, J. L. Kreuzer, and G. R. Conti, Jr., "X-ray step and repeat lithography system for submicron VLSI," Proceedings of SPIE, vol. 773, pp. 156-163, 1986.

[11] A. R. Shimkunas, J. J. LaBrie, P. E. Mauger, and J. J. Yen, "Mask technology of X-ray step-and-repeat system," Proceedings of SPIE, vol. 632, pp. 106-117, 1986.

[12] B. Latombe, M. Alaimo, C. Desplat, F. Debaene, and J. M. Dumant, "Effective procedures to achieve a 1 micron CMOS process using a step and repeat aligner with autocalibration system," Microelectronic Engineering, vol. 3, pp. 267-274, 1985.

[13] H. Binder and M. Lacombat, "Step-and-repeat projection printing for VLSI circuit fabrication," IEEE Transactions on Electron Devices, vol. 26, pp. 698-704, 1979.

[14] P. Gargini, "The International Technology Roadmap for Semiconductors (ITRS): Past, present and future," Gallium Arsenide Integrated Circuit (GaAs IC) Symposium, 22nd Annual, pp. 3-5, 2000.

[15] C. A. Mack, "Pitch: The other resolution limit [photolithography]," Microlithography World, vol. 7, pp. 23-24, 1998.

[16] H. Fukuda, R. Yamanaka, T. Terasawa, K. Hama, T. Tawa, and S. Okazaki, "Characterization of super-resolution photolithography," International Electron Devices Meeting, pp. 49-52, 1992.

[17] A. N. Broers, *Resolution limits of electron beam lithography and methods for avoiding these limits, Nanostructure Physics and Fabrications*, M. A. Reed and W. P. Kirk Eds., Academic Press, London, pp. 421-430, 1989.

[18] C. Vieu, F. Carcenac, A. Pepin, Y. Chen, M. Mejias, A. Lebib, L. Manin-Ferlazzo, L. Couraud, and H. Launois, "Electron beam lithography, resolution limits and applications," Applied Surface Science, vol. 164, pp. 111-117, 2000.

[19] A. N. Broers, "Resolution limits for electron-beam lithography," IBM Journal of Research and Development, vol. 32, pp. 502-513, 1988.

[20] A. N. Broers, "Resolution limits of electron beam lithography," Topical Meeting on Optical Computing, vol. 90, pp. 43-46, 1989.

[21] A. N. Broers, "Resolution, overlay, and field-size for lithography systems," IEEE Transactions on Electron Devices, vol. 28, pp. 2-6, 1980.

[22] A. N. Broers, "Resolution, overlay, and field size for lithography systems," IEEE Transactions on Electron Devices, vol. ED-28, pp. 1268-1278, 1981.

[23] W. Banqiu, A. Kumar, "Extreme ultraviolet lithography: a review," Journal of Vacuum Science & Technology B, vol. 25, pp. 1743-1761, Nov. 2007.

[24] R. Hirose, "New g-line lens for next generation," Proceedings of SPIE, vol. 1088, pp. 178-186, 1989.

[25] K. Eguchi, S. Miyazaki, C. Takai, and T. Suganuma, "0.5μm lithography using a g-line stepper with a 0.6 numerical aperture lens," Proceedings of the SPIE - The International Society for Optical Engineering, vol. 922, pp. 335-343, 1988.

[26] J. Przybyla, T. Emery, and H. Mukaled, "The effect of G-line filter transmission characteristics on dose matching between monochromatic exposure tools in a production environment," Proceedings of SPIE, vol. 1927, pp. 794-805, 1993.

[27] M. Ohta, T. Kojima, C. Sato, T. Ogawa, and M. Noguchi, "The future of projection lenses and the new g-line lens for 0.7μm lithography," Proceedings of the SPIE - The International Society for Optical Engineering, vol. 922, pp. 291-299, 1988.

[28] W. H. Ostrout, W. Mark Hiatt, and A. E. Kozlowski, "Process enhancement for a g-line photolithographic system," Microelectronics Manufacturing Technology, vol. 14, pp. 16-19, 1991.

[29] J. R. Sheats, "Photochemical image enhancement for 0.5μm g-line lithography," Polymer Engineering and Science, vol. 29, pp. 965-971, 1989.

[30] J. D. Buckley, "An advanced H-line stepper," Solid State Technology, vol. 30, pp. 87-93, 1987.

[31] G. Degiorgis, P. Pateri, A. Pilenga, R. J. Hurditch, B. T. Beauchemin, Jr., and E. A. Fitzgerald, "I-line photolithography: an investigation of resist bleachability and process performance," Proceedings of the SPIE - The International Society for Optical Engineering, vol. 1262, pp. 368-77, 1990.

[32] S. J. Holmes, P. H. Mitchell, and M. C. Hakey, "Manufacturing with DUV lithography," IBM Journal of Research and Development, vol. 41, pp. 7-20, 1997.

[33] W. Zhang and S. Y. Chou, "Multilevel nanoimprint lithography with submicron alignment over 4 in. Si wafers," Applied Physics Letters, vol. 79, pp. 845-847, 2001.

[34] H. Sakou, T. Miyatake, S. Kashioka, and M. Ejiri, "A position recognition algorithm for semiconductor alignment based on structural pattern matching," IEEE Transactions on Acoustics, Speech, and Signal Processing, vol. 37, pp. 2148-2157, 1989.

[35] O. Wilhelm, S. S. Peredkov, and A. L. Bogdanov, "Concept, construction and commissioning of an alignment system for deep X-ray lithography," Microelectronic Engineering, vol. 61-62, pp. 1107-1111, 2002.

[36] K. Cheol-Kyun, H. Cheol, K. Young-Sik, and B. Ki-Ho, "Optimization of alignment key in electron beam lithography," Proceedings of the SPIE - The International Society for Optical Engineering, vol. 3676, pp. 528-535, 1999.

[37] N. Bobroff and A. E. Rosenbluth, "Optical alignment for lithography," OSA Proceedings on Soft-X-Ray Projection Lithography. vol.12, pp. 42-44, 1991.

[38] T. Nakasugi, A. Ando, K. Sugihara, Y. Yamazaki, M. Miyoshi, and K. Okumura, "Alignment system using voltage contrast images for low-energy electron-beam lithography," Journal of Vacuum Science & Technology, vol. 19, pp. 2869-2873, 2001.

[39] H.-y. Wang and Z.-h. Wu, "Study on the alignment technology process of double-sided lithography on glass substrate," Semiconductor Technology, vol. 31, pp. 576-578, 2006.

[40] L. Wang, Y. Ding, B. Lu, Z. Qiu, and H. Liu, "Novel nano-scale overlay alignment method for room-temperature imprint lithography," Proceedings of the SPIE - The International Society for Optical Engineering, vol. 6149, pp. 61491-61496, 2006.

[41] D. P. Stumbo, G. A. Damm, D. W. Engler, F. O. Fong, S. Sen, J. C. Wolfe, J. N. Randall, P. Mauger, A. Shimkunas, and H. Loschner, "Advances in mask fabrication and alignment for masked ion beam lithography," Proceedings of the SPIE - The International Society for Optical Engineering, vol. 1263, pp. 35-43, 1990.

[42] L. B. Zhang, J. X. Shi, J. L. Yuan, S. M. Ji, and M. Chang, "The advancement of SPM-based nanolithography," Advances in Materials Manufacturing Science and Technology, vol. 471, pp. 353-357, 2004.

[43] Y. Takemura and J.-i. Shirakashi, "AFM lithography for fabrication of magnetic nanostructures and devices," Journal of Magnetism and Magnetic Materials, vol. 304, pp. 19-22, 2006.

[44] H. Sugimura and N. Nakagiri, "AFM lithography in constant current mode," Nanotechnology, vol. 8, pp. A15-A18, Sep. 1997.

[45] Z. J. Davis, G. Abadal, O. Hansen, X. Borise, N. Barniol, F. Perez-Murano, and A. Boisen, "AFM lithography of aluminum for fabrication of nanomechanical systems," Ultramicroscopy, vol. 97, pp. 467-472, Oct-Nov. 2003.

[46] S. Rozhok, P. Sun, R. Piner, M. Lieberman, and C. A. Mirkin, "AFM study of water meniscus formation between an AFM tip and NaCl substrate," Journal of Physical Chemistry B, vol. 108, pp. 7814-7819, Jun. 2004.

[47] R. L. Lo, W. C. Lee, and J. Kwo, "Atomic force microscopic nanolithography on hafnium oxide thin film grown on Si(100)," Japanese Journal of Applied Physics Part 1-Regular Papers Brief Communications & Review Papers, vol. 45, pp. 2067-2069, Mar. 2006.

[48] A. Notargiacomo, V. Foglietti, E. Cianci, G. Capellini, M. Adami, P. Faraci, F. Evangelisti, and C. Nicolini, "Atomic force microscopy lithography as a nanodevice development technique," Nanotechnology, vol. 10, pp. 458-463, Dec. 1999.

[49] I. Fernandez-Cuesta, X. Borrise, and F. Perez-Murano, "Atomic force microscopy local oxidation of silicon nitride thin films for mask fabrication," Nanotechnology, vol. 16, pp. 2731-2737, Nov. 2005.

[50] L. Santinacci, T. Djenizian, and P. Schmuki, "Atomic force microscopy-induced nanopatterning of Si(100) surfaces," Journal of the Electrochemical Society, vol. 148, pp. C640-C646, Sep. 2001.

[51] B. W. Maynor, Y. Li, and J. Liu, "Au ‘ink’ for AFM ‘dip-pen’ nanolithography," Langmuir, vol. 17, pp. 2575-2578, May. 2001.

[52] J. W. Park, D. W. Lee, N. Takano, and N. Morita, "Diamond tip cantilever for micro/nano machining based on AFM," in Progress on Advanced Manufacture for Micro/Nano Technology 2005, Pt 1 and 2. vol. 505-507, pp. 79-84, 2006.

[53] G. Agarwal, L. A. Sowards, R. R. Naik, and M. O. Stone, "Dip-pen nanolithography in tapping mode," Journal of the American Chemical Society, vol. 125, pp. 580-583, Jan. 2003.

[54] R. D. Piner, J. Zhu, F. Xu, S. H. Hong, and C. A. Mirkin, "‘Dip-pen’ nanolithography," Science, vol. 283, pp. 661-663, Jan. 1999.

[55] A. Ivanisevic and C. A. Mirkin, ""Dip-Pen" nanolithography on semiconductor surfaces," Journal of the American Chemical Society, vol. 123, pp. 7887-7889, Aug. 2001.

[56] S. Kuwahara, S. Akita, M. Shirakihara, T. Sugai, Y. Nakayama, and H. Shinohara, "Fabrication and characterization of high-resolution AFM tips with high-quality double-wall carbon nanotubes," Chemical Physics Letters, vol. 429, pp. 581-585, Oct. 2006.

[57] C. Van Haesendonck, L. Stockman, G. Neuttiens, C. Strunk, and Y. Bruynseraede, "Nanolithographic patterning of Au films with a scanning tunneling microscope," Journal of Vacuum Science & Technology B, vol. 13, pp. 1290-1293, 1995.

[58] C. Van Haesendonck, L. Stockman, Y. Bruynseraede, L. Langer, V. Bayot, J. P. Issi, J. P. Heremans, and C. H. Olk, "Nanolithographic patterning of metal films with a scanning tunnelling microscope," Physica Scripta T, vol. T55, pp. 86-89, 1994.

[59] D. Wouters and U. S. Schubert, "Nanolithography and nanochemistry: Probe-related patterning techniques and chemical modification for nanometer-sized devices," Angewandte Chemie-International Edition, vol. 43, pp. 2480-2495, 2004.

[60] R. Held, T. Heinzel, P. Studerus, and K. Ensslin, "Nanolithography by local anodic oxidation of metal films using an atomic force microscope," Physica E, vol. 2, pp. 748-752, Jul. 1998.

[61] B. Irmer, M. Kehrle, H. Lorenz, and J. P. Kotthaus, "Nanolithography by non-contact AFM-induced local oxidation: fabrication of tunnelling barriers suitable for single-electron devices," Semiconductor Science and Technology, vol. 13, pp. A79-A82, Aug. 1998.

[62] R. D. Ramsier, R. M. Ralich, and S. F. Lyuksyutov, "Nanolithography of silicon: An approach for investigating tip-surface interactions during writing," Applied Physics Letters, vol. 79, pp. 2820-2822, Oct. 2001.

[63] F. J. Rubio-Sierra, W. M. Heckl, and R. W. Stark, "Nanomanipulation by atomic force microscopy," Advanced Engineering Materials, vol. 7, pp. 193-196, Apr. 2005.

[64] W. C. Moon, T. Yoshinobu, and H. Iwasaki, "Nanoscale patterning of Au films on Si surfaces by atomic force microscopy," Japanese Journal of Applied Physics Part 1-Regular Papers Short Notes & Review Papers, vol. 38, pp. 6952-6954, Dec. 1999.

[65] X. J. Duan, J. Zhang, X. Ling, and Z. F. Liu, "Nano-welding by scanning probe microscope," Journal of the American Chemical Society, vol. 127, pp. 8268-8269, Jun. 2005.

[66] T. Zhenhua and B. Bharat, "New technique for studying nanoscale friction at sliding velocities up to 200 mm/s using atomic force microscope," Review of Scientific Instruments, vol. 77, pp. 103705-103709, Oct. 2006.

[67] K. Wilder, C. F. Quate, D. Adderton, R. Bernstein, and V. Elings, "Noncontact nanolithography using the atomic force microscope," Applied Physics Letters, vol. 73, pp. 2527-2529, Oct. 1998.

[68] H. Jung Hwan, Y. Jin-Young, H. Mitsuhiro, K. Sang Wook, K. Hyun-Woo, W. Sang-Gyoun, C. Han-Ku, H. Woo-Sung, M. Joo-Tae, and R. Byoung-Il, "Most efficient alternative manner of patterning sub-80 nm contact holes and trenches

with 193 nm lithography," Japanese Journal of Applied Physics, Part 1, vol. 43, pp. 3663-3667, 2004.

[69] W. Fallmann, A. Bruckner, E. Cekan, W. Friza, G. Stangl, F. Thalinger, P. Hudek, H. Loschner, and G. Stengl, "Demagnifying ion projection a promising alternative to optical and x-ray lithography," Electron Technology, vol. 26, pp. 107-114, 1993.

[70] C. M. Sotomayor Torresa, S. Zankovych, J. Seekamp, A. P. Kam, C. Clavijo Cedeno, T. Hoffmann, J. Ahopelto, F. Reuther, K. Pfeiffer, G. Bleidiessel, G. Gruetzner, M. V. Maximov, and B. Heidari, "Nanoimprint lithography: an alternative nanofabrication approach," Materials Science & Engineering C, vol. C23, pp. 23-31, 2003.

[71] R. K. Kupka, S. Megtert, M. Roulliay, and F. Bouamrane, "Transparent masks for aligned deep X-ray lithography/LIGA: Low-cost well-performing alternative using glass membranes," Proceedings of the SPIE - The International Society for Optical Engineering, vol. 3512, pp. 271-276, 1998.

[72] L.-C. Wittig, T. Clausnitzer, E. B. Kley, and A. Tunnermann, "Alternative Method of Gray Tone Lithography with Potential for the Fabrication of Combined Continues 3-Dimensional Surface Profiles and Sub-Wavelength Structures," Proceedings of SPIE - The International Society for Optical Engineering, vol. 5183, pp. 109-115, 2003.

[73] M. A. Piestrup, M. W. Powell, and L. W. Lombardo, "Alternative soft-x-ray source for step and scan lithography," Proceedings of SPIE - The International Society for Optical Engineering, vol. 2723, pp. 288-298, 1996.

[74] K. H. Brown, "Next generation lithography-the real challenge," AIP Conference Proceedings, vol. 449, pp. 481-483, 1998.

[75] A. Heuberger, *X-ray lithography*, Cambridge, UK, pp. 53-92, 1987.

[76] D. Fleming, J. R. Maldonado, and M. Neisser, "Prospects for X-ray lithography," Journal of Vacuum Science & Technology B, vol. 10, pp. 2511-2515, 1992.

[77] A. Zacharias, "An X-ray lithography system for VLSI device fabrication," Journal of Vacuum Science and Technology, vol. 16, pp. 1953, 1979.

[78] F. R. Aussenegg, A. Hohenau, H. Ditlbacher, B. Lamprecht, J. R. Krenn, and A. Leitner, "Electron beam lithography, a helpful tool for nanooptics," Microelectronic Engineering, vol. 83, pp. 1464-1467, 2006.

[79] H. C. Pfeiffer, T. R. Groves, and T. H. Newman, "High-throughput, high-resolution electron-beam lithography," IBM Journal of Research and Development, vol. 32, pp. 494-501, 1988.

[80] A. A. Tseng, C. Kuan, C. D. Chen, and K. J. Ma, "Electron beam lithography in nanoscale fabrication: Recent development," IEEE Transactions on Electronics Packaging Manufacturing, vol. 26, pp. 141-149, 2003.

[81] H. Sugimura and N. Nakagiri, "AFM lithography in constant current mode," Nanotechnology, vol. 8, pp. 15-18, 1997.

[82] S. C. Wimbush, M. Tachiki, E. Takayama-Muromachi, and H. Itozaki, "Atomic force microscope based lithography of $YBa_2Cu_3O_{7-\delta}$;thin films," Japanese Journal of Applied Physics, Part 1, vol. 45, pp. 5742-5745, 2006.

[83] X. Tian, N. Jiao, L. Liu, Y. Wang, Z. Dong, N. Xi, and W. Li, "An AFM based nanomanipulation system with 3D nano forces feedback," Proceedings - 2004

International Conference on Intelligent Mechatronics and Automation, pp. 18-22, 2004.

[84] T. Qian, S. San-Qiang, and Z. Limin, "Nanofabrication with atomic force microscopy," Journal of Nanoscience and Nanotechnology, vol. 4, pp. 948-963, 2004.

[85] H. Sugihara, A. Takahara, and T. Kajiyama, "Mechanical nanofabrication of lignoceric acid monolayer with atomic force microscopy," Journal of Vacuum Science & Technology B, vol. 19, pp. 593-595, 2001.

[86] M. Kato, M. Ishibashi, S. Heike, and T. Hashizume, "Nanofabrication using atomic force microscopy lithography combined with optical lithography," Japanese Journal of Applied Physics, Part 1, vol. 40, pp. 4317-4320, 2001.

[87] R. E. Ricker, A. E. Miller, D. F. Yue, G. Banerjee, and S. Bandyopadhyay, "Nanofabrication of a quantum dot array: atomic force microscopy of electropolished aluminum," Journal of Electronic Materials, vol. 25, pp. 1585-1592, 1996.

[88] S. Sasa, T. Ikeda, C. Dohno, and M. Inoue, "Atomic force microscope nanofabrication of InAs/AlGaSb heterostructures," Japanese Journal of Applied Physics, Part 1, vol. 36, pp. 4065-4067, 1997.

[89] G. Binnig and H. Rohrer, "Scanning tunneling microscopy," Helvetica Physica Acta, vol. 55, pp. 726-735, 1982.

[90] G. Binnig and H. Rohrer, "Scanning tunneling microscopy - from birth to adolescence," Reviews of Modern Physics, vol. 59, pp. 615-625, 1987.

[91] Y. Hosono and Y. Yamashita, "Piezoelectric ceramics and single crystals for ultrasonic medical transducers," Journal of Electroceramics, vol. 17, pp. 577-583, Dec. 2006.

[92] N. K. C. Ng, T. Li, J. Ma, and F. Y. C. Boey, "Behavior of piezoelectric ultrasonic tubular transducers in relation to tube geometry," Journal of Electroceramics, vol. 16, pp. 307-311, Jul. 2006.

[93] S. B. Lang and S. Muensit, "Review of some lesser-known applications of piezoelectric and pyroelectric polymers," Applied Physics a-Materials Science & Processing, vol. 85, pp. 125-134, Nov. 2006.

[94] M. M. Karpuk, D. A. Kostyuk, Y. A. Kuzavko, and V. G. Shavrov, "Ultrasonic piezoceramic transducers with a magnetoacoustic layer," Technical Physics Letters, vol. 30, pp. 1005-1008, 2004.

[95] R. Young, J. Ward, and F. Scire, "Topografiner - Instrument for measuring surface microtopography," Review of Scientific Instruments, vol. 43, pp. 999-1011, 1972.

[96] H. T. H. Chen, W. Ng, and R. L. Engelstad, "Finite-element analysis of a scanning-X-ray microscope micropositioning Stage," Review of Scientific Instruments, vol. 63, pp. 591-594, Jan. 1992.

[97] A. Guha, S. Kim, and A. L. de Lozanne, "Novel frictionless approach mechanism for a scanning tunneling microscope," Review of Scientific Instruments, vol. 74, pp. 4384-4388, Oct. 2003.

[98] H. P. Rust, J. Buisset, E. K. Schweizer, and L. Cramer, "High precision mechanical approach mechanism for a low temperature scanning tunneling microscope," Review of Scientific Instruments, vol. 68, pp. 129-132, Jan. 1997.

[99] G. Meyer and N. M. Amer, "Novel optical approach to atomic force microscopy," Applied Physics Letters, vol. 53, pp. 1045-1047, Sep. 1988.

[100] S. Akita, H. Nishijima, Y. Nakayama, F. Tokumasu, and K. Takeyasu, "Carbon nanotube tips for a scanning probe microscope: their fabrication and properties," Journal of Physics D-Applied Physics, vol. 32, pp. 1044-1048, May. 1999.

[101] P. Fontaine, P. Guenoun, and J. Daillant, "A critical look at surface force measurement using a commercial atomic force microscope in the noncontact mode," Review of Scientific Instruments, vol. 68, pp. 4145-4151, 1997.

[102] C. A. J. Putman, K. O. Vanderwerf, B. G. Degrooth, N. F. Vanhulst, and J. Greve, "Tapping mode atomic-force microscopy in liquid," Applied Physics Letters, vol. 64, pp. 2454-2456, May. 1994.

[103] S. S. F. Chan and J. B. D. Green, "Tapping mode imaging and measurements with an inverted atomic force microscope," Langmuir, vol. 22, pp. 6701-6706, Jul. 2006.

[104] N. Hosaka and T. Saiki, "Near-field fluorescence imaging of single molecules with a resolution in the range of 10 nm," Journal of Microscopy-Oxford, vol. 202, pp. 362-364, May. 2001.

[105] T. Fukuma, J. I. Kilpatrick, and S. P. Jarvis, "Phase modulation atomic force microscope with true atomic resolution," Review of Scientific Instruments, vol. 77, pp. 123703-123705, Dec. 2006.

[106] D. J. Fermin, "Nanoscale probing of electrode surfaces by scanning force microscopy," Chimia, vol. 60, pp. A789-A794, 2006.

[107] K. Murayama, S. Gonda, K. Kinoshita, H. Koyanagi, T. Terasawa, and S. Hosaka, "Height measurement using high-precision atomic force microscope scanner combined with laser interferometers," Japanese Journal of Applied Physics Part 1, vol. 45, pp. 8832-8838, Nov. 2006.

[108] M. R. Gullo, P. Frederix, T. Akiyama, A. Engel, N. F. deRooij, and U. Staufer, "Characterization of microfabricated probes for combined atomic force and high-resolution scanning electrochemical microscopy," Analytical Chemistry, vol. 78, pp. 5436-5442, Aug. 2006.

[109] J. E. Kim, J. K. Park, and C. S. Han, "Use of dielectrophoresis in the fabrication of an atomic force microscope tip with a carbon nanotube: Experimental investigation," Nanotechnology, vol. 17, pp. 2937-2941, Jun. 2006.

[110] R. J. Fasching, S. J. Bai, T. Fabian, and F. B. Prinz, "Nanoscale electrochemical probes for single cell analysis," Microelectronic Engineering, vol. 83, pp. 1638-1641, Apr.-Sep. 2006.

[111] A. Limanskii, "Functionalization of aminomodified probes for atomic force microscopy," Biofizika, vol. 51, pp. 225-235, Mar.-Apr. 2006.

[112] J. A. J. Steen, J. Hayakawa, T. Harada, K. Lee, F. Calame, G. Boero, A. J. Kulik, and J. Brugger, "Electrically conducting probes with full tungsten cantilever and tip for scanning probe applications," Nanotechnology, vol. 17, pp. 1464-1469, Mar. 2006.

[113] T. R. Albrecht, S. Akamine, T. E. Carver, and C. F. Quate, "Microfabrication of cantilever styli for the atomic force microscope," Journal of Vacuum Science & Technology a-Vacuum Surfaces and Films, vol. 8, pp. 3386-3396, Jul.-Aug. 1990.

[114] D. J. Keller and C. C. Chou, "Imaging steep, high structures by scanning force microscopy with electron-beam deposited tips," Surface Science, vol. 268, pp. 333-339, May. 1992.

[115] K. Nishio, T. Ozaki, T. Morishita, W. Shinoda, and M. Mikami, "Electronic and optical properties of polyicosahedral Si nanostructures: A first-principles study," Physical Review B, vol. 77, pp. 075431-075444, Feb. 2008.

[116] J. C. Yi, "Miniband properties of superlattice quantum dot arrays fabricated by the edge-defined nanowires," Microelectronics Journal, vol. 39, pp. 369-374, Mar.-Apr. 2008.

[117] F. J. Himpsel, K. N. Altmann, R. Bennewitz, J. N. Crain, A. Kirakosian, J. L. Lin, and J. L. McChesney, "One-dimensional electronic states at surfaces," Journal of Physics: Condensed Matter, vol. 13, pp. 11097-11113, 2001.

[118] W. Lu and C. M. Lieber, "Semiconductor nanowires," Journal of Physics D-Applied Physics, vol. 39, pp. R387-R406, Nov. 2006.

[119] Y. Hu, J. Xiang, G. Liang, H. Yan, and C. M. Lieber, "Sub-100 nanometer channel length Ge/Si nanowire transistors with potential for 2 THz switching speed," Nano Letters, vol. 8, pp. 925-930, 2008.

[120] Y. Cui, Q. Wei, H. Park, and C. M. Lieber, "Nanowire nanosensors for highly sensitive and selective detection of biological and chemical Species," Science, vol. 293, pp. 1289-1292, 2001.

[121] F. Patolsky and C. M. Lieber, "Nanowire nanosensors," Materials Today, vol. 8, pp. 20-28, 2005.

[122] G. Timp, *Nanotechnology*, New York, Springer, pp. 207-256, 1998.

[123] E. Yablonovitch and R. B. Vrijen, "Optical projection lithography at half the Rayleigh resolution limit by two-photon exposure," Optical Engineering, vol. 38, pp. 334-338, Feb. 1999.

[124] S. Okazaki, "Resolution limits of optical lithography," The Journal of Vacuum Science and Technology B, vol. 9, pp. 2829-2833, 1991.

[125] G. W. Tasker, S. T. Bentley, S. M. Shank, R. J. Soave, A. M. Then, "Microfabrication of channel electron multipliers," Proceedings of SPIE - The International Society for Optical Engineering, vol. 2640, pp. 58-70, 1995.

[126] Y. Zhao and C. Shu, "Selectable dual-wavelength pulses generated from a laser diode using external feedback from a two-chromatic fiber grating," Applied Physics Letters, vol. 73, pp. 2402-2404, 1998.

[127] S. Y. Chou, "Nano-imprint lithography and lithographically induced self-assembly," MRS Bulletin, vol. 26, pp. 512-517, 2001.

[128] M. A. Herman, *Molecular Beam Epitaxy: Fundamentals and Current Status*, New York, Springer, pp. 18-29, 1996.

[129] J. S. Frood, G. J. Davis, and W. T. Tsang, *Chemical Beam Epitaxy and Related Techniques*, New York, Wiley, pp. 331-394, 1997.

[130] S. Mahajan and K. S. S. Harsha, *Principles of Growth and Processing of Semiconductors*, New York, McGraw-Hill, pp, 223-235, 1999.

[131] K. K. Lew, C. Reuther, A. H. Carim, J. M. Redwing, and B. R. Martin, "Template-directed vapor--liquid--solid growth of silicon nanowires," Journal of Vacuum Science & Technology B: Microelectronics and Nanometer Structures, vol. 20, pp. 389-392, 2000.

[132] M. R. S. Kim, *Advances in quantum dot structures. In: Processing and Properties of Compound Semiconductors,* ed. by R. Willardson, H. S. Navawa, New York, Academic Press, pp. 21-28, 2001.

[133] Y. H. Tang, Y. F. Zhang, N. Wang, W. S. Shi, C. S. Lee, I. Bello, and S. T. Lee, "Si nanowires synthesized from silicon monoxide by laser ablation," Journal of Vacuum Science & Technology B: Microelectronics and Nanometer Structures, vol. 19, pp. 317-319, 2001.

[134] F. Guffarth, R. Heitz, A. Schliwa, O. Stier, N. N. Ledentsov, A. R. Kovsh, V. M. Ustinov, and D. Bimberg, "Strain engineering of self-organized InAs quantum dots," Physical Review B, vol. 64, pp. 085305-085307, 2001.

[135] R. J. Tonucci, B. L. Justus, A. J. Campillo, and C. E. Ford, "Nanochannel array glass," Science, vol. 258, pp. 783-785, 1992.

[136] G. A. Ozin, "Nanochemistry: Synthesis in diminishing dimensions," Advanced Material, vol. 4, pp. 612-649, 1992.

[137] J. Y. Ying, "Nanoporous systems and templates," Science of Spectra, vol. 18 p. 56-77, 1999.

[138] J. M. Rabaey, A. P. Chandrakasan, and B. Nikolic, *Digital Integrated Circuits: A Design Perspective*, 2nd edition, Saddle River, Prentice Hall Electronics and VLSI Series, NJ, pp.7-9, 2003.

[139] P. M. Zeitzoff, "2007 International Technology Roadmap: MOSFET scaling challenges," Solid State Technology, vol. 51, pp. 35-37, Feb. 2008.

[140] S. W. Chung, J. Y. Yu, and J. R. Heath, "Silicon nanowire devices," Applied Physics Letters, vol. 76, pp. 2068-2070, Apr. 2000.

[141] C. B. Sophie, L. Boyer, F. H. Z. Mekhalif, J. Delhalle, J. J. Pireaux,, "Adhesion properties and surface analyses of monolayers of n-dodecanethiol self-assembled on galvanic gold," Surface and Interface Analysis, vol. 26, pp. 889-895, 1998.

[142] S. Sampathkumar, A. Li, M. Jones, Z. Sun, and K. Yarema, "Metabolic installation of thiols into sialic acid modulates adhesion and stem cell biology," Nature Chemical Biology, vol. 2, pp. 149-152, 2006.

[143] C. A. Zorman and R. J. Parro, "Micro- and nanomechanical structures for silicon carbide MEMS and NEMS," Physica Status Solidi B-Basic Solid State Physics, vol. 245, pp. 1404-1424, Jul. 2008.

[144] C. Rossi, K. Zhang, D. Esteve, P. Alphonse, P. Tailhades, and C. Vahlas, "Nanoenergetic materials for MEMS: A review," Journal of Microelectromechanical Systems, vol. 16, pp. 919-931, Aug. 2007.

[145] H. A. Abdel-Aal, J. A. Patten, and L. Dong, "On the thermal aspects of ductile regime micro-scratching of single crystal silicon for NEMS/MEMS applications," Wear, vol. 259, pp. 1343-1351, Jul.-Aug. 2005.

[146] S. Sukhoveyev, "Ultra high aspect-ratio MEMS and NEMS on basis of fibrous composite technology," Microsystem Technologies-Micro-and Nanosystems-Information Storage and Processing Systems, vol. 14, pp. 1099-1110, Aug. 2008.

[147] K. J. McLean, "Cohesion of precipitated dust layer in electrostatic precipitators," Journal of the Air Pollution Control Association, vol. 27, p. 1100-1103, 1977.

[148] K. Kendall, "Solid surface energy measured electrically," Journal of Physics D: Applied Physics, vol. 23, pp. 1329-1331, 1990.

[149] J. Israelachvili, *Intermolecular and Surface Forces*, 3e, Elsevier Publishing Company, pp. 17-59, 2003.

[150] F. P. Bowden and D. Tabor, *The Friction and Lubrication of Solids*, Oxford University Press, pp. 25-32, 2001.

[151] C. A. J. Putman, M. Igarashi, and R. Kaneko, "Single-asperity friction in friction force microscopy: The composite-tip model," Applied Physics Letters, vol. 66, pp. 3221-3223, 1995.

[152] J. A. Greenwood and J. B. P. Williamson, "Contact of nominally flat surfaces," Proceedings of the Royal Society of London. Series A, Mathematical and Physical Sciences, vol. 295, pp. 300-319, 1966.

[153] K. Hayashi, N. Sakudo, and T. Kawai, "A new measure of local temperature distribution in non-equilibrium molecular dynamics simulation of friction," Surface and Coatings Technology, vol. 83, pp. 313-316, 1996.

[154] E. Meyer, *Nanoscience: Friction and Rheology on the Nanometer Scale*, World Scientific Publishing Company, pp. 29-98, 1998.

[155] A. Buldum, S. Ciraci, and I. P. Batra, "Contact, nanoindentation, and sliding friction," Physical Review B, vol. 57, pp. 2468-2476, 1998.

[156] J. Shimizu, H. Eda, M. Yoritsune, E. Ohmura, "Molecular dynamics simulation of friction on the atomic scale," Nanotechnology, vol. 9, pp. 118-123, 1998.

[157] T. Narusawa, K. Kinoshita, W. M. Gibson, and A. Hiraki, "Structure study of Au--Si interface by MeV ion scattering," Journal of Vacuum Science and Technology, vol. 18, pp. 872-875, 1981.

[158] J. J. Yeh, J. Hwang, K. Bertness, D. J. Friedman, R. Cao, and I. Lindau, "Growth of the room temperature Au/Si(111)-7×7 interface," Physical Review Letters, vol. 70, pp. 3768- 3771, 1993.

[159] T. Narusawa, S. Komiya, and A. Hiraki, "Diffuse interface in Si (substrate)-Au (evaporated film) system," Applied Physics Letters, vol. 22, pp. 389-390, 1973.

[160] J. W. Cahn and J. E. Hilliard, "Free energy of a nonuniform system. I. interfacial free energy," The Journal of Chemical Physics, vol. 28, pp. 258-267, 1958.

[161] J. Dargahi, N. P. Rao, and S. Sokhanvar, "Design and microfabrication of a hybrid piezoelectric-capacitive tactile sensor," Sensor Review, vol. 26, pp. 186-192, 2006.

[162] J. Dargahi, N. P. Rao, and S. Sokhanvar, "Design and microfabrication of a hybrid piezoelectric-capacitive tactile sensor," Sensor Review, vol. 26, pp. 186-192, 2006.

[163] D. G. Pirolo and E. S. Kolesar, "Piezoelectric polymer tactile sensor arrays for robotics," Proceedings of the IEEE 1989 National Aerospace and Electronics Conference, vol. 3, pp. 1130-1135, 1989.

[164] Q. X. Chen and P. A. Payne, "Industrial applications of piezoelectric polymer transducers," Measurement Science & Technology, vol. 6, pp. 249-267, 1995.

[165] G. R. Crane and A. A. Comparini, "Transducer applications of piezoelectric polymers," IEEE Transactions on Industry Applications, vol. 35, pp. 380-382, 1977.

[166] C. Zhang, "Piezoelectric polymers and their applications," Key Engineering Materials, vol. 122-124, pp. 71-144, 1996.

[167] T. R. Dargaville, M. Celina, J. W. Martin, and B. A. Banks, "Evaluation of piezoelectric PVDF polymers for use in space environments. II. Effects of atomic oxygen and vacuum UV exposure," Journal of Polymer Science, Part B (Polymer Physics), vol. 43, pp. 2503-2513, 2005.

[168] R. G. Kepler, "Piezoelectricity and pyroelectricity in poly(vinylidene fluoride)," Journal of Applied Physics, vol. 49, pp. 4490-4494, 1978.

[169] G. Eberle, H. Schmidt, and W. Eisenmenger, "Piezoelectric polymer electrets," IEEE Transactions on Dielectrics and Electrical Insulation, vol. 3, pp. 624-646, 1996.

[170] H. Kawai, "The piezoelectricity of poly(vinylidene fluoride)," Japanese Journal of Applied Physics, vol. 8, pp. 975-976, 1969.

[171] K. Nakamura and Y. Wada, "Piezoelectricity, pyroelectricity, and the electrostriction constant of poly(vinylidene fluoride)," Journal of Polymer Science, Part A-2, vol. 9, pp. 161-173, 1971.

[172] H. Tanaka, K. Takayama, S. Taki, and T. Takemura, "Piezoelectricity of poly(vinylidene fluoride) under high pressure," Japanese Journal of Applied Physics, Part 2, vol. 21, pp. 715-721, 1982.

[173] S. Tasaka and S. Miyata, "The origin of piezoelectricity in poly(vinylidene fluoride)," Ferroelectrics, vol. 32, pp. 17-23, 1981.

[174] W. J. Bell and K. G. Adiyodi, *The American Cockroach*, London, Chapman and Hall, pp. 117-150, 1981.

[175] M. K. Rust, D. A. Reierson, and K. H. Hansgen, "Control of American cockroaches (Dictyoptera: Blattidae) in sewers," Journal of Medical Entomology, vol. 28, pp. 210-213, 1991.

[176] R. Holzer and I. Shimoyama, "Locomotion control of a bio-robotic system via electric stimulation," IEEE International Conference on Intelligent Robots and Systems, vol. 3, pp. 1514-1519, 1997.

[177] E. Kramer, "The orientation of walking honeybees in odour fields with small concentration gradients," Physiological Entomology, vol. 1, pp. 27-37, 1976.

[178] R. J. Full and M. A. R. Koehl, "Drag and lift on running insects," The Journal of Experimental Biology, vol. 176, pp. 89-101, Mar. 1993.

[179] R. J. Full and M. S. Tu, "Mechanics of six-legged runners," Journal of Experimental Biology, vol. 148, pp. 129-146, Jan. 1990.

[180] S. W. R. Lee and C. T. Sun, "Bending/twisting/shearing actuation and sensing of laminated composite beams with piezopolymer film," Intelligent Materials and Systems, vol. 10, pp. 137-148, 1995.

[181] G. M. Sessler and A. Berraissoul, "Tensile and bending piezoelectricity of single-film PVDF monomorphs and bimorphs," IEEE Transactions on Electrical Insulation, vol. 24, pp. 249-254, 1989.

[182] S. A. Hashmi and A. H. Jayatissa, "Modeling of piezoelectric response in PVDF for monitoring of mechanical bending in hinges," Proceedings of 2006 ASME International Mechanical Engineering Congress and Exposition, pp. 6-11, 2006.

[183] T. Takamatsu, R. W. Tian, and H. Sasabe, "Bending piezoelectricity of polymer electrets," IEEE, vol. 5, pp. 942-946, 1985.

[184] J. Dargahi, M. Parameswaran, and S. Payandeh, "A micromachined piezoelectric tactile sensor for an endoscopic grasper-theory, fabrication and experiments," Journal of Microelectromechanical Systems, vol. 9, pp. 329-35, 2000.

[185] I. Lee and H. J. Sung, "Development of an array of pressure sensors with PVDF film," Experiments in Fluids, vol. 26, pp. 27-35, 1999.

[186] P. E. Bloomfield and R. A. Ferren, "Piezoelectricity and pyroelectricity in Poly(Vinylidene Fluoride)," Naval Research Reviews, vol. 31, pp. 1-15, 1978.

[187] F. Delcomyn, *Walking and running. In, Comprehensive Insect Physiology, Biochemistry and Pharmacology*, Ed. by G.A. Kerkut and L.I. Gilbert, London, Pergamon Press, Chapt 11, Vol. 5, pp. 439-466, 1985.

[188] Q. X. Chen and P. A. Payne, "Industrial applications of piezoelectric polymer transducers," Measurement Science & Technology, vol. 6, pp. 249-267, 1995.

[189] S. Bauer, S. B. Gogonea, M. Dansachmüller, G. Dennler, I. Graz, M. Kaltenbrunner, C. Keplinger, H. Reiss, N. S. Sariciftci, T. B. Singh, R. Schwödiauer, "Piezoelectric polymers," Materials Research Society Symposium Proceedings, vol. 889, pp. 23-30, 2006.

[190] M. Madou, *Fundamentals of Microfabrication*, Boca Raton, CRC Press, FL, pp. 518-522, 1997.

[191] G. Kovacs, *Micromachined Transducers Sourcebook*, New York, McGraw-Hill, pp. 77-122, 1998.

[192] I. Seo, "Piezoelectric polymers and their applications," Journal of the Japan Society of Precision Engineering, vol. 55, pp. 1374-1377, 1989.

[193] D. Q. Xiao and S. B. Lang, "Measurement applications based on pyroelectric properties of ferroelectric polymers," IEEE Transactions on Electrical Insulation, vol. 24, pp. 503-516, Jun. 1989.

[194] R. Aoshima, Y. Kanda, A. Takada, and A. Yamashita, "Sulfonated poly (vinylidene fluoride) as a biomaterial: Immobilization of urokinase and biocompatibility," Journal of Biomedical Materials Research, vol. 16, pp. 289-299, 1982.

[195] I. Sons, "Polyvinylidene fluoride (PVDF) as a biomaterial: From polymeric raw material to monofilament vascular suture," Journal of Biomedical Materials Research, vol. 29, p. 152-515, 1995.

[196] S. Bouaidat, B. Winther-Jensen, S. F. Christensen, and J. Jonsmann, "Plasma-polymerized coatings for bio-MEMS applications," Sensors & Actuators: A. Physical, vol. 110, pp. 390-394, 2004.

[197] T. Furukawa and N. Seo, "Electrostriction as the origin of piezoelectricity in ferroelectric polymers," Japanese Journal of Applied Physics Part 1-Regular Papers Short Notes & Review Papers, vol. 29, pp. 675-680, Apr. 1990.

[198] E. Fukada, "History and recent progress in piezoelectric polymers," Ieee Transactions on Ultrasonics Ferroelectrics and Frequency Control, vol. 47, pp. 1277-1290, Nov. 2000.

[199] K. Tashiro, M. Kobayashi, H. Tadokoro, and E. Fukada, "Calculation of elastic and piezoelectric constants of polymer crystals by a point-charge model - applition to poly(vinylidene fluoride) Form-1," Macromolecules, vol. 13, pp. 691-698, 1980.

[200] K. Tashiro, H. Tadokoro, and M. Kobayashi, "Structure and piezoelectricity of poly(vinylidene fluoride)," Ferroelectrics, vol. 32, pp. 167-175, 1981.

[201] J. Sirohi and I. Chopra, "Fundamental understanding of piezoelectric strain sensors," Journal of Intelligent Material Systems and Structures, vol. 11, pp. 246-257, Apr. 2000.

[202] F. Hui-Qing, S. Ke-He, W. Zhi-Yin, and W. Zhen-Yi, "Structure and piezoelectric properties of poly(vinylidene fluoride) studied by density functional theory," Polymer, vol. 47, pp. 7988-7996, 2006.

[203] F. J. Lu and S. L. Hsu, "Spectroscopic study of the electric field induced microstructural changes in poly (vinylidene fluoride)," Polymer, vol. 25, pp. 1247-1252, 1984.

[204] B. E. El Mohajir and N. Heymans, "Changes in structural and mechanical behaviour of PVDF with processing and thermomechanical treatments. 1. Change in structure," Polymer, vol. 42, pp. 5661-5667, Jun. 2001.

[205] T. Sun, G. Wang, L. Feng, B. Liu, Y. Ma, L. Jiang, and D. Zhu, "Reversible switching between superhydrophilicity and superhydrophobicity," Angew. Chem. Int. Ed, vol. 43, pp. 357-360, 2004.

[206] J. Cir, P. Tomc, D. Barancok, A. Bolognesi, and M. Ragazzi, "Dipole moment of a modified poly(3-alkylthiophene) at the air/water interface," Thin Solid Films, vol. 402, pp. 190-194, 2002.

[207] C. Duan, W. N. Mei, W. G. Yin, J. Liu, J. R. Hardy, S. Ducharme, and P. A. Dowben, "Simulations of ferroelectric polymer film polarization: The role of dipole interactions," Physical Review B, vol. 69, pp. 235106-235116, 2004.

[208] W. Song, T. Sun, Y. Song, Y. Bai, F. Liu, and L. Jiang, "An atomic force microscopic investigation of electro-sensitive polymer surface," Talanta, vol. 67, pp. 543-547, 2005.

[209] A. Maksimov, "Theory of ordering in three-dimensional polymer systems with local orientational-deformational interactions," Polymer Science Series A, vol. 49, pp. 599-610, 2007.

[210] K. Wang, H. Lee, R. Cooper, and H. Liang, "Time resolved, stress induced, and anisotropic phase transformation of a piezoelectric polymer," Journal of Applied Physics, A, (accepted).

VITA

Name: Hyungoo Lee

Address: Department of Mechanical Engineering,
Texas A&M University
College Station,
TX 77843-3123, USA

Email Address: prettylhg@tamu.edu

Education: Ph.D., Mechanical Engineering, Texas A&M University, 2009
B.S., Electrical Engineering, University of Seoul, 2002